Experimental observation and integrated modelling of proton-beryllium fusion in He and D plasmas at JET

Ž. Štancar[a,*], J. Eriksson[b], H.J.C. Oliver[a], V.G. Kiptily[a], S. Conroy[b], A. Čufar[c], A. Hjalmarsson[b], Ye.O. Kazakov[d], Z. Ghani[a], M. Gorelenkova[e], A. Boboc[a], P. Carvalho[a], A. Chomiczewska[f], E. Delabie[a], M. Dreval[g], L. Garzotti[a], K. Kirov[a], D. Kos[a], K. D. Lawson[a], I. Lengar[c], M. Lenholm[a], E. Lerche[d], X. Litaudon[h], E. Litherland-Smith[a], M. Maslov[a], S. Menmuir[a], M. O'Mullane[a], E. Parr[a], A. Patel[a], L. Snoj[c], R. Sydenham[i], H. J. Sun[a], R. Villari[j], V.T. Wang[k], V.K. Zotta[l], JET Contributors[m]

[a] *United Kingdom Atomic Energy Authority, Culham Campus, UK*
[b] *Department of Physics and Astronomy, Uppsala University, Sweden*
[c] *Jožef Stefan Institute, Ljubljana, Slovenia*
[d] *Laboratory for Plasma Physics, Ecole Royale Militaire, Brussels, Belgium*
[e] *Princeton Plasma Physics Laboratory, Princeton, USA*
[f] *Institute of Plasma Physics and Laser Microfusion, Warsaw, Poland*
[g] *National Science Centre, Kharkiv Institute of Physics and Technology, Kharkiv, Ukraine*
[h] *CEA, Cadarache, France*
[i] *University of Portsmouth, Portsmouth, UK*
[j] *C.R. ENEA Frascati, Frascati, Italy*
[k] *Queen Mary University, London, UK*
[l] *Dipartimento di Ingegneria Astronautica, Elettrica ed Energetica, University of Rome La Sapienza Faculty of Engineering, Rome, Italy*
[m] *See the author list of 'Overview of T and D-T results in JET with ITER-like wall' by CF Maggi et al 2024 Nucl. Fusion 64 112012*

Abstract

In the paper we present validated integrated modelling of JET experiments in which fusion performance is driven by reactions between fast ions and intrinsically present metal wall impurities. A steady-state L-mode plasma with dominant proton-beryllium fusion and neutron yields of up to $\approx 6{\cdot}10^{13}$ s^{-1} is developed in He and D. The fusion drive is unambiguously confirmed by neutron and γ-ray diagnostics. The experiments are analysed via an integrated modelling framework, developed to model the two-stage proton beryllium-fusion chain and produce high-fidelity fusion product source terms. The modelling chain comprises TRANSP and JETTO for plasma core modelling, LOCUST for full orbit product tracking and collisional slowing-down, DRESS to resolve two- and three-body fusion kinematics, and MCNP for neutron transport calculations. Modelling shows that the primary ^{9}Be(p,n)^{9}B reaction is the dominant neutron emitter at naturally present concentrations of beryllium in these experiments. The yield contribution of secondary reactions between fusion products and beryllium, ^{9}Be(d,n)^{10}B and ^{9}Be(α,n)^{12}C, is found to be negligible. The proton-deuteron knock-on effect in D plasmas is modelled, which is calculated to contribute $\approx$ 25 % to the total neutron yield. For both He and D discharges the total computed neutron rates match fission chamber measurements within the combined experimental and computational uncertainty, with an average discrepancy of $\approx \pm$ 20 %. Realistic proton-beryllium neutron sources are propagated through JET's MCNP neutron transport model – we find that the ^{235}U fission chambers' response is sensitive to p–Be source changes, with up to $\approx$ 10 % variation compared to a generic D-D neutron source. We show that differences in p–Be spectral tail energy gradients, present because of fast proton distribution variations in the discharges, could be detected via multi-foil neutron activation. The tool is applied to the study of interactions between fast ions and

boron impurities, of relevance to ITER – we calculate that in JET conditions a significant alpha source with DT-like energies could be generated through ^{11}B(p,α)2α, and detected via γ-emission in secondary interactions between fast alphas and boron. The work represents an important step towards validating predictive integrated modelling capabilities for non-standard fusion reactions.

Keywords:
Proton-beryllium fusion, Integrated modelling, Plasma neutron source, Neutron yield, JET

1. Introduction

Fusion power measurements are an essential tokamak operational parameter, relevant for radiation safety, fuel self-sufficiency estimates, plasma diagnostics, whole-plant operation planning, as well as validating progress towards developing plasma scenarios with high fusion gain [1, 2, 3, 4] – the latter being of increasing importance as we enter an era of public-private fusion partnerships targeting the demonstration of burning plasma conditions in magnetically confined devices. Fusion yield measurements in tokamaks are generally absolutely calibrated via an elaborate in-vessel procedure and supported by extensive neutronics calculations [5, 6, 7], with the calibration accuracy dependent on the fidelity of underlying plasma neutron sources and neutron transport computational models. Similar in-situ P_{fus} calibration procedures are envisioned to be used in future fusion reactors, such as SPARC [8], ITER [9], and DEMO [10], motivating continuous improvement, optimization, and development of the fusion yield calibration process, as well as of the integrated modelling framework supporting it.

Over the past decade extensive collaborative effort has been invested into the development and validation of coupled plasma-neutronics integrated modelling workflows for tokamaks, based on state-of-the-art plasma transport solvers, kinematics codes, and Monte Carlo neutron and photon transport codes [11, 12, 13, 14]. The aim is to generate unprecedented high-fidelity neutron and gamma plasma source models, comprising radially and poloidally resolved emissivity profiles with realistic pitch-dependent energy spectra. The models are based on interpretive plasma simulations [15], with bespoke neutron sources computed and validated for individual plasma discharges, or predictive plasma simulations, strengthening our confidence in fusion yield estimates for future fusion reactors [16]. The neutron and gamma source models are used in synthetic diagnostics codes for diagnostics optimization and experiment analysis, in neutron and photon transport shielding and radiation safety studies, or could provide input to surrogate models for fusion performance estimates.

In this paper we extend the application of coupled plasma-neutronics workflows to the non-standard proton-beryllium fusion reaction chain (denoted *p–Be*). The methodology is validated with dedicated experiments aimed at triggering reactions between fast ions and beryllium impurities in He and D plasmas at JET. The following reactions in the proton-beryllium chain are relevant for this work:

I.a) $^{9}Be(p,n)^{9}B$ with Q = –1.85 MeV
I.b) $^{9}Be(p,\alpha)^{6}Li$ with Q = 2.126 MeV
I.c) $^{9}Be(p,d)2\alpha$ with Q = 0.65 MeV
II.a) $^{9}Be(d,n)^{10}B$ with Q = 4.36 MeV
II.b) $^{9}Be(\alpha,n)^{12}C$ with Q = 5.7 MeV

*Corresponding author
Email address: ziga.stancar@ukaea.uk (Ž. Štancar)

Reactions are divided into two groups - the primary fusion reactions between beryllium and fast protons are denoted *I.a)* to *I.c)*, of which only the first reaction is neutron-emitting. The latter is a threshold reaction, with the minimum kinetic energy of the impinging proton needed to trigger it being above 2.06 MeV, meaning the production of neutrons via ^{9}Be(p,n)^{9}B fusion can exclusively be driven by the presence of a suprathermal, MeV-range population of protons. While reactions *I.b)* to *I.c)* do not emit neutrons, they produce high-energy deuterons ($E_{\mathrm{d}} \approx 0.6$ MeV) and alphas ($0.5 \lessapprox E_{\alpha} \lessapprox 1.8$ MeV). These charged fusion products are confined and collisionally slowed-down, triggering secondary neutron-emitting fusion on beryllium impurities, via reactions denoted *II.a)* and *II.b)*. Neutron emission via fusion between fast ions and beryllium impurities is thus a two-step process, in which the strength of contributions to the fusion yield from primary proton-induced and secondary fusion-product-induced fusion strongly depends on the mean energy of the proton population, and the fast protons' energy distribution.

The experimental and integrated modelling work presented in the paper is driven by the following motivation:

(i) Design a steady-state plasma scenario which can be applied to the study of fusion products emitted via reactions between fast ions and metallic wall impurities, taking advantage of the naturally present Be impurities in JET's ITER-like-wall (ILW, metal Be/W): Dedicated experiments aimed at studying the interaction between fast ions and beryllium have been performed at JET before – in [17] evidence of neutrons emitted as a result of ^{9}Be(^{3}He,n)^{11}C fusion is presented, performed with JET's carbon wall, which required wall preparation via Be evaporation. It was shown that in bulk D plasmas with dominating d(d,n)^{3}He neutron emission, beryllium fusion contributed ≈ 20 % to the total fusion yield. The detection of neutrons with energies up to 10 MeV by the time-of-flight neutron spectrometer, extending above the 2.45 MeV D-D neutron peak, was linked to ^{9}Be(^{3}He,n)^{11}C emission. Another targeted experiment was performed with JET's ILW in hydrogen plasmas, analysed in [18], utilizing the synergistic effect of H-NBI and second harmonic RF heating to generate an MeV-range population of fast protons. A transient neutron emission event was reported, peaking at a rate of $3.1{\cdot}10^{13}$ s^{-1}, which was argued to be dominated by ^{9}Be(p,n)^{9}B fusion. In the paper a D discharge with H RF minority heating is also analysed and TOFOR neutron spectrum measurements presented. It is postulated that the interactions between bulk thermal D and proton-beryllium fusion deuterons contribute to around 50 % of the observed neutron rate at $\approx 1.5{\cdot}10^{13}$ s^{-1}, based on the broadening of the measured D-D neutron spectrum's beam-target component.
In this work we improve on the experimental results by developing an optimized JET-ILW scenario in He and D plasmas, utilizing H minority RF heating at the fundamental frequency, in which steady-state neutron emission is fully driven by the proton-beryllium fusion chain, sustained over multiple slowing-down times of the fast proton population $\tau_{\mathrm{p,f}}$ (note that $\tau_{\mathrm{p,f}} \gg$ plasma energy confinement time τ_{e}).

(ii) Improve and demonstrate the modelling capability for non-standard fusion reaction products, specifically those occurring regularly in magnetic confinement devices between hydrogenic species and plasma impurities, and experimentally validate it: Previous efforts were focused on modelling neutron and gamma emission in D and D–T plasmas [12, 13, 14, 15] due to their importance in global fusion roadmaps. While rates of fusion reactions on impurities are orders of magnitude lower than those of D–D or D–T fusion in conditions relevant for fusion reactors, they become dominant in so-called aneutronic plasmas, i.e. bulk H or He plasmas which at thermal temperatures produce charged and confined fusion products. However, if the plasma in addition to bulk ions contains a population of fast ions and impurities, a variety of nuclear reactions can be triggered, resulting in emission of charged particles, neutrons and gamma-rays [17, 18, 19]. H and He plasmas are envisioned to be used

in the diagnostics and plasma operations commissioning phases of future tokamaks [20], in which some level of intrinsic low-Z impurities, such as beryllium or boron, will be present. Knowledge of these nuclear reactions, supported by the capability to realistically model the emission sources, is important for radiation safety, and can be exploited to characterize and calibrate the response of nuclear diagnostics.

Interactions between fast ions and impurities in tokamak plasmas have not been modelled extensively in the past. There are several main papers published on this topic, which we summarize here – in [17] the Monte Carlo code ControlRoom has been used to model reaction rates and neutron energy spectra of ^{9}Be(^{3}He,n)^{11}C, ^{9}Be(α,n)^{12}C, and ^{9}Be(p,n)^{9}B reactions. Neutron emission from ^{3}He–^{9}Be fusion was found to be dominant in analysed experiments, and a synthetic time-of-flight spectrometer response was modelled. Be impurity concentration in the discharges was determined by adjusting the impurity density to match the measured neutron yield. In [13] the neutron yield and neutron energy spectrum for reaction ^{9}Be(d,nγ)^{10}B were modelled. In the paper a neutron spectrum anisotropy, induced by highly energetic deuterons generated via the three-ion RF scheme [21], was measured through neutron activation of indium and aluminium foils. Integrated modelling of foil activation was validated against the experiment, with the d–^{9}Be reaction computed to contribute up to 5 % to activation. In [19] the neutron yield in aneutronic plasmas of ITER's Pre-Fusion Power Operation (PFPO) phase is predicted, focusing on fusion between Be impurities and energetic fast ion, such as protons and ^{3}He. The analysis is based on predictive simulations with the ASTRA-NBI and TORIC-SSFPQL codes, with which the distribution functions of fast ions accelerated by NBI and ICRH was obtained. The fusion products' slowing-down was modelled via a stationary solution of the linearized Fokker-Plank equation. The authors calculate that in ITER's He commissioning plasmas significant neutron emission, with rates of up to 10^{15} s^{-1}, could be driven by interactions between fast protons and Be impurities, predominantly through ^{9}Be(p,n)^{9}B.

With the work presented in this paper we improve the complexity and fidelity of the integrated modelling workflow for characterising fusion on beryllium impurities in tokamak plasmas. The novelty of our modelling lies in the developed framework, coupling the TRANSP [22], JETTO [23], LOCUST-GPU [24], and DRESS [25] codes. With it we deliver a state-of-the-art model of the proton-beryllium fusion chain, capable of computing the fast ion distribution functions, spatially resolved 2D emissivity profiles, and energy spectra of all reactants and fusion products within the chain, as well as their interactions with background plasma. Calculated neutron emissivity properties of primary and secondary impurity-driven fusion reactions are used to derive a source description, which is coupled to the MCNP code [26] and applied to JET's neutron transport model. First-of-a-kind simulations of nuclear detectors' response to neutrons emitted from fusion on beryllium are then obtained with MCNP. In addition, we estimate the contribution of knock-on deuterons, generated via p-d inelastic scattering, to the neutron yield, and discuss the potential of triggering proton-boron reactions in JET-like conditions. Modelling results are validated against absolutely calibrated measurements of the neutron yield.

(iii) Re-evaluate and validate cross sections for fusion reactions between fast ions and beryllium plasma impurities: Non-standard fusion interactions have not been studied extensively in the past, and minimal work has been done to validate their cross sections in tokamak-relevant plasma conditions. This is necessary to facilitate the utilization of plasma impurity fusion for diagnostics commissioning and fast ion generation purposes, and can be relevant in other fields of scientific research, such as nucleosynthesis in astrophysics [27], and accelerator-driven irradiation therapy [28]. In support of the work presented in this paper, cross sections for neutron-emitting reactions between fast ions and beryllium, namely ^{9}Be(p,n)^{9}B, ^{9}Be(p,α)^{6}Li, and ^{9}Be(p,d)2α have been re-evaluated, and their uncertainty as-

sessed, pending inclusion in the FENDL nuclear data library [29, 30]. Newly evaluated cross sections are applied in this paper, validating the dominant ^{9}Be(p,n)^{9}B reaction against JET's absolutely calibrated fusion yield measurements. Cross sections of fusion reactions on Be impurities analysed in this paper are plotted in figure 1.

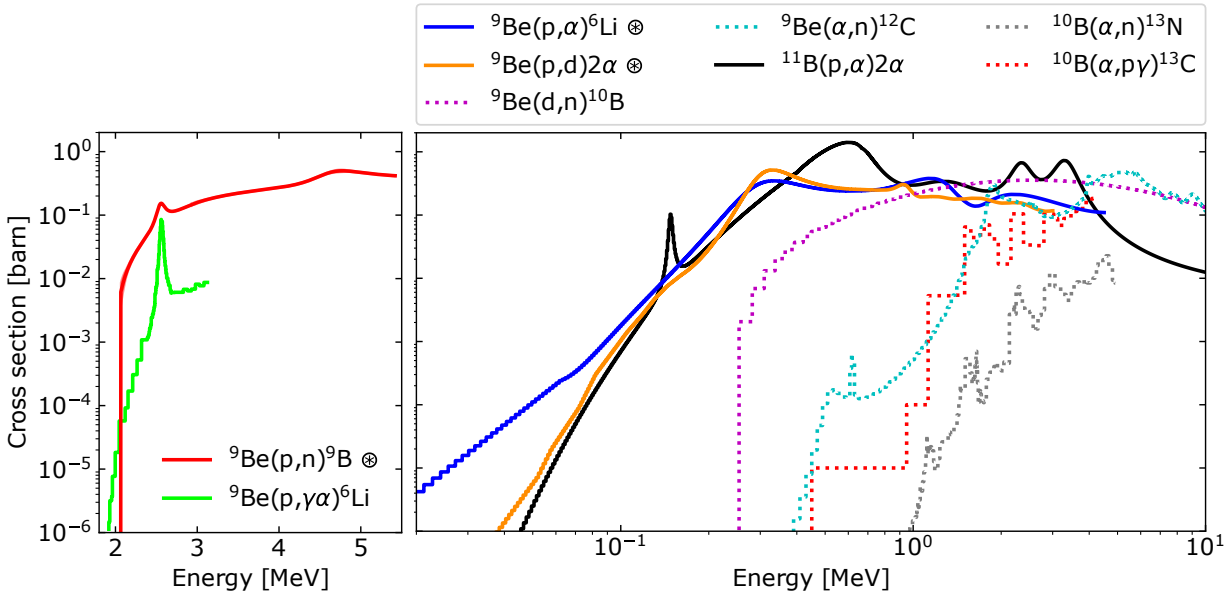

Figure 1: Cross sections of relevant reactions within the proton-beryllium fusion chain [29, 30], plotted against the impinging particle's centre-of-mass energy. Newly evaluated cross sections are denoted with ⊛. In the left panel cross sections of the two reactions dominating neutron (^{9}Be(p,n)^{9}B) and γ emission (^{9}Be(p,α)^{6}Li with $E_\gamma \approx 3.56$ MeV) are plotted. In the right panel cross sections of interactions between fast ions and boron are added [31, 20].

(iv) Provide input to energetic particle modelling codes: There is great interest in the fusion community for models capable of generating high fidelity source descriptions of energetic ions, i.e. distribution functions finely resolved in space, time, and pitch-energy. The fast ion birth functions are applied to studies of advanced plasma heating schemes [21, 32, 33], the effects of energetic ions on MHD stability [34, 35, 36] and plasma confinement [37, 38], fast ion diagnostics [39, 40, 41], and importantly alpha heating [3]. In this paper we couple TRANSP, LOCUST-GPU, and DRESS, developing the capability of enhancing a zero-orbit-width bounce-averaged fast ion distribution function with corrections for prompt losses and finite Larmor radius effects. With the modelling framework we additionally demonstrate generating realistic birth and slowed-down (thermalised) distribution functions for fast fusion products, deuterons and alphas, emitted in the proton-beryllium fusion chain.

The paper is structured as follows: in *Section 2* we describe the JET discharges developed to trigger and sustain proton-beryllium fusion in He and D, and detail the nuclear diagnostics measurements supporting this observation. In *Section 3* the modelling workflow is presented, describing the modelling tools used, and detailing the validated diagnostics used for the preparation of input and their fits. In *Section 3.1* we describe the results of predictive impurity modelling with JETTO, and the calculation of proton distribution functions with TRANSP-DRESS, both needed to compute the primary set of proton-beryllium interactions. This is followed by the modelling of fast fusion products, deuterons and alphas, and the fusion reactions these trigger with the impurity in *Section 3.2*. We also construct a model for the proton-deuteron inelastic scattering and its effect on the neutron emission in D plasmas. In *Section 3.3* the computed total neutron

yield is validated against fission chamber measurements, followed by a discussion on the computational uncertainty. The coupling of the modelled proton-beryllium neutron source to MCNP and JET's neutron transport model is demonstrated in *Section 4*. Calculations of neutron fluxes and neutron energy spectra for selected nuclear detectors are shown and compared against standard D-D and D-T plasma sources. In *Sections 5* and *6*, the discussion and conclusions section, we highlight the novelty and findings, followed by a description of future work and modelling suggestions. We comment on how fusion reactions between energetic ions and plasma impurities could be utilized in future reactors, including an assessment of the feasibility of using proton-boron fusion to generate and study energetic alpha particles.

2. Experimental observations

In the experimental section we first detail the development and plasma parameters of targeted proton-beryllium He and D plasma discharges performed at JET, followed by an analysis of nuclear diagnostics' measurements identifying neutron emission from the p–Be fusion chain as the dominant fusion yield drive.

2.1. Experiment summary

Dedicated experiments were performed in JET's 2022 *C43* He and 2023 *C45* D campaigns targeting conditions in which a non-negligible source of ionizing radiation in otherwise aneutronic plasma is created, unambiguously and in a sustained way driven primarily by neutron and gamma emission via the proton-beryllium fusion chain. He plasmas were initially chosen for developing the scenario, primarily due to their relevance for the planned commissioning role within ITER's PFPO phase, for which they were predicted to achieve the highest neutron rates through fusion on impurities [19, 42]. An energetic population of protons was generated in the experiments by employing RF heating at the fundamental frequency of a puffed H minority, while Be impurities were inherently present in JET due to its Be/W metal wall. To facilitate an effective evolution of a fast proton tail and increase the concentration of Be relative to n_e, plasma density was decreased as much as permitted by safety limits. In order to prevent parasitic absorption of RF power on beam ions, and keep the plasmas in L-mode, no additional NBI was applied, with the exception of diagnostics blips in D pulses for charge exchange measurements.

We focus the analysis on four representative discharges from a set of 14 performed in total: #101184 and #101185 in He, #103598 and #105453 in D. A summary of their plasma parameters is shown in figure 2. All discharges were performed at 1.45 MA, while the magnetic field was varied between 2.2 T and 2.8 T. H minority RF heating was applied throughout a 9 second interval with P_{RF} varying between 4 MW and 5 MW. The RF frequency was adjusted to place the resonance layer on the magnetic axis, set to 32.2 MHz and 42.5 MHz, depending on the B-field. Note that in #101185 the magnetic field was 2.5 T while the RF frequency was intentionally kept at 42.5 MHz to push the resonance off-axis. In D discharges diagnostics NBI blips were employed to measure T_i, Ω_{tor}, and the concentration of low-Z impurities. Note that applying NBI blips was not possible in He plasmas due to higher beam shine-through compared to D at low densities. Relatively low plasma density was established in both He and D pulses, with core line integrated n_e varying between $2.5 - 3.5{\cdot}10^{19}$ m^{-2}, and on-axis n_e of $\approx 1.5{\cdot}10^{19}$ m^{-3}. High electron temperature was sustained throughout the heating phase of all discharges, the profiles being strongly peaked with on-axis T_e of up to 9 keV. As seen in panels *g* and *h* of figure 2 regular sawtooth activity was induced in all discharges with a short sawtooth period of ≈ 170 ms. Ion temperature in all pulses was constant at just above 2 keV. Plasma effective charge was high in the heating phase of the four pulses, reaching values of around 5 in He and 4 in D. The concentration of hydrogen was maintained between 2 – 3 % to enable efficient coupling of RF power to the minority. Panels *m* and *n* display time traces of the measured total neutron rate – He discharges are seen to achieve a maximum R_n of $\approx 6{\cdot}10^{13}$ s^{-1} with steady-state fusion sustained over an

interval ≥ 5 s. After the start of RF heating at 10 s the neutron yield is seen to evolve on the time scale of a second, governed by the slowing-down time of fast protons and variation in plasma density. In discharge #101184 the strong dependency of fusion yield on P_{RF} can be seen, where an RF deterioration in the interval [12.3, 13.8] s leads to a 20 % reduction in R_n. In panel *m* hydrogen discharge #91667, the previous experiment triggering transient conditions with dominant proton-beryllium fusion via RF heating, is plotted for comparison [18]. Neutron rate in D pulse #103598 is characterized by baseline emission at $\approx 3{\cdot}10^{13}$ s^{-1} driven by RF heating, interspersed with beam-target D-D fusion blips driven by D-NBI ions which are additionally accelerated by second harmonic RF heating. Due to the parasitic D-D neutron emission being intricately intertwined with proton-beryllium fusion in this discharge, it is analysed solely for its charge exchange diagnostics measurements. Following an initial deterioration of RF heating in D pulse #105453, an asymptotic exponential rise of neutron emission can be observed after 12.3 s, plateauing at $\approx 6{\cdot}10^{13}$ s^{-1}. This is followed by a step change to P_{RF} from 4 MW to 2 MW in order to display the effect of a decaying fast proton distribution function on neutron emission. A singular NBI diagnostic blip was introduced at the end of the pulse to avoid contamination of the fusion yield by beam-driven D-D fusion. The pulse intervals for which integrated modelling of neutron emission was performed are denoted with dashed lines.

Four main actors were employed to develop plasma conditions that facilitated the evolution of an energetic proton tail, with it maximizing proton-beryllium fusion – RF power, plasma fuelling, H puffing, and magnetic field. Namely, via controlling P_{RF} and fuelling plasma collisionality and RF power density are defined, while B-field adjustments result in changes to the location of the RF resonance layer and affect fast ion confinement through orbit effects. Plasma current could be increased to further improve confinement and with it fusion performance, however this would results in an increase in plasma density, which would dampen the proton tail evolution. Experiments to test this interplay of I_p effects were not executed. In the left-hand side graph of figure 3 the scenario optimization process leveraging the four actuators is shown for the proton-beryllium experiments in He and D. On the *x*-axis the ratio between RF power and H concentration is plotted, while the *y*-axis displays a normalized (maximum) ratio of $T_e^{1.5}/n_e^2$, which is inversely proportional to the product of collisionality and electron density – representing the combined effects of RF power and fuelling actuators on the formation of a proton fast tail. The symbol shape categorizes pulses with respect to magnetic field, and the symbol colouring represents a whole-discharge average of the total neutron rate. Conditions favouring an energetic fast proton tail exist when quantities on both *x*- and *y*-axis are maximized, meaning low collisionality, low plasma density, and high RF power density per proton ion. One can observe that both the He and D pulse development branches have started out at low actuator values and consequently low fusion performance, followed by a scenario optimization route which led to a higher performance domain in the upper right-hand side of the graph. The isolated effects of three actuators on the fusion performance of four consecutive He discharges are addressed in the graph, denoted with black arrows. A 25 % reduction in line integrated n_e is highlighted first, performed at a fixed RF power to proton ratio, which resulted in an increased collisionality proxy and an ≈ 50 % fusion yield rise. This is followed by an increase of the magnetic field from 2.2 T to 2.8 T, which drove a 20 % increase in core T_e through improved fast ion confinement, resulting in an increase in neutron rates of almost a factor of 2. In the final optimization step the RF power was increased by 25 %, improving both P_{RF}/n_e and RF power per proton, increasing the neutron yield by another factor of 2 in the best performing proton-beryllium discharge #101184 (red-edged symbol). In the last He discharge #101185 (blue-edged symbol) the magnetic field was reduced to 2.5 T at a fixed RF frequency, dislocating the RF resonance layer to the inboard side, and inducing an RF power density and T_e decrease. With 5 MW of RF power coupled to relatively poorly confined fast ions, significant losses occurred which caused an increase in plasma density through interaction with plasma facing components, further reducing the collisionality proxy. Interestingly, the fusion performance

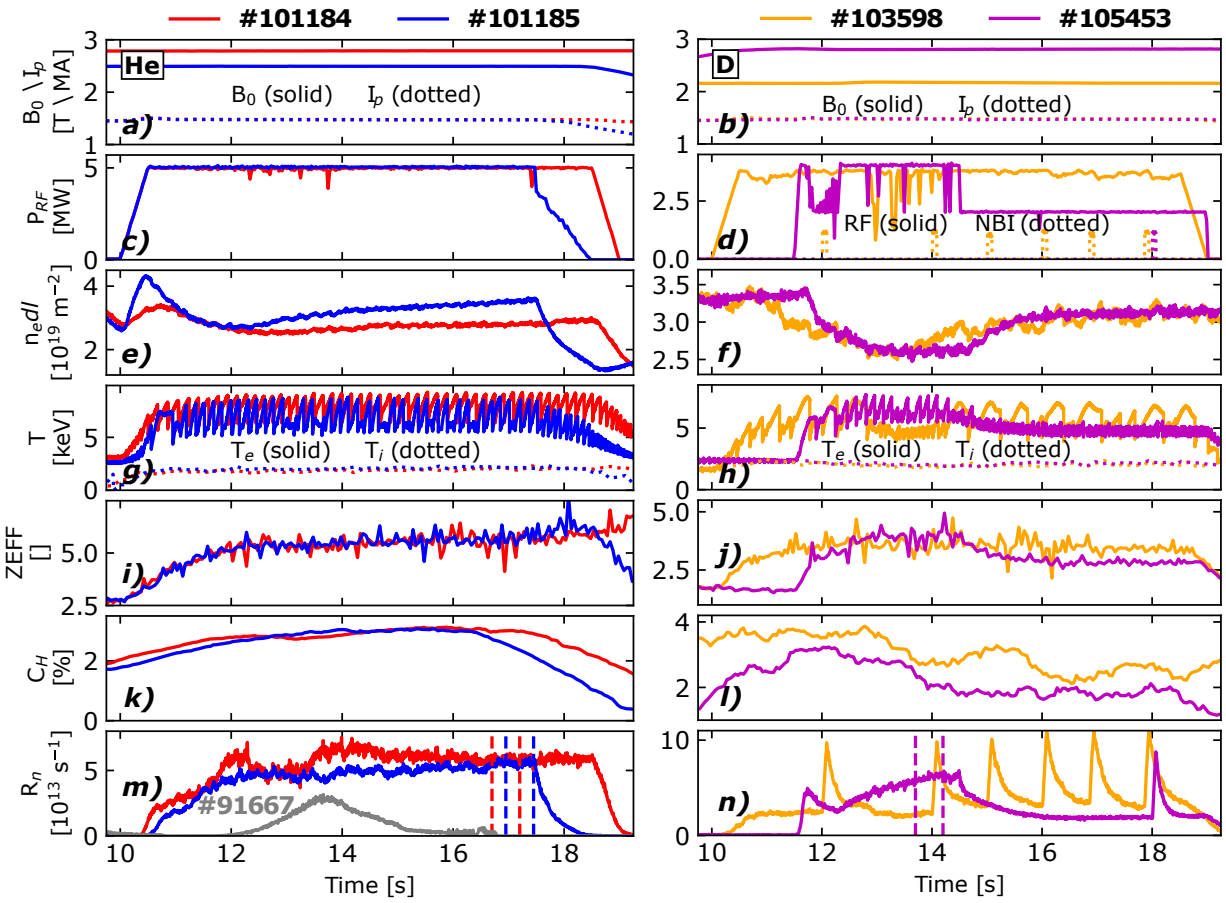

Figure 2: Overview of plasma parameters for He discharges #101184 and #101185 on the left, and D discharges #103598 and #105453 on the right. Panels *(a, b)*: vacuum field B_0 and plasma current I_p. Panels *(c, d)*: ICRH and NBI heating power. Panels *(e, f)*: plasma core line integrated electron density (interferometer measurements). Panels *(g, h)*: electron temperature on axis (electron cyclotron emission measurements), and core ion temperature (crystal x-ray spectrometer measurement). Panels *(i, j)*: plasma effective charge (visual spectroscopy). Panels *(k, l)*: H minority concentration (versus n_e, divertor gas analysis). Panels *(m, n)*: total neutron rate (fission chamber measurement). For comparison the highest achieved neutron rate in discharge #91667 is plotted in grey. The dashed vertical lines denote the intervals chosen for integrated modelling of individual discharges.

was partly recovered due to increased Be concentration driven by the wall interaction. The best performing D pulse #105453 (magenta-edged symbol) is seen to have achieved collisionality and RF power to proton ratio values comparable to the highest performing He discharges, including the fusion performance.

In the right-hand side graph of figure 3 the integral neutron yield for the entirety of JET's 2022 *C43* He campaign is plotted against pulse number on the *y*-axis, and the maximum heating power on the *z*-axis (P_Ω+P_{NBI}+P_{RF}). Targeted proton-beryllium pulses denoted with stars are an obvious outlier, having achieved the campaign's largest fusion yields, three orders of magnitude higher than the campaign average yield of $\approx 2{\cdot}10^{11}$ neutrons/s, denoted with the red dashed line. In aneutronic He plasmas the presence of a baseline neutron yield level is a strong indication of a presence of trace levels of D or T fuel due to fuel mixtures in preceding experimental campaigns [43]. Further supporting this is the fact that the recorded neutron yield is seen to be largely independent of P_{heat} as well as core T_{i}, meaning that the fusion performance is not driven by bulk plasma ions but rather residual fuel, the kinetic profiles of which depend strongly on wall heat loading, plasma fuelling, and fuel retention, the interaction of which is not explicitly

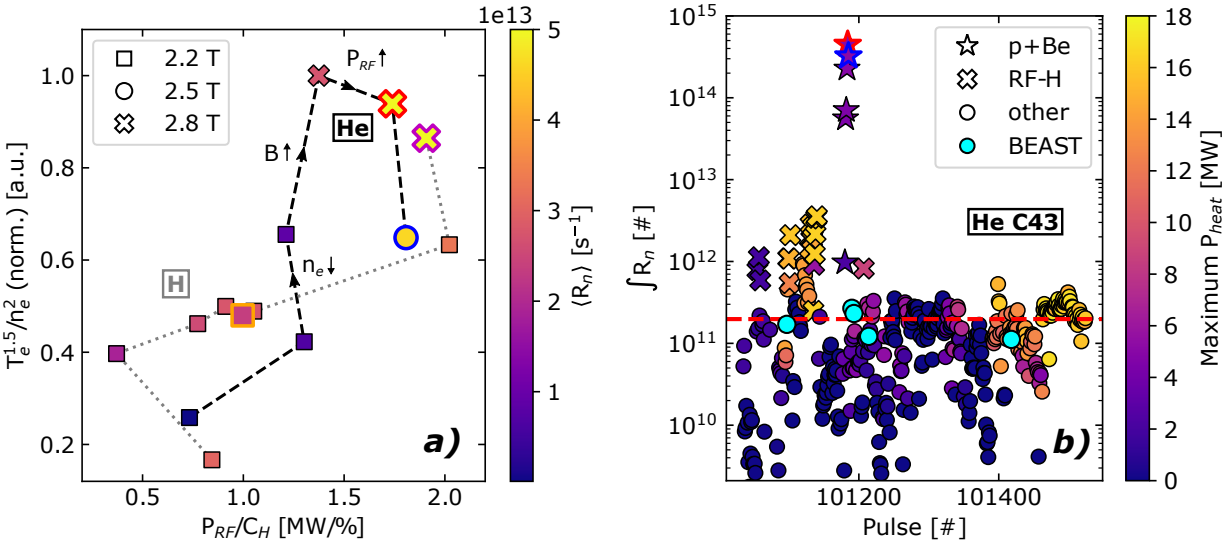

Figure 3: Panel *(a)*: ratio of electron temperature over electron density ($\propto \nu_{\rm eff}^{-1} n_{\rm e}^{-1}$) versus the ratio between injected RF power and hydrogen minority concentration, for proton-beryllium experiments in He (black dashed line) and D (grey dotted line). The z-axis (colorbar) denotes whole-pulse averages of measured total neutron rate. The varying levels of vacuum magnetic field are denoted with symbols shapes, with the four pulses modelled in the paper marked with individual symbol edge colours: #101184 in red, #101185 in blue, #103598 in orange, and #105453 (magenta). The effects of changes in plasma actuators $n_{\rm e}$, B_0, and $P_{\rm RF}$ on the scenario performance are shown for He pulses with arrowed lines. Panel *(b)*: Time-integrated neutron yield versus pulse number for the entirety of JET's 2022 *C43* He campaign database. The z-axis (colorbar) denotes maximum heating power in a discharge. The targeted proton-beryllium discharges are denoted with stars, pulses in which H RF minority heating resulted in increased neutron rates are marked with x-symbols, with other He discharges in circles. Cyan-coloured circles denote pulses modelled with BEAST to estimate the residual concentration of D and T in the plasma. Two He pulses modelled in the paper are marked with individual symbol edge colours: #101184 in red, and #101185 in blue. The red dashed line represents a whole-campaign mean neutron yield.

controlled in the experiment. A separate set of discharges is highlighted with x-symbols in the right panel of figure 3 – these are pulses in which the fusion yield is seen to be systematically higher than the average value by around an order of magnitude. The performance increase is driven by the use of RF H minority heating in these discharges, importantly in the termination phase in which $P_{\rm NBI}$ (12 MW in flat-top phase) was turned off, followed by a transition from H- to L-mode and a decrease in density with the plasma heated only by 3.5 MW of RF. Thus, unintentionally, conditions favourable for the evolution of an energetic proton tail were established, triggering a transient fusion yield rise assumed to be dominated by proton-beryllium fusion.

2.2. *Nuclear diagnostics measurements*

Apart from fast protons, highly energetic deuterons, generated by parasitic absorption of RF heating via the second harmonic resonance or as secondary fusion products in the proton-beryllium fusion chain, are the only other candidate that could trigger neutron and gamma emission in the dedicated p–Be experiments. To support the claim that proton-beryllium fusion was dominant in the selected three discharges, data of relevant nuclear detectors at JET is analysed and evidence detailed. The measurements presented below confirm two critical criteria, namely:

(i) Presence of fast protons in the energy range needed to trigger proton-beryllium fusion, and the absence of fast deuterons at significant concentrations — provided by two neutral particle analysers (NPA), the fast ion loss detector (FILD), and magnetic coils through MHD activity measurement.

(ii) Signature of fusion products emitted either via proton-beryllium fusion, or secondary reactions with Be triggered by primary fusion products -– provided by gamma spectrometers, and fission chambers.

2.2.1. Neutral particle analyser

The neutral particle analyser (NPA) utilizes a nonperturbing method to measure radial profiles of hydrogenic isotope ratios and their energy distributions, making it an optimal tool for inferring fast ion characteristics [44]. The diagnostics measures flux and energy spectra of neutral atoms escaping the plasma, after they've undergone charge exchange neutralization. Our analysis relies on JET's low-energy NPA, which enables diagnosing H and D neutrals simultaneously along a horizontal midplane sightline in JET's Octant 3. Note that NPA cannot distinguish between He and D atoms in it's deuterium channel, because of their identical atomic mass over charge ratio. The NPA was set to measure in the RF minority energy range, which for protons extends over 150 keV – 740 keV, and 125 keV – 370 keV for deuterons/helium-4. The measurements of H and D/^{4}He neutral flux over particle energy are shown in figure 4 for two He discharges #101184 and #101185, and D discharge #105453. Several major conclusions can be drawn – the H RF minority neutrals display a prominent fast ion tail in all three discharges, extending up to maximum detection energy. Note that for #105453 the high-energy NPA data is also available and corroborates the low-energy results, showing a proton energy tail extending up to the detector's maximum range at 1.1 MeV. The flux intensity differs for the two He discharges because of the RF resonance position being shifted inboard of the magnetic axis in #101185 and poorer fast particle confinement, however the energy spectra shapes are close to identical. We observe a difference between the He and D discharges energy spectra below $\approx$ 300 keV, where He discharges show a larger relative density of fast ions. This is the result of an enhanced H acceleration in He compared to D plasmas with similar RF parameters, due to the lower ion density and larger mass. However, the slopes of measured H fluxes at $\gtrapprox$ 0.5 MeV are similar for all three discharges, with a proton tail effective temperature of $\approx$ 200 keV. Importantly, deuteron channel measurements show that in He discharges fast deuterons or alphas were present at negligible concentrations – in #101184 and #101185 the D channel intensity is three orders of magnitude lower than that of H, on the limit of NPA detectability. On the contrary, the signature of a non-negligible population of fast deuterons is observed in D pulse #105453, which arises through a combination of p-d elastic collision energy transfer (knock-on effect) coupled with second harmonic deuteron acceleration, which is expanded on and modelled in Section 3.2.3.

2.2.2. Fast ion loss detector

The fast ion loss detector measures the pitch angle $\theta = \cos^{-1}(v_\parallel/v)$ versus gyro-radius distribution of lost ions impinging on a scintillator plate, located within an in-vessel aperture at machine coordinates of R_{maj} = 3.850 m and Z = –0.277 m [45, 46]. FILD measurements for the two He discharges #101184 and #101185, and D discharge #105453, which were averaged over the highest fusion yield discharge phases, are shown in figure 5. The basic characteristics of the detected fast ion losses are shared between the three discharges – we observe enhanced losses surrounding the pitch angle that corresponds to the location of the first harmonic H RF resonance layer (denoted with solid red lines), where the major radius R_{RF} at the ion bounce reflection and the pitch-angle of the FILD grid are related through $\theta = \arcsin(R_{\mathrm{RF}}/R_{\mathrm{FILD}})^{1/2}$. The wide distribution of detected losses varying in pitch angle from 50$^{\mathrm{o}}$ to 70$^{\mathrm{o}}$, outlined for pulse #101184 with a dashed white line, indicates that the distribution functions of the lost fast particles are broad in pitch angle. The broad loss formation is a signature of fast proton prompt losses, the majority of which is expected to originate from the trapped-passing particle boundary. Importantly, the energy range of lost protons varies between 0.7 MeV to beyond 3.5 MeV, which confirms the successful generation of a significant populations of MeV-range fast protons in these experiments. The observable difference between the measurements is in

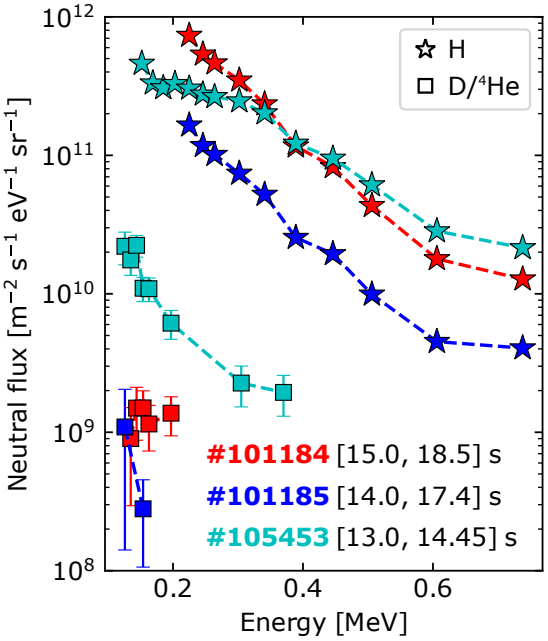

Figure 4: Neutral particle analyser measurement of neutral flux vs. energy for protons (stars) and deuterons/alphas (squares) for two He discharges #101184 and #101185, and D discharge #105453. The low-energy NPA detection limit is below neutral flux of $\approx 10^9$ $m^{-2}s^{-1}eV^{-1}sr^{-1}$. The measurement averaging windows are specified.

the recorded intensity of the enhanced ridge of losses at $\theta \approx 55^o$, which is driven by strong MHD activity in these discharges. The enhanced losses ridge is weakest in #105453, which is expected since the RF power applied was lowest of the three discharges, resulting in a less energetic proton population. In comparison, the signal intensity in #101184 is approximately three times higher due to the 25 % higher RF power, with a clear proton losses peak seen at energies of around 1.2 MeV. In #101185 B_T was reduced to push the resonance layer off-axis, which resulted in an overall poorer confinement of wide energetic proton orbits. Indeed, the intensity of losses is the highest in this discharge, an order of magnitude higher than #101184. In pulse #101185 the ridge of increased losses peaks at $\approx$ 1.7 MeV – due to the large peak intensity the underlying broad distribution of prompt losses can not be seen on this scale, however is visible in short intervals of MHD quiescence. The amplitude of losses at energies above 1 MeV in #101185 confirms that MHD-enhanced losses of highly energetic protons are the cause for the formation of a hotspot on the Be limiters, absent in the other two discharges.

Deuterons and alphas generated through proton-beryllium fusion in these discharges are born at energies of $\gtrapprox$ 0.5 MeV, and $\gtrapprox$ 1.5 MeV, respectively. Because fusion products are quasi-isotropic in pitch, the expected footprint of losses of these particles would coincide with the broad distribution seen in the FILD measurement in figure 5. However, with fusion product densities being approximately four orders of magnitude lower compared to the H RF minority, their contribution to FILD's response is negligible.

2.2.3. MHD activity

Signatures of a prominent fast ion population can be observed indirectly through the MHD activity measured by JET's in-vessel magnetic pickup coils. In all the low density He and D discharges discussed in the paper there are clear signs of MHD modes driven by the highly energetic ion population, with the observed activity being similar across all shots. In figure 6 the MHD spectrogram for He discharge #101185

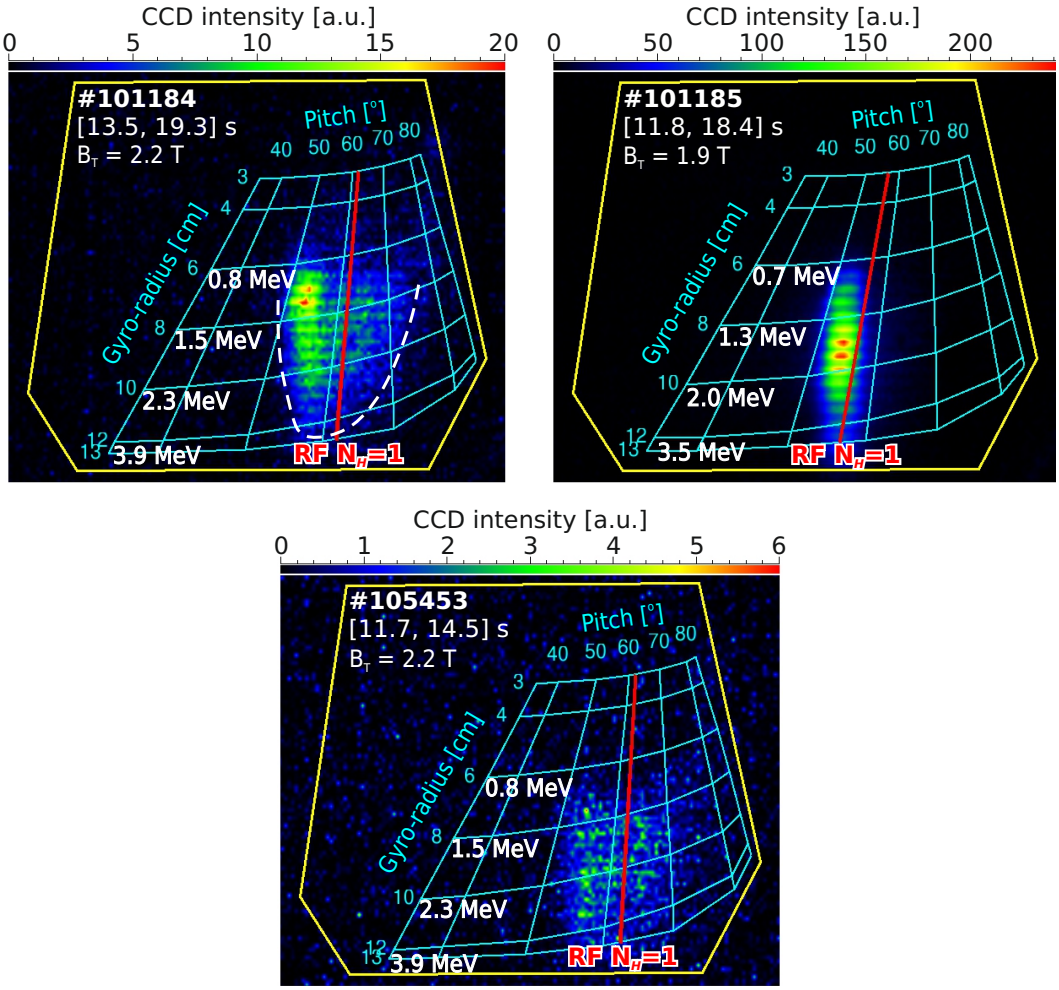

Figure 5: Fast ion loss detector measurements of the pitch angle (top axis, in degrees) vs. gyro-radius (left axis, added corresponding proton energies - identical for alphas, factor 2 lower for deuterons) distributions of ion losses for two He discharges #101184 and #101185, and D discharge #105453. The ion losses amplitude is represented via the measured CCD intensity. The measurement averaging window and toroidal field at the location of FILD are specified. The position of the first harmonic H RF resonance layer in relation to the pitch angle is denoted with the red line.

is shown and the main modes are identified. The significant population of highly energetic protons present in these plasmas destabilised several Alfvén eigenmodes. Toroidal Alfvén eigenmodes (TAEs) [47] with toroidal mode numbers n = 1 to 6 and frequencies 170 kHz – 280 kHz were driven sufficiently strongly by fast protons to exhibit pitchfork splitting, a non-linear modulation of the mode frequency. Data from the reflectometer [48] indicates that the TAEs are located near the plasma edge, enabling efficient transport of fast particles, such as trapped protons with wide banana orbits, on to lost trajectories. At 340 kHz – 460 kHz elliptical Alfvén eigenmodes (EAEs) [49] were excited throughout the pulse with toroidal mode numbers n = 2 to 6. EAEs were not seen on the reflectometer, indicating they are located at the very edge of the plasma, beyond the reflectometer's radial scan. In the highest frequency range of 530 kHz – 620 kHz, non-triangularity-induced Alfvén eigenmodes (NAEs) [49] were excited with negative toroidal mode numbers –6 to –1, indicating the modes were excited by either a hollow fast particle profile, anisotropy, or positive energy gradients in the proton distribution. The reflectometer suggests the NAEs are located in the

core region of the plasma on both sides of the magnetic axis, from 2.4 m < R_{maj} < 3.4 m. Additionally, n = 0 modes were observed simultaneously in both the TAE and EAE frequency ranges. The reflectometer data suggests the axisymmetric modes are located at the very edge of the plasma, near the pedestal. The simultaneous observation at several frequencies, and location near the plasma edge indicates that the axisymmetric modes were global Alfvén eigenmodes (GAEs) [50] below two different continuum branches. n = 0 modes are destabilised by either anisotropy or positive energy gradients in the fast proton distribution function, which are produced by sawtooth crashes. At approximately 70 kHz, high frequency fishbones appeared throughout the pulse. Like Alfvén eigenmodes, fishbones are also able to eject fast particles from the plasma, despite their location near the centre of the plasma [51]. Alfvén cascades are also observed during the pulse, indicating a flat or reversed q-profile. FILD's loss spectrograph [52] shows strong correlation between fast ion losses and edge TAE activity, and to a lesser degree core fishbones.

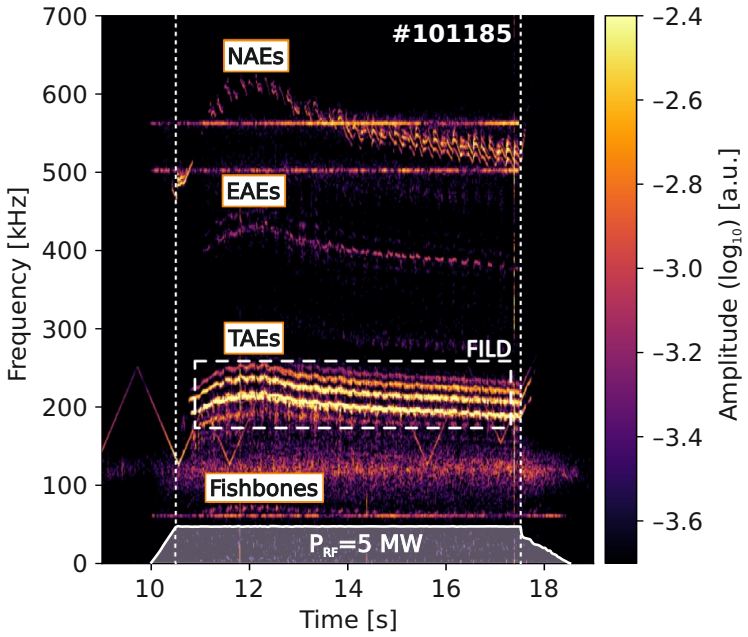

Figure 6: MHD spectrograph of the perturbed magnetic field measured at the plasma edge for He discharge #101185. Unstable TAEs, EAEs, NAEs and fishbones are identified, driven by various features of the RF-accelerated fast proton minority. Horizontal signals are artefacts from the ICRH antenna, while diagonal zigzags are an artefact from the TAE antenna. The RF power waveform is plotted in the bottom with the two dotted vertical lines denoting the flat-top interval at maximum P_{RF} = 5 MW. The dashed rectangle denotes the region of highest loss amplitude recorded by FILD, driven by TAEs.

2.2.4. Gamma spectrometers

A unique measurement of this experiment was produced by JET's $LaBr_3$ gamma spectrometers. Measurements of two detectors at different positions were used, namely one positioned in the roof laboratory with a vertical view of the plasma, and one located in the biological shield surrounding the torus hall with a tangential plasma view. Both have a relatively narrow line of sight into JET's octant 8, crossing the plasma close to the magnetic axis. In figure 7 we show a comparison of the measured gamma spectra, normalized by their integral values, for the D-^{3}He three-ion discharge #94701, two He discharges #101184 and #101185, and D discharge #103598. Note that in pulse #105453 the γ-spectrometers were not operational, therefore data for #103598 with matching plasma conditions is shown. The D-^{3}He discharge was chosen because of

its population of MeV-range deuterons, accelerated by a synergy of NBI and RF via the three-ion resonance scheme. These have been shown, experimentally and by modelling, to trigger fusion interactions with Be impurities in addition to the dominant deuteron-deuteron fusion [13, 53, 32]. As such it can be used as an example of a discharge in which fusion is fully driven by MeV-range deuterons, and contrasted against the fast proton dominated fusion drive observed in the low density He and D discharges. At the top of figure 7 the fusion reactions emitting signature gammas in these two plasma types are detailed. The reactions are split into two groups:

(i) Primary fast proton induced fusion with beryllium and deuterium (denoted with green lines): ^{9}Be(p,$\alpha\gamma$)^{6}Li with E_γ = 3.56 MeV [54, 55], ^{9}Be(p,γ)^{10}B with E_γ between 6.84 MeV and 7.75 MeV (multiple resonances with a broad composite peak) [56], and d(p,γ)^{3}He with $E_\gamma \approx$ 5.5 MeV [57].

(ii) Fusion reactions induced by fast deuterons and alphas, generated by either heating or as fusion products of p–Be reactions (denoted with orange lines): first branch of ^{9}Be(d,nγ)^{10}B with E_γ = 2.87 MeV, ^{9}Be(d,pγ)^{10}B with E_γ = 3.37 MeV, second branch of ^{9}Be(d,nγ)^{10}B with E_γ = 3.59 MeV, and ^{9}Be(α,nγ)^{12}C with E_γ = 4.44 MeV.

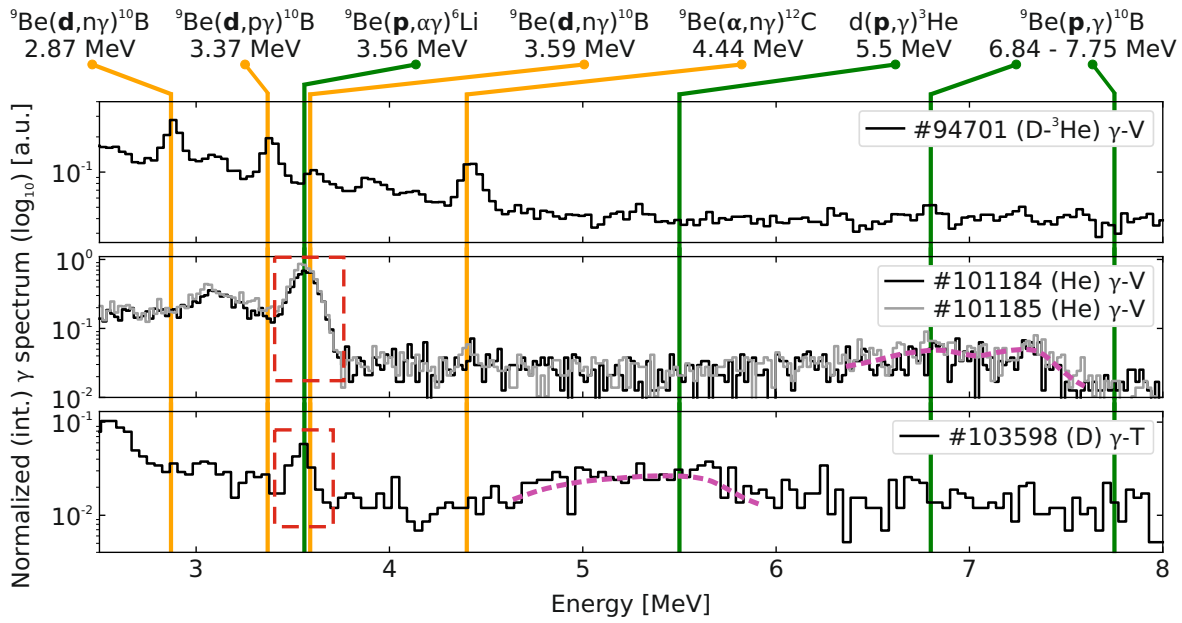

Figure 7: Comparison of normalized (integral) gamma spectra measured with the vertical (label γ-V) and tangential (label γ-T) $LaBr_3$ gamma spectrometers for the D-^{3}He three-ion discharge #94701, two He discharges #101184 and #101185, and D discharge #103598. The vertical coloured lines denote the energies of relevant gamma peaks emitted by fusion interactions between fast protons (green), deuterons (orange), and alphas (orange), with Be impurities. The red dashed rectangles highlight the primary proton-beryllium fusion gamma peaks. The broad gamma peak distributions of fast proton induced d(p,γ)^{3}He and ^{9}Be(p,γ)^{10}B reactions are denoted with a dashed magenta line.

The gamma spectrum for discharge #94701 displays prominent deuteron-beryllium fusion peaks, indicating that the significant fast deuteron population is driving not only the main D-D beam-target fusion, but also reactions with metallic impurities. In contrast, the measured spectra for He and D discharges show a landmark gamma peak at around 3.6 MeV (red dashed rectangles in figure 7), predominantly a result of gammas produced in proton-beryllium fusion. At a set detector energy resolution and count statistics, it is not possible to separate the contributions of ^{9}Be(p,$\alpha\gamma$)^{6}Li (cross section shown in figure 1) and the second

branch of ^{9}Be(d,nγ)^{10}B to the 3.6 MeV gamma peak. However, it is evident from the spectrum of #94701 that the relative intensity of the fast deuteron driven ^{9}Be(d,nγ)^{10}B 3.59 MeV peak is small compared to the peak intensity of the first branch of this reaction at 2.87 MeV, as well as that of the ^{9}Be(d,pγ)^{10}B peak at E_γ = 3.37 MeV. Since neither of these two reactions contribute significantly to the He plasma spectra, indicated by the absence of distinct peaks at corresponding energies in figure 7, we conclude that the supra-thermal deuteron population is not highly energetic and remains at low concentrations. This means that the contribution of the fast deuteron induced gammas to the composite peak at 3.6 MeV is expected to be insignificant. Because the ^{9}Be(p,$\alpha\gamma$)^{6}Li cross section resonance is located at proton energies of 2.6 MeV, as shown in figure 1, the strong presence of this peak in the gamma spectra and the large peak width, is direct evidence of a significant H population in the energy range of several MeV in the low density He and D plasmas. Another indication of a dominant fast H population in low-density He plasmas is the presence of a broad spectral formation between energies of around 6.5 MeV and 7.8 MeV (denoted with a dashed magenta line in the middle panel of figure 7). This is a result of gamma emission due to five resonances of the ^{9}Be(p,γ)^{10}B reaction, triggered by fast protons with energies between 0.2 MeV and 1.4 MeV. There is no corresponding composite gamma spectrum peak in the fast deuteron discharge #94701, due to the absence of a fast proton minority, or in #103598, which is mostly likely due to a lower fusion rate and resulting low counting statistics. Interestingly, in both D-^{3}He and He discharges the ^{9}Be(α,nγ)^{12}C alpha particle induced gamma peak at 4.44 MeV can be seen. In #94701 the alphas are emitted through fast deuteron and helium-3 fusion at birth energies of 3.6 MeV, while in the He discharges these are produced by ^{9}Be(p,$\alpha\gamma$)^{6}Li and ^{9}Be(p,d)2α fusion reactions with a broad birth energy distribution peaking at around 1.5 MeV. In the D-^{3}He discharge the alpha induced peak is more prominent due to the higher α-particle birth energy and higher alpha fusion yield. In majority-D discharge #103598 another spectral formation is observed (denoted with a dashed magenta line in the bottom panel of figure 7), peaking at around 5.5 MeV, which is driven by gamma emission through proton-deuteron fusion. Due to a monotonically rising d(p,γ)^{3}He cross section, the proton minority's energetic tail induces an emission peak with a low amplitude and large width.

The γ-spectrometer data was integrated over 200 ms intervals to obtain a time evolution of the gamma yield, which is compared against absolutely calibrated total neutron rates measured by fission chambers in figure 8. The gamma measurements were integrated over a selected energy interval, namely within [2.75, 7.75] MeV to cover all major gamma peaks for relevant reactions with beryllium. In addition, an integration solely over the ^{9}Be(p,$\alpha\gamma$)^{6}Li 3.56 MeV peak was done for the He pulses to assess the strength of the dominant gamma emission reaction driven by the fast proton minority. Due to a low count rate on the 3.56 MeV spectrum feature such a targeted integration could not be done for #103598. For pulses #101184 and #101185 the comparison shows good agreement between neutron and gamma rates within the experimental uncertainty, strongly indicating that the drive behind total neutron emission and the processed gamma signal is the same, i.e. primary fusion between the H RF minority and beryllium impurities. Analysing the isolated 3.56 MeV peak contribution showed that it is the dominant contributor to the total gamma yield within the relevant spectrum range, which occurs due to similar threshold energy and shape of ^{9}Be(p,n)^{9}B and ^{9}Be(p,α)^{6}Li cross sections, as shown in the left panel of figure 1. We observe that the γ-yields at the beginning of the He discharges are systematically lower compared to the neutron rates, and higher at the end of the heating phase. There are two main reasons for this, the first being that the ^{9}Be(p,$\alpha\gamma$)^{6}Li resonance is triggered by protons with energies of several MeV and slowing-down time of up to 3 seconds, meaning that the high energy proton tail evolves on a time scale of seconds and will therefore induce a gradually rising 3.56 MeV gamma yield. The second cause for this qualitative discrepancy is the difference in the cross sections of proton-beryllium fusion reactions dominating neutron and gamma emission, further affected by the properties of energy dependent fast particle confinement and MHD interaction. The ^{9}Be(p,γ)^{10}B

reaction is the second contributor to the plotted He plasma γ-yield, accessible to protons with lower energies, above several hundreds of keV. This reaction contributes to the integrated gamma yield throughout the discharges, with the contribution weakly decreasing as the average energy of the fast proton tail increases through the pulse. A good match between the neutron and gamma yield time trace is observed for pulse #103598 as well – gamma emission is seen to rise with the injection of D beams (neutron rate spikes) and decay in-between beam blips to the pre-injection emission levels. The latter is dominated by proton-induced fusion with beryllium, with the γ-emission boosted during NBI blips as a result of the fast deuteron population, injected at 80 keV and additionally accelerated through RF second harmonic resonant heating, interacting with the proton minority via d(p,γ)^{3}He fusion. We identify the elastic scattering of fast protons on bulk plasma deuterons [58] in the low-density D plasma discharges as an actor in further increasing the reactivity of γ-emitting proton-deuterium fusion, through knock-on acceleration and formation of an energetic deuteron tail.

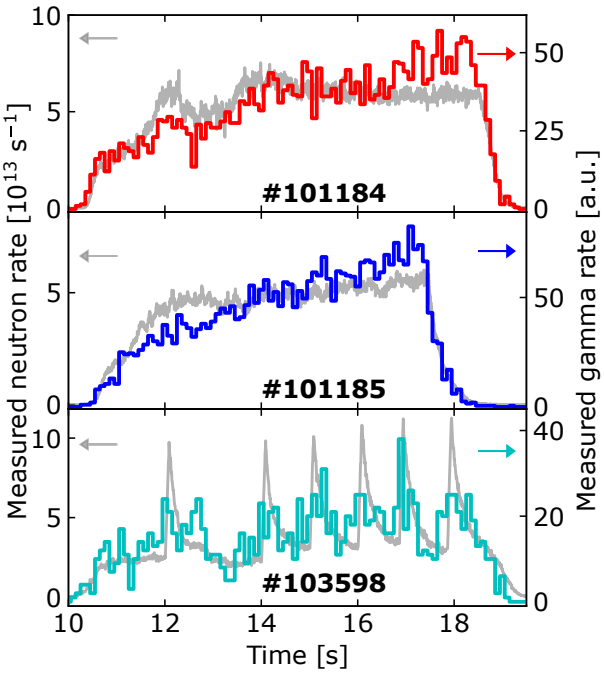

Figure 8: Comparison of the time evolution of measured total neutron rate (left axis, gray) and $LaBr_3$ gamma spectrometer response (right axis, coloured) for discharges #101184, #101185, and #103598. The γ-spectrometer data was integrated over time (200 ms interval) and gamma energy (interval 2.75 MeV – 7.75 MeV).

2.2.5. Neutron diagnostics

Absolutely calibrated fission chambers are used for measurements of fusion power independent of neutron energy, owing to their flat response function [59]. While this means the output signal caries no information on the spectrum of impinging neutrons, the dynamics of the fission chamber response provides implicit information on the characteristics of fusion ions that triggered the neutron emission [53]. For example, in plasma conditions where fusion is driven by a population of fast ions the neutron rise or decay rate, caused by a transient in the external heating power, is related to the fast ion slowing-down time. In the top panel of figure 9 the analysis of neutron decay rates for two heating transients with different dominant fusion drive in D discharge #105453 is presented. The emission rate is fitted with an exponential function e^{-t/τ_n},

with τ_n being the neutron emission decay constant. At 14.5 s a decrease in RF power from 4 MW to 2 MW was performed in #105453, which induced a slow neutron emission decay driven by the diminishing fast ion tail, the rate of which is dictated by the interplay between particles' slowing-down time and the energy dependency of the dominant proton-beryllium fusion cross sections. Fitting the neutron decay rate we obtain a time constant which represents an effective slowing down time of the fusion-inducing fast ions – the RF transient yields $\tau_n \approx 660$ ms. For comparison we analyse the decay rate of the D-NBI induced fusion power transient at 18.07 s, dominated by beam-target D-D fusion triggered by fast beam deuterons, additionally accelerated by RF second harmonic heating. Figure 9 shows that the fusion power decays significantly faster with beam-only drive, with a fitted τ_n of around 100 ms. Assuming the computed τ_n is proportional to the fusion-inducing ions' slowing down time, the ratio of effective source particle energies in the two transients can be assessed via the Spitzer formulation, which is E_0(RF)/E_0(D-NBI) = 8.4. NBI and RF heating synergy has been experimentally and computationally shown to reliably produce fast ion tails with energies of several hundred keV [33, 13]. Applying the calculated ratio of seed particle energies, we deduce that the energy of fast ions dominating fusion at peak neutron performance in discharge #105453, i.e. beginning of the RF power transient, was in the MeV range, providing further evidence that proton-beryllium fusion was the primary source of detected neutrons. Because the fast ion slowing-down is $\propto T_e^{3/2}$, traces of T_e are shown for the two transient events at two core radial locations in the bottom panel of figure 9. The ratio between electron temperatures for the RF and D-NBI transients, averaged over the fitting interval, is approximately 1.09. No isolated transient events were triggered in the He pulses.

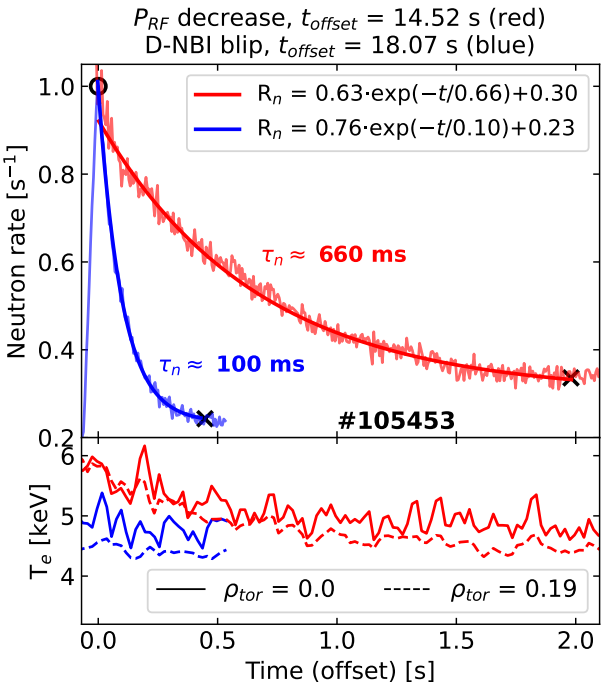

Figure 9: *Top:* Exponential fits of neutron emission decay constant τ_n following an RF power decrease (red, 4 MW → 2 MW) and a CXRS diagnostic D-NBI blip (blue) based on absolutely calibrated fission chambers measurements in D discharge #105453. Beginning and end time of fitting windows are denoted with circle and cross symbols, respectively. *Bottom:* Time traces of electron temperature fits at the magnetic axis, and at the location of neutron emission peak of $\rho_{tor} = 0.19$. The time axis is offset to align with the start of the neutron rate decay.

The time-of-flight neutron spectrometer (TOFOR) measures energy spectra of neutrons emitted from

the core of JET's plasmas, sharing its line-of-sight with the vertical gamma spectrometer [60]. The detector is sensitive to signatures of fusion induced by RF-accelerated ions with increased perpendicular velocity components and large Larmor radii. Similarly to the gamma spectrometer, TOFOR can resolve components of neutron spectra arising through various fusion reactions due to signature peaks of energy emission. While the spectrometer would in principle be able to discriminate between proton-beryllium, D-D, and D-T neutrons, the fusion yields in dedicated proton-beryllium experiments were too low to achieve sufficient TOFOR counting statistics. Similarly, owing to the low neutron rates, neutron emissivity profile could not be captured by JET's neutron camera [61].

3. Integrated modelling

A bespoke integrated modelling methodology has been developed with the purpose of accurately modelling neutron emission in selected He and D discharges, which is a combination of primary proton-beryllium fusion, secondary fusion product interactions with beryllium, and parasitic deuteron-triggered fusion. A diagram of the modelling workflow is shown in figure 10, it comprises five steps:

1. Interpretive plasma modelling with TRANSP [62] was performed using JET diagnostics measurements as input. The TORIC RF wave solver [63] was used in combination with the Fokker–Planck Program (FPP) code [64] to compute the pitch/energy distribution functions of H RF minority. JETTO-SANCO [23, 65] simulations were run, predictively evolving the impurity ion channel to determine the plasma composition.
2. FPP computed proton distribution functions were resampled and input into the LOCUST GPU code [24] to correct for prompt losses and account for finite Larmor radius effects.
3. LOCUST corrected proton distribution functions were input into the DRESS code [25] to calculate the characteristics of primary proton-beryllium fusion products (green colour coding).
4. DRESS calculated birth distributions of deuterons and alphas (bold blue) produced in primary proton-beryllium fusion were resampled and input into LOCUST to model the slowing-down of these energetic ions and obtain thermalised FIDFs (orange colour coding).
5. LOCUST thermalised fusion product FIDFs were looped back into DRESS to calculate the characteristics of the secondary proton-beryllium fusion products and sum up the primary and secondary neutron emission contributions into a joint neutron source. Non-negligible contributions of parasitic fusion reactions with deuterons to the neutron emissivity were modelled and combined with the proton-beryllium source (violet colour coding).

Neutron emission modelling was performed for one time interval in each of the selected discharges, at steady-state conditions and highest fusion performance, i.e. [16.7, 17.2] s for He pulse #101184, [16.95, 17.45] s for He pulse #101185, and [13.7, 14.2] s for D pulse #105453, as shown in figure 2. The thermal energy confinement time is around 170 ms for these discharges, which means the analysis time intervals are a multiple of ~ 3 of $\tau_{e,th}$. In the following sub-sections, split between plasma modelling, fusion product modelling, and experimental validation, we discuss the details of individual workflow steps and analyse the results obtained.

3.1. Plasma modelling

The prescribed input for interpretive TRANSP and predictive JETTO modelling was prepared in the following way: electron density and temperature profile fits were based on high resolution Thomson scattering (HRTS) [66] and electron cyclotron emission data [67] (ECE, covering core and edge regions) as constraints.

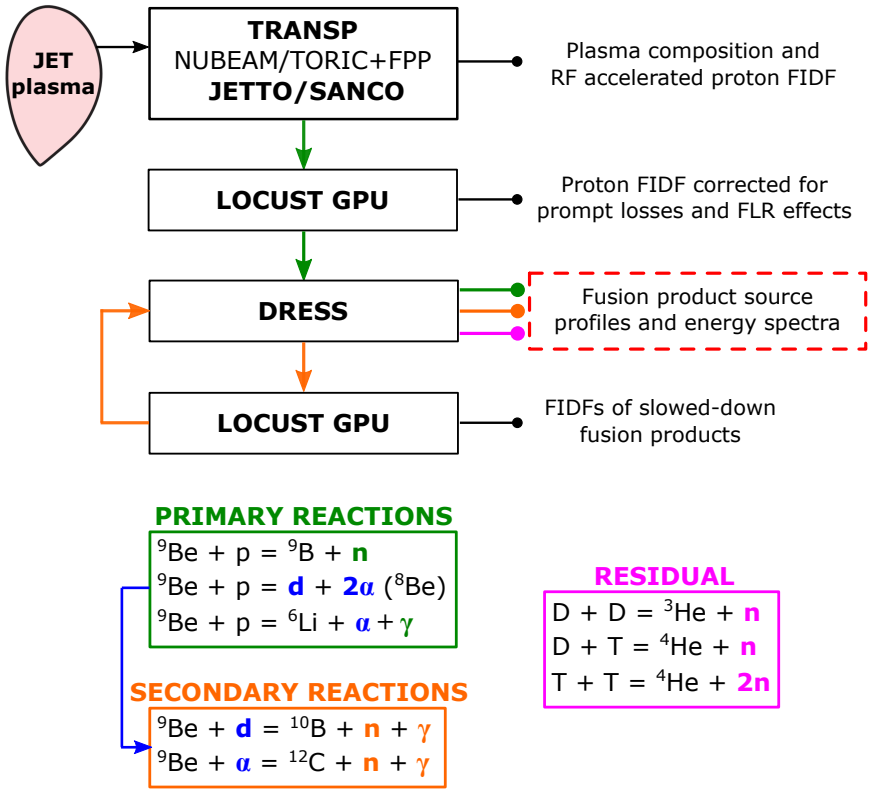

Figure 10: Diagram of the developed workflow to model fast ion distribution functions (FIDFs) of RF-accelerated protons and fusion products, and calculate neutron source characteristics – emissivity profiles and energy spectra – in proton-beryllium fusion dominated discharges. Proton-beryllium interaction triggers a two-stage process, with neutrons and gammas produced by both direct fusion and through secondary fast ion production. The colour coding refers to the primary (green) or secondary (orange) reaction stage that is being computed within the workflow. The workflow includes neutron emission contribution due to the presence of residual D and T (violet).

Thomson scattering n_e measurements were additionally cross-calibrated against the absolutely calibrated interferometer line-integrated density. Profiles were fitted with a cubic spline suitable for L-mode plasmas, with a comparison between measurements and fits shown in figure 11. He discharge #101184 was chosen as an example, with n_e and T_e shown in panels *(a)* and *(b)*. The ion temperature and toroidal plasma rotation were prescribed based on fits from core charge-exchange recombination spectroscopy (CXRS) diagnostics for main and Ne impurity ions [68, 69, 70] (good agreement between the two channels is observed). CXRS data for He discharges was not available due to beam shine-through being too high at relatively low main ion densities, i.e. factor of 2 lower compared to D discharges at same electron density. The charge-exchange diagnostics data was instead obtained and validated for discharge #103598, the D-equivalent compared to the original He discharges (all the global parameters with the exception of the main ion species are matched). In discharge #103598 six diagnostic D-NBI blips at 1 s intervals were employed, in addition to diagnostic neon puffing to enable core CXRS measurements. In addition to T_i and Ω_{tor} profiles, Be and Ne impurity densities were also measured. The equally spaced diagnostics beam blips show that measured profiles for all quantities evolved minimally throughout the RF heated phase of the discharge and were steady-state. To interchangeably use ion temperature and rotation fits obtained in D plasma for He discharge modelling, high-resolution crystal X-ray spectrometer (XCS) [71] measurements on ^{26}Ni were analysed, available for

all discharges. XCS measured T_i in D plasmas matches CXRS data within experimental uncertainty, and also coincides with He discharge XCS T_i in similar plasma conditions, which is shown in panel *(c)* of figure 11 (magenta square denotes #101184 XCS measurement, all other data is for #103598). He T_i profiles were obtained by scaling the D plasma profile fits by the ratio of XCS measurement $T_{i,He}(XCS)/T_{i,D}(XCS)$, measured at $\rho_{tor} \approx 0.25$. The same procedure was applied to the toroidal rotation measurements in #103598 and their scaling for He discharges, shown in panel *(d)* of figure 11.The fit uncertainty was calculated as the combination of two uncorrelated uncertainties, namely the deviation of the fit from the available measurement constraints, and the uncertainty of the measurements. In average the former were below 5 %, while the measurements uncertainty varied between 5 % – 10 %, which yields an approximate 1σ fit uncertainty of $\sim$ 10 %.

The equilibrium and safety factor were taken from an EFIT++ time-evolved reconstruction constrained by an extended magnetics suite and TRANSP computed pressure profiles, i.e. including kinetic profile fits and the contribution of RF fast ions, as well as a q=1 inversion radius constraint based on ECE measurements [72, 15]. The equilibrium was applied to kinetic profile data mapping and was fully prescribed in all modelling codes. We observed a consistent match between the equilibrium-reconstructed boundary location and the one inferred by density and temperature edge measurements, and agreement between the EFIT++ and TRANSP/JETTO calculated plasma stored energy. Sawteeth were not explicitly modelled in TRANSP, meaning that potential recombination-triggered redistribution effects on fast ions, such as increased transport of particles dependent on plasma radius and pitch-energy distribution functions, were not taken into account [73]. Magnetic reconstruction shows that the discharges' q-profiles within $\rho_{tor} \sim 0.4$ were relatively flat with q_0 close to 1 throughout. Neutron traces shown in panels m and n of figure 2 show no evidence of the sawteeth affecting fusion performance. Since this is driven by fast protons, the observation could indicate that: *(i)* the sawtooth phase is short enough compared to the proton slowing down time that the fast proton distribution does not recover from effects of adjacent crashes and is saturated by the sawtooth-particle interaction redistribution throughout the pulse, or *(ii)* that the redistribution/losses of fast protons due to frequent reconnection events are low and do not significantly alter their density profiles or energy-pitch distribution – owing to the fact that protons with energy high enough to trigger neutron-emitting p-^{9}Be fusion are likely trapped, with wide orbits located in the vicinity or outside of the sawtooth inversion radius. The implicit effect of sawteeth on particle slowing-down time due to the induced collapse of core electron temperature is accounted for via the prescribed T_e profiles. Any additional MHD-driven losses of fast protons are similarly not modelled, e.g. fishbone-induced core-localized losses. These were, however, shown to have a relatively small effect on the particle energy or magnetic moment of RF-accelerated H in JET hybrid experiments, in which wall hotspots were similarly observed [51].

3.1.1. Plasma impurity modelling

The fidelity of the calculation of proton-Beryllium fusion rates is linearly proportional to the estimate of Be concentration and its uncertainty. Additionally, the fusion rate evaluation is dependent on the impurity dilution through the role it plays in determining the concentration of the puffed H gas in the core. We have determined the plasma composition using a combination of diagnostic data, and impurity transport modelling. The analysed He and D discharges are non-standard from the viewpoint of their low electron density and high energy fast ion population. This results in a naturally higher concentration of intrinsically present JET metallic wall impurities, and in the increased strength of wall impurity sources due to fast ion losses. Plasma facing components most exposed are beryllium limiters, nickel-coated RF antenna elements, and the W divertor tiles. These contribute to an increased effective charge in the analysed discharges, compared to what is observed in He and D plasmas with more conventional plasma parameters, i.e. Z_{eff} of just above 2 and 1, respectively. The plasma composition calculation was done for a mix of main ions,

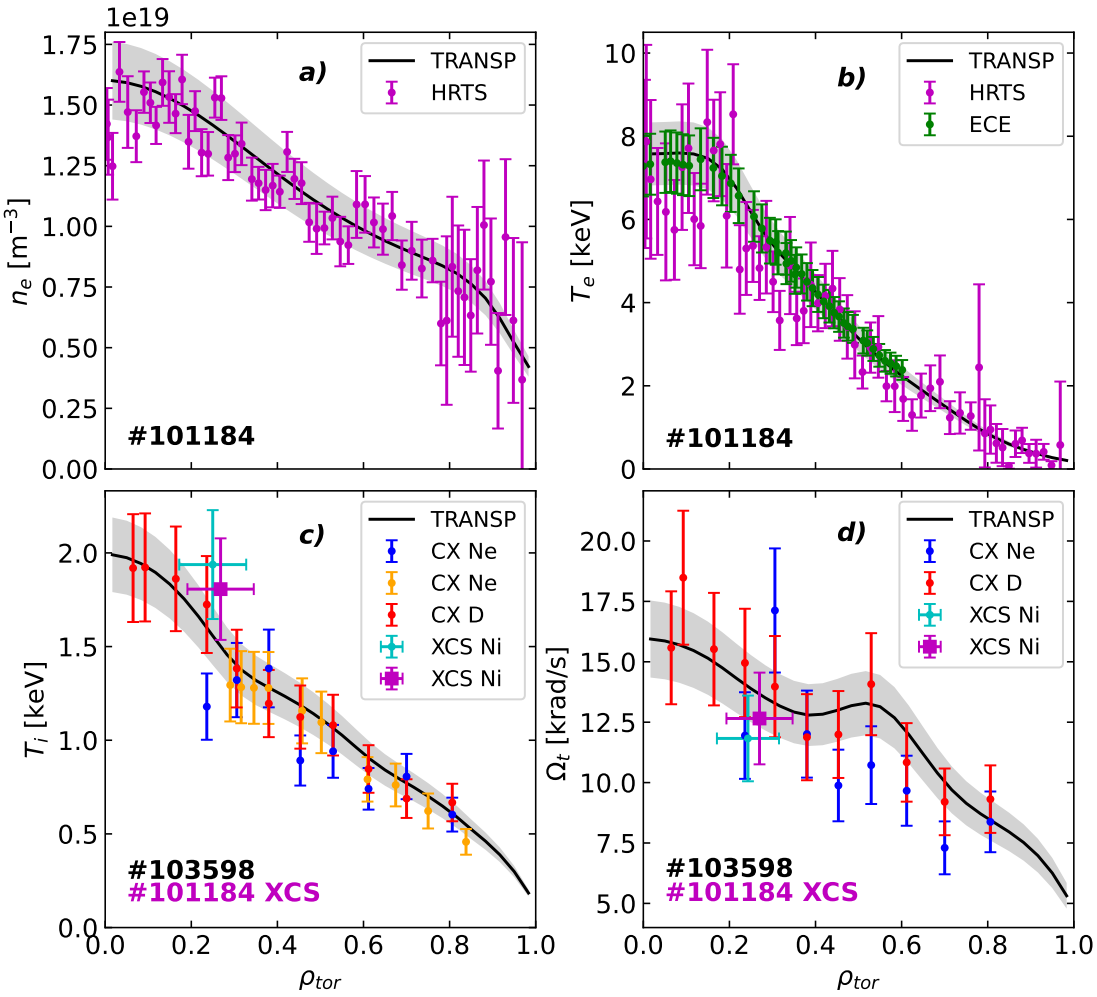

Figure 11: Comparison between measurements and fits (solid black) used as input in TRANSP and JETTO simulations for L-mode discharges #101184 in He, and #103598 in D (averaged over modelling intervals). Panels – *(a)*: electron density with HRTS measurements; *(b)*: electron temperature with HRTS and ECE measurements; *(c)*: ion temperature with CXRS (main D and impurity Ne ions) and XCS measurements (#103598 cyan, #101184 magenta); *(d)*: toroidal rotation with CXRS (main D and impurity Ne ions) and XCS measurements (#103598 cyan, #101184 magenta). The TRANSP's native ρ_{tor} radial coordinate, i.e. root of the normalized toroidal magnetic flux $\sqrt{\Psi_{tn}}$, is on the x-axis. The grey shaded areas denote a 10 % profile fit uncertainty.

beryllium, neon (only puffed in D discharges), nickel (mid-Z representative including a contribution from iron), molybdenum, and tungsten, via the following steps:

1. *Predictive modelling of impurity density and charge profiles*: the experimental data fits were input into JETTO, which was run predictively on the impurity ion channel using SANCO with the aim of obtaining impurity density profile shapes. Impurity transport was determined by a combination of NCLASS (neoclassical – note that due to T_i gradients, Ω_tor, and collisionality being low NCLASS is expected to perform well for high-Z impurities) [74], and Bohm-GyroBohm [75] and TGLF-SAT2 [76] (turbulent) models, with turbulent transport found to be dominant. Satisfactory agreement was found between the measured low-Z impurity density profiles and the whole-radius gradient-driven TGLF prediction, while the Bohm-GyroBohm particle diffusion coefficient was multiplied by a factor

of 0.6 to reproduce the experimentally observed density gradients. The boundary condition at the separatrix was set such that the net particle flux crossing the separatrix was matched by the inward flux, which is suitable for steady-state conditions in which the impurity densities are approximately constant in time. Baseline ADAS year 89 [77] was used for analysing nickel and tungsten to ensure comparability with the analysis of vacuum ultra-violet (VUV) [78] measurements. A combination of improved ADAS data for Ni and W, namely year 41 [79] and 50 [80], was used to evaluate the impact of different ADAS data on plasma composition and the associated uncertainty. For molybdenum line power data from ADAS year 42 methodology [79] was used. For light impurities ADAS year 96 [81] was employed.

2. *Diagnostics constraints*: Be and Ne profiles were obtained via CXRS measurements in D discharge #103598, averaged over all available diagnostics blips and fitted. Measurements show that both impurities have a flat concentration profile and that these remain constant throughout the discharge. The measured Be and Ne profile shapes are computationally reproduced by JETTO-SANCO. Because plasma conditions in #103598 are matched in He and D discharges, the Be and Ne profile fits were directly adopted in their modelling. Due to increased fast ion losses and the formation of hotspots on the Be limiters in He discharge #101185, the Be concentration in the time interval of interest is expected to be higher than in steady-state conditions of #103598 and #101184. Because limiter hotspots developed in the last several seconds of the discharge, the conditions at the beginning of the pulse can be considered equivalent to the D discharge. Therefore in #101185 the Be density was adjusted to account for the difference in the measured Z_{eff} between the beginning of the heating phase and the interval of interest. With this we imply that the observed increase in Z_{eff} throughout #101185 is solely the consequence of an increase in the Be source due to the fast ions' interaction with the wall. Constraints for nickel and molybdenum volume averaged densities were obtained through VUV emission spectroscopy analysis [78]. The profile shapes were taken from JETTO-SANCO predictive simulations and were rescaled (radially constant) to match the $\langle n_{\mathrm{imp}} \rangle_{\mathrm{V}}$ VUV constraint. W content, with its profile shape computed by JETTO-SANCO, was determined by matching the total integral radiated power measured by bolometry. The computed total radiation profiles were additionally compared against tomographically reconstructed bolometry profiles – both measurement and calculation show a flat radiation profile over the whole radius for all discharges.
3. *Quasi-neutrality and effective charge profiles*: The constrained mix of impurity profiles and the electron density fits were plugged into the quasi-neutrality equation to obtain the main ion species solution and calculate the effective charge profile. The H RF minority concentration was measured by the residual gas analysis diagnostics, located in the sub-divertor plenum [82] – this is an edge measurement done relative to the hydrogenic and He species, which means it needs to be adjusted for impurity dilution and extrapolated to the core, while a flat concentration profile was assumed with respect to n_{e}. In all discharges residual D and T were present. While in bulk D discharges their content could be obtained from residual gays analysis, indicating T concentrations of around 1.4 %, in He the abundances were too low for relevant diagnostic statistics. Deuterium and tritium concentrations were therefore estimated by running BEAST (low-fidelity TRANSP) for multiple discharges within the He campaign with various levels of heating and density, in which D-D and D-T fusion were the only contributors to the total fusion yield (see discharges in cyan in figure 3). The mixture, additionally constrained by T measurements done as part of post-T and D-T operation removal of tritium [43], was adjusted to provide a match between the measured and computed total neutron yield, giving an estimate of $\approx$ 0.5 % D and 0.01 % T, consistent across the modelled set of He pulses. Similarly to H, a flat concentration profile was assumed for D and T. The computed total Z_{eff} was compared against

visible Bremsstrahlung measurements as the final consistency check.

In figure 12 the computed Z_{eff} and density profiles, and the radiated power of individual main ions and impurities are presented for discharges #101184, #101185, and #105453. The effective charge calculations (solid black) in panels *(a, b, c)* can be seen to match the measured values (red shaded area) well over most of the plasma radius. An uncertainty of ± 0.5 is assumed for the measured Z_{eff}, in which we've combined the contributions of the nominal measurement uncertainty, spread of the data over the flat-top phase, and a radial component to the uncertainty due to the measurement being line-integrated. The latter is dependent on the visual spectrometer's line-of-sight and the measurement sensitivity scaling with $n_{\text{e}}^2/\sqrt{T_{\text{e}}}$, with the measurement being most representative of a radial interval $\rho_{\text{tor}} \approx [0.5, 0.75]$. The computational Z_{eff} uncertainty was estimated to be around 15 % in the core and up to 30 % at the edge. The increased uncertainty in the vicinity of the separatrix is driven by the relatively large spread of HRTS n_{e} measurements at the edge, evident in figure 11, and the lack of impurity constraints in this plasma region. The edge Z_{eff} profiles beyond $\rho_{\text{tor}} \gtrapprox 0.9$ can thus be seen to rise steeply, a consequence of it being proportional to the ratio of the modelled flat impurity density profiles and decreasing n_{e}, as seen in panels *(d, e, f)* of figure 12. Ni, Mo, and W are computed to contribute most to Z_{eff} in the analysed discharges, with the volume averaged $\Delta\langle Z_{\text{eff}}\rangle \approx 1$ for all three impurities. This means that the Ni and Mo densities, due to an increased background abundance at low densities and fast ion-wall interaction, are of the order of 10^{16} m^{-3}, resulting in high core concentrations of around 0.1 %. The W density and concentration are computed to be approximately an order of magnitude lower. Panels *(g, h, j)* of figure 12 display a good match between the measured and computed P_{rad} within the estimated uncertainty for all three discharges. Tungsten is seen to contribute to the radiation most, while molybdenum and nickel contribute ≈ 35 % and $\lessapprox$ 15 %, respectively. We found that the difference in the estimated radiated power between ADAS year 89 and 41 & 50 data for tungsten is significant, with calculated P_{rad} approximately a factor of two higher for modern libraries. This is reflected in P_{rad} computational error bars – the low value has been set to ≈ 25 % due to the uncertainty in the volumetrically important edge tungsten density, while the upper uncertainty at ≈ 50 % is driven by ADAS data differences.

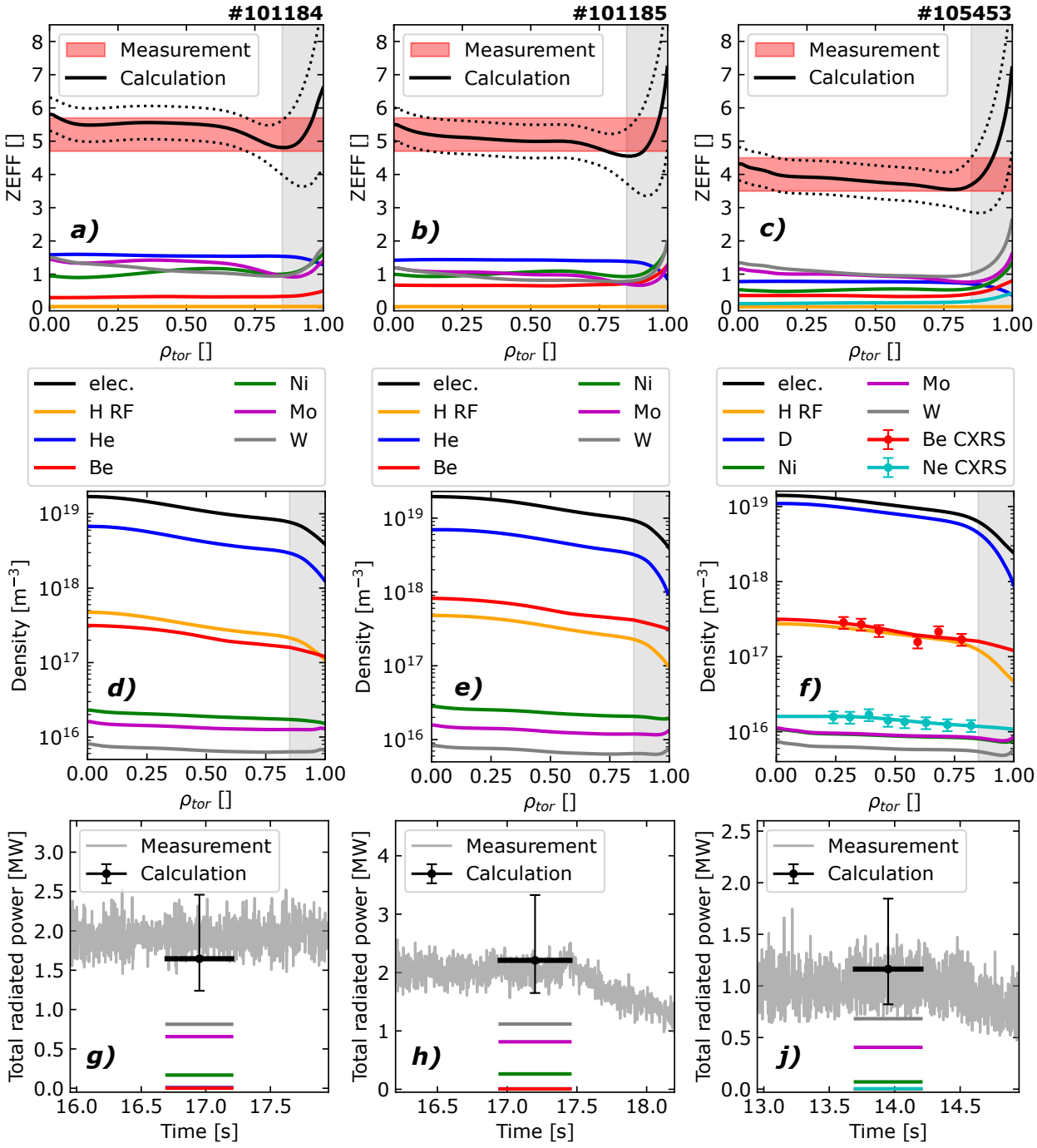

Figure 12: Results of plasma composition analysis for discharges #101184 and #101185 in He, and #105453 in D (corresponding to vertical rows of plots). Panels *(a, b, c)*: comparison between measured (red shaded) and computed Z_{eff} (solid black with dotted uncertainty lines) with individual isotopes' contributions. Panels *(d, e, f)*: density profiles based on fits of measurements (electrons, H minority, Be, Ne), JETTO modelling (Ni, Mo, W), or quasi-neutrality (He, D). Be and Ne density CXRS measurements obtained in D discharges are shown in panel *f* (red and cyan error bars). Panels *(g, h, j)*: comparison between measured (gray) and modelled radiated power with individual contributions (total P_{rad} in black). Plasma edge region at $\rho_{\text{tor}} \geq 0.85$ is denoted with shaded grey areas. Colour coding of impurities is consistent in graphs of the same discharge.

A comparison between H RF minority and Be concentration profiles is shown in figure 13. Hydrogen concentration is seen to vary between 2 – 3 % for the three discharges, and has a prescribed flat concentration profile. In the region of highest proton-beryllium neutron emission (grey shaded interval in figure 13) Be concentration is approximately 2 % for pulses #101184 and #105453, while it is a factor of two higher for #101185. The concentration increases up to around 8 % at the separatrix. While an edge density estimate for Be is not available for these experiments, high peripheral concentrations of $\approx$ 10 % have been reported in previous proton-beryllium studies at JET [18]. In view of the main aim to model the neutron source properties of proton-beryllium fusion, a high uncertainty of the edge Z_{eff} and Be concentration calculation is not a concern, because the contribution of neutron emission beyond $\rho_{\mathrm{tor}} > 0.75$ to the total yield is negligible.

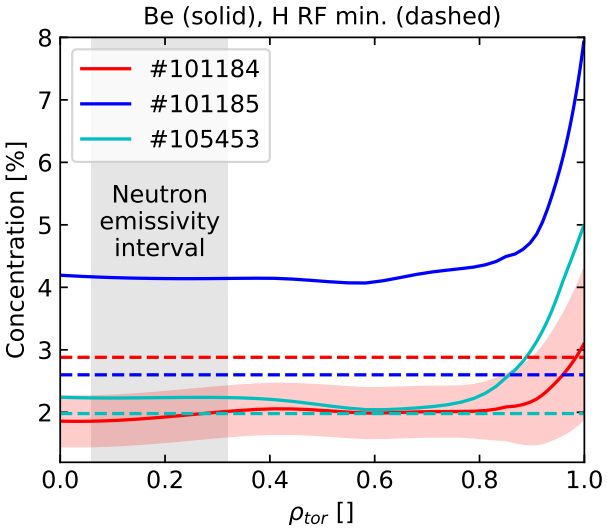

Figure 13: Comparison of H RF minority (dashed) and Be impurity (solid) concentration profiles for discharges #101184, #101185, and #105453. Be concentration uncertainty is shown with the red shaded area for #101184, increasing from 20 % in the core to around 30 % at the separatrix. Radial interval $0.06 \leq \rho_{\mathrm{tor}} \leq 0.32$ within which the majority of proton-beryllium neutrons are emitted is denoted with a grey shaded area.

3.1.2. RF H minority modelling

TRANSP-TORIC simulations were performed for discharges #101184, #101185, and #105453 to calculate the balance between RF power deposition on the H minority and other plasma ions, and to obtain an initial estimate of a radially resolved fast proton pitch-energy distribution function. The computed RF power balance for all discharges shows that $\approx$ 85 % of P_{RF} was coupled to the H minority, with the order of percent coupled to thermal bulk He and D, a negligible amount to the impurities, and just over 10 % directly to electrons. The computed RF resonance locations are shown in the left panel of figure 14. For both #101184 and #105453 the fundamental H resonant layer, coinciding with the 2^{nd} harmonic He and D resonances, is aligned with the magnetic axis. In #101185 the H resonance is shifted inboard, approximately 30 cm radially from the magnetic axis, which increased the volume onto which the RF power was deposited, consequently decreasing power densities on the fast protons.

Plots of plasma energy density profiles for the three discharges are shown in the right panel of figure 14. Comparing the total energy density (solid) and the perpendicular component of the RF energy density (dashed, $\propto v_{\perp}^2$), one can observe that for all pulses the integral amount of core energy stored in the RF-

accelerated protons is significant compared to the total energy, indicating an efficient coupling of RF power to the proton minority. Energy density profiles are distinctly peaked for the two He discharges due to localized RF absorption – in #101184 the peak is located at $\rho_{\mathrm{tor}} \approx 0.13$ corresponding to the energy carried by highly energetic protons with trapped orbits. In #101185 the peak is shifted off-axis to $\rho_{\mathrm{tor}} \approx 0.21$, resulting in a lower RF energy density component compared to the total plasma energy. #105453 is seen to have a broader energy density profile in the vicinity of the axis, potentially indicating a higher fraction of energetic passing protons compared to trapped ones, in addition to the lower profile amplitude, due to the 20 % lower P_{RF} in D pulses compared to He. W_{dia} averaged over the modelling interval for individual pulses was 2.7 MJ in #101184, 2.0 MJ in #101185, and 2.1 MJ in #105453.

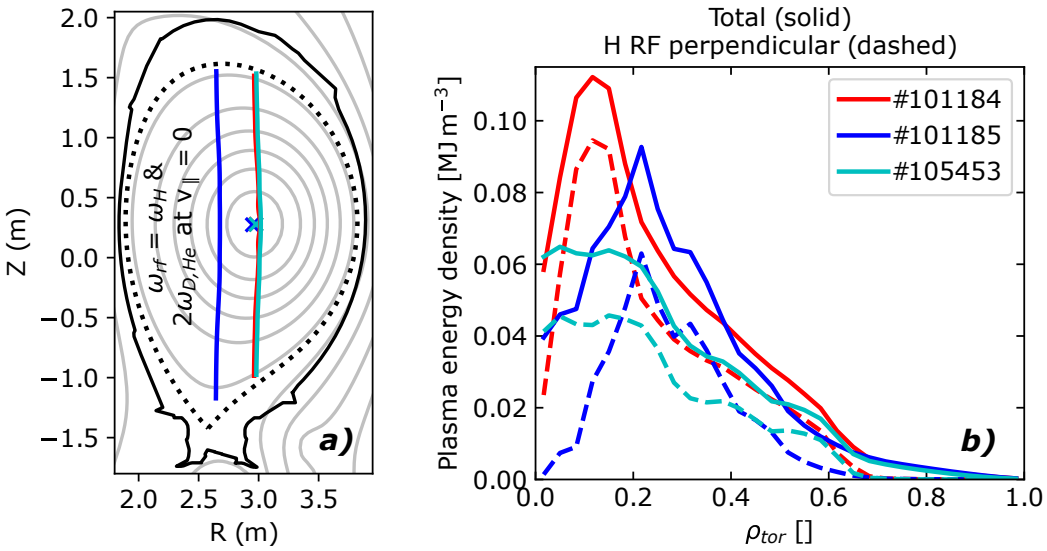

Figure 14: TORIC results for discharges #101184 and #101185 in He, and #105453 in D. Panel *(a)*: N=1 hydrogen and N=2 deuterium RF resonance layers at zero parallel velocity. Enclosing the plot are plasma boundary (dotted black) and JET limiter (solid black). Panel *(b)*: comparison of total (solid) and H RF perpendicular (dashed) energy density profiles.

Fast proton distribution functions $f_{\mathrm{p,rf}}$ are calculated by the Fokker-Planck Program (FPP) within the TRANSP-TORIC-FPP workflow [64]. FPP provides a bounce-averaged solution to the Fokker–Planck equation, dependent on plasma radius ρ_{tor}, particle energy E, and pitch p. It is flux-surface averaged, and does not have a self-collisional operator, using the assumption that all background species are Maxwellian. FPP computed distributions of RF-accelerated fuel ions have been applied to JET modelling before to calculate D-T yields in discharges employing RF heating of a large D minority at the fundamental frequency [83, 15]. Because a zero-orbit width approximation is used within FPP, the calculated $f_{\mathrm{p,rf}}$ were coupled to the orbit tracking LOCUST-GPU code [36] to correct the FPP distribution function for finite Larmor radius effects, prompt losses, and to spatially resolve the orbits with respect to major radius R_{maj} and the tokamak vertical axis Z. The coupling was achieved by random sampling on the order of 10^7 proton particles from the FPP $f_{\mathrm{p,rf}}$, uniformly in (R_{maj}, Z, E, p), and tracking individual orbits with LOCUST, having prescribed background plasma parameters from TRANSP. Sample particles were simulated for up to 10 ms, with collisions neglected. Note that because RF wave coupling is not computed in LOCUST some types of orbit losses might not be accounted for, e.g. specific high energy parts of phase-space would not be populated by RF-accelerated H due to losses occurring at lower energies. In figure 15 core H RF minority $f_{\mathrm{p,rf}}(E, p)$ are shown for He discharge #101184 as computed by FPP (panel *(a)*) and subsequently enhanced by LOCUST

(panel *(b)*). As expected, the FPP distribution function is isotropic in pitch at low proton energies due to the dominant collisional slowing down in the vicinity of source Maxwellian particles, whereas at higher energies two tails form, symmetrical in pitch, around $p \approx \pm\ 0.2$. These represent the favourably accelerated trapped ions whose banana orbit tips lie in the RF resonant layer. The FPP energy scale extends up to energies of 10 MeV, over which the high energy tail density decays by approximately 1.5 orders of magnitude. Such a low value of $\partial f_{\mathrm{p,rf}}(E)/\partial E$ indicates favourable conditions for the formation of a highly energetic RF proton tail, however also emphasizes the need for assessing high energy proton losses using full-orbit tracking, crucial for ions with large Larmor radii (protons at 5 MeV exceed gyro-radii of 10 cm in conditions of pulse #101184). Coupling $f_{\mathrm{p,rf}}(E, p)$ to LOCUST results in large differences to the distribution function. Most notably the counter-passing particle population between pitch angles of $\approx$ 0.1–0.3 exhibit significant losses at energies higher than 4 MeV due to unconfined orbits. The positive pitch angle branch retains its shape and is broadened due to orbital redistribution in (R_{maj}, Z) space, however the energy gradient of the distribution function is increased with particle densities at energies higher than $\approx$ 5 MeV being approximately an order of magnitude lower compared to the FPP $f_{\mathrm{p,rf}}(E, p)$. The occurrence of a tail at negative pitch values of $\approx$ 0.55 is predicted, which is an orbit effect explained through local migration of fast protons from the trapped-passing boundary to fully counter-passing particles. The ratio between LOCUST and FPP distribution functions is shown in panel *(c)* of figure 15. An increase in particle density is calculated for the high energy region, however these occur at particle densities more than 4 orders of magnitude lower than the $f_{\mathrm{p,rf}}(E, p)$ maximum value. LOCUST $f_{\mathrm{p,rf}}$ is plotted in the velocity space in panel *(d)*, in which the trapped particle cone is shown with the dashed lines. One can see that the tail protons are within the trapped region, albeit close to the trapped-passing boundary, which results in high calculated losses for counter particles, most prominent in the vicinity of this boundary. $f_{\mathrm{p,rf}}$ for D discharge #105453 has the same shape as #101184, however the energetic proton tail is calculated to decay with energy faster, with the MeV-range proton density in D plasma approximately a factor of 3 lower compared to He. This effect, observed in both TRANSP and FOPLA [84] calculations, is the consequence of more favourable proton RF acceleration in He plasmas owing to the lower ion density and larger mass of bulk ions.

For comparison the FPP-LOCUST $f_{\mathrm{p,rf}}(E, p)$ for He discharge #101185 is plotted in figure 16. Due to off-axis RF resonance positioning, and therefore lower RF power density compared to #101184, the proton acceleration in the pulse was less effective, resulting in a significantly larger $|\partial f_{\mathrm{p,rf}}(E)/\partial E|$. While an energetic tail is still clearly formed, it decays by three orders of magnitude in the energy range spanning from thermalised ions to $\approx$ 6 MeV. At a lower magnetic field the trapped particle cone is expected to be wider in this discharge, seen by the increase of pitch angle at which the RF tails are formed to around $\pm$0.4. A similar effect of unconfined orbit losses on $f_{\mathrm{p,rf}}(E, p)$ for negative pitch particles around the trapped tail and trapped-passing boundary can be seen.

LOCUST additionally offers insight into the characteristics of protons lost during the tracking. Orbits of promptly lost protons for the two He discharges are shown in panel *(a)* of figure 17 – these are two representative orbits chosen from the ensemble of particles with highest loss probability. Both orbits are of highly energetic protons with large Larmor radii and widths, with transient trapped orbit tips aligned with the respective RF resonance layer. A large majority of the modelled losses, amounting to 25 % of the simulated particles, result in particles hitting the tokamak wall at the location of outboard Be limiters, distributed over an $\approx$ 0.5 m section below the midplane denoted with the cyan line, where the plotted orbits terminate. Since this area coincides with the positioning of the FILD diagnostics in JET, the protons impinging on this wall region were sampled into a normalized energy-pitch angle distribution, and are plotted in a FILD-like format in panels *(b)* and *(c)*. Comparing the computed loss distributions to FILD measurements in figure 5, we observe that the main features have been well reproduced. Importantly,

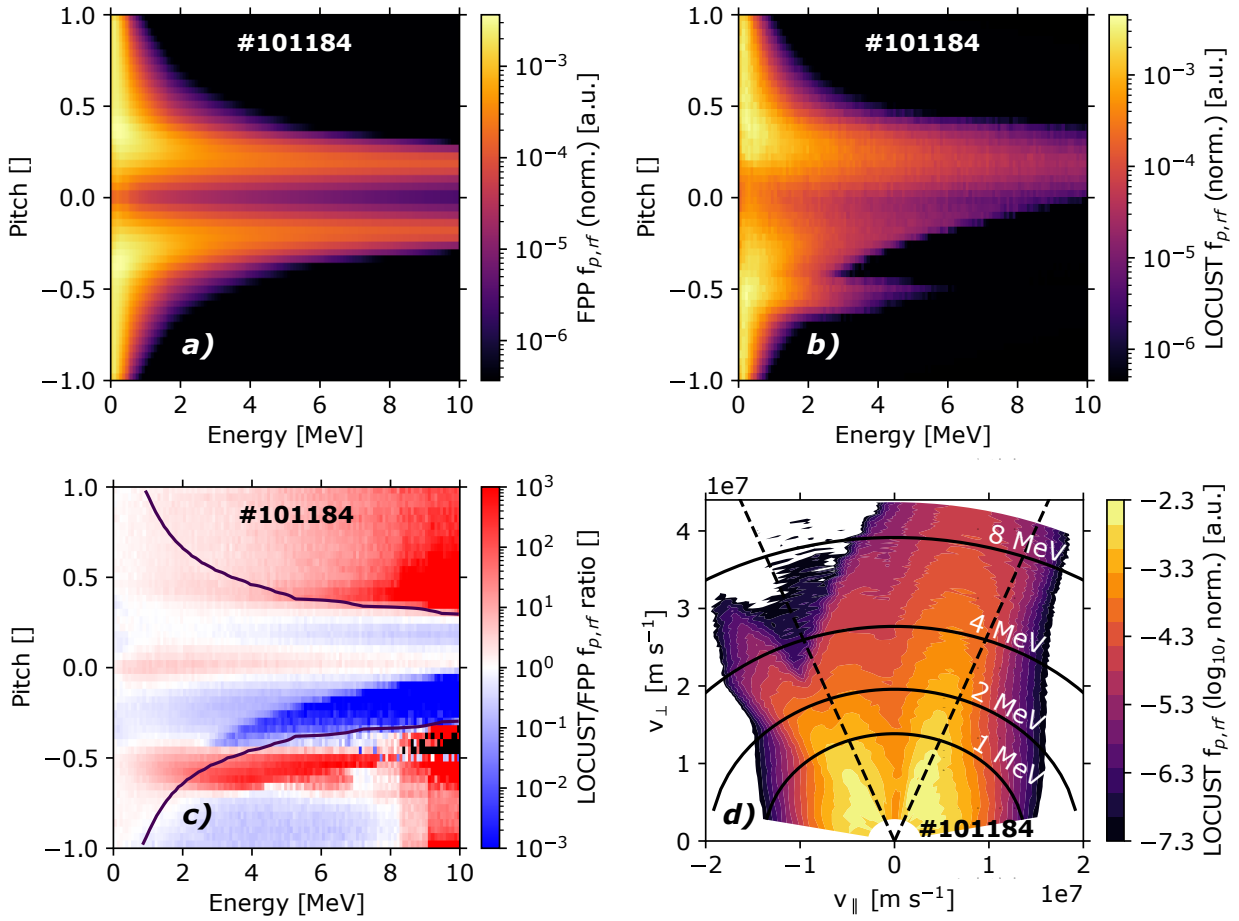

Figure 15: Modelled H RF minority distribution function $f_{\mathrm{p,rf}}$ for He discharge #101184. Panel *(a)*: normalized (integral value) pitch-energy proton $f_{\mathrm{p,rf}}$ calculated by FPP. Panel *(b)*: normalized (integral value) pitch-energy proton $f_{\mathrm{p,rf}}$ corrected for prompt losses and finite Larmor radii by LOCUST. Panel *(c)*: ratio of LOCUST-corrected and FPP proton $f_{\mathrm{p,rf}}$, with the black line denoting FPP's tail shape contour. Panel *(d)*: normalized (integral value, $\log_{10}$) velocity-space proton $f_{\mathrm{p,rf}}$, with iso-energy surfaces denoted with solid black lines, and the trapped particle cone denoted with dashed black lines. The distribution functions are plotted at $\rho_{\mathrm{tor}} = 0.18$ where protons have the largest mean energy in the plasma.

the pitch angle at which most losses occur is matched, as well as the distribution of losses around the position of the RF resonance layer, which is slightly wider in pitch for #101184 spanning angles of $40^o \approx 70^o$. This confirms that poorly confined orbits of particles at the trapped-passing boundary were the major contributor to the observed losses. In addition, the peak energy of the enhanced ridge of losses at pitch angle of $\approx 55^o$ matches that observed by FILD, at approximately 0.8 MeV in #101184 and 2 MeV in #101185. While the intensity of losses measured by FILD is an order of magnitude higher in #101185, the computed loss yields in LOCUST are similar for both discharges. Additionally, the LOCUST estimate of power flux on the wall region close to the location of the observed hotspot in #101185 due to prompt losses is not high enough to induce Be melting. Critical temperatures are also not reached by including 3D wall shaping in LOCUST, instead of using an axisymmetric model, although calculated local heat loads increase by an order of magnitude. These observations imply that there is a significant enhancement of losses due to MHD activity, discussed in section 2.2.3, which is not captured by our modelling. However, we conclude that the observed MHD modes acted mainly toward additional orbit destabilization of already

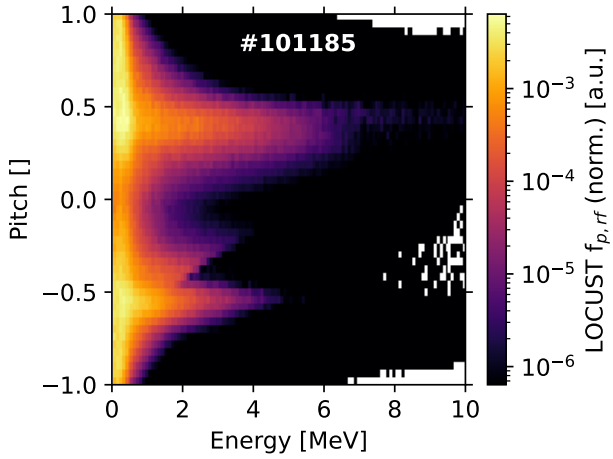

Figure 16: Modelled normalized (integral value) pitch-energy H RF minority distribution function $f_{\mathrm{p,rf}}$ for He discharge #101185, calculated by FPP and corrected for prompt losses and finite Larmor radii by LOCUST. The distribution function is plotted at $\rho_{\mathrm{tor}} = 0.18$ where protons have the largest mean energy in the plasma.

poorly confined energetic protons around the trapped-passing boundary, exacerbated in #101185 by the off-axis RF resonance. Triggering these effects were edge TAEs, impacting barely confined energetic protons with wide orbits, and core fishbones, perturbing orbits upon RF acceleration in the vicinity of the magnetic axis.

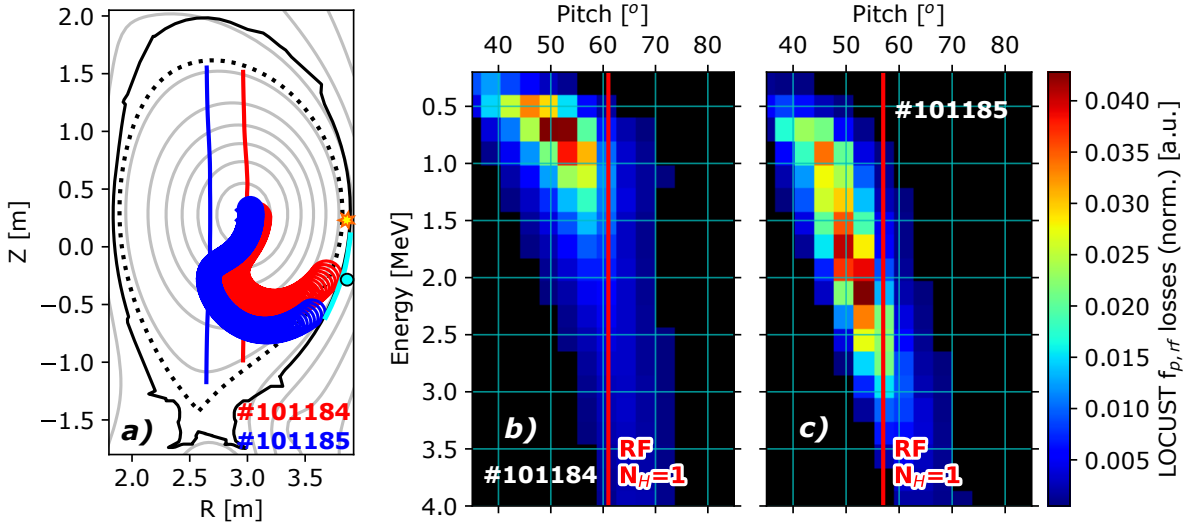

Figure 17: LOCUST calculated fast proton losses for He discharges #101184 and #101185. Panel *(a)*: examples of unconfined proton orbits with highest loss probabilities. The fast ion loss detector position is denoted with a cyan circle, together with a wall region onto which the computed lost orbits had to impinge to contribute to the estimate of FILD-like losses. The location of #101185 hotspot is denoted with the orange star. Panels *(b, c)*: computed normalized (integral value) FILD-like pitch angle (in degrees) vs. energy proton loss distributions sampled over the cyan wall region. The layout matches that of FILD measurements in figure 5, including the fundamental H RF resonance layer denoted with the red line.

3.2. Fusion product modelling

FPP-LOCUST proton distribution functions were fed into the DRESS code to calculate birth (R_{maj}, Z, E, p) distributions for products of primary proton-beryllium reactions, namely neutrons from ^{9}Be(p,n)^{9}B, deuterons and alphas from ^{9}Be(p,d)2α, and alphas from ^{9}Be(p,α)^{6}Li. Deuterons and alphas further trigger secondary fusion on beryllium, therefore their slowing-down distributions were calculated with LOCUST. This was done by weight sampling on the order of $\approx 10^{7}$ particles from DRESS birth functions and performing orbit-tracking until thermalisation at $1.5{\cdot}T_{\mathrm{i}}$, with background plasma parameters from TRANSP. The final state in the ^{9}Be(p,d)2α reaction was treated in DRESS as a pure three-body break-up, i.e. the final state interactions between the deuteron and the alpha particles were not modelled. Such interactions could in principle modify the shape of the birth spectra, however the impact on the energy distributions of the products after slowing-down is expected to be insignificant. Note that other fusion products, i.e. ^{9}B, ^{6}Li, ^{10}B, ^{12}C, and the effects of seconds harmonic RF acceleration of deuteron and alpha fusion products were not modelled, due to a negligible effect on the total neutron and gamma emission. In the final step of the modelling process the thermalised deuteron and alpha distributions were looped back into DRESS to obtain the birth distributions of secondary neutrons emitted in ^{9}Be(d,n)^{10}B and ^{9}Be(α,n)^{12}C fusion, and to assess the contribution of D-D and D-T fusion between deuteron fusion products and residual D and T. In D discharge #105453 proton knock-on driven acceleration of bulk deuterons is additionally assessed, together with its contribution to total neutron emission via D-D and D-T fusion.

3.2.1. Primary proton-beryllium products

In figures 18 and 19 the modelled emissivity profiles and energy spectra of neutrons emitted via the primary ^{9}Be(p,n)^{9}B fusion are shown. A common trait of the discharges' spatial emission distribution is their hollowness, with most neutrons being emitted in an $\approx$ 15 cm wide ring around the magnetic axis which peaks at the outboard midplane. This occurs because the most energetic protons with highest Be fusion cross section are trapped on the outboard side, additionally inducing a broadening of the emissivity profiles toward the low-field separatrix. As seen in panel *(b)* of figure 18, another peak is observed on the inboard side of the emissivity ring in discharge #101185, which coincides with the off-axis RF resonance layer positioning and is thus a result of the local source of energy to protons.

Pitch-integrated neutron energy spectra at the point of highest neutron emissivity are plotted in panel *(a)* of figure 19. The spectra exhibit several important features: because ^{9}Be(p,n)^{9}B is a threshold reaction, the neutron birth spectrum starts at 0 MeV and rises steeply to reach its first peak at neutron energy of 0.5 MeV, corresponding to the cross section's threshold at $E_{\mathrm{p,rf}} \approx 2.1$ MeV and first resonance at $E_{\mathrm{p,rf}} \approx 2.6$ MeV, respectively. The spectrum for #101184 additionally displays a broad peak at neutron energy of 1.9 MeV, driven by highly energetic protons interacting with beryllium at the second cross section resonance around $E_{\mathrm{p,rf}} \approx 4.8$ MeV. All three spectra are broad and have a prominent high-energy tail extending up to neutron energies of 7 MeV, an indication of a significant MeV-range proton population with relatively low $|\partial f_{\mathrm{p,rf}}(E)/\partial E|$. The spectral full widths at half maximum are large and vary between 2 MeV $\approx$ 3 MeV. Neutron spectra in discharges #101185 and #105453 are less prominent at high energies due to the less energetic proton population compared to #101184. In panel *(b)* volume-averaged neutron spectra for discharge #101184 at three pitch angles θ are shown, namely in the direction of the magnetic field (0^{o}), opposite (180^{o}), and perpendicular to it (90^{o}). A spectral difference is observed for the three directions due to the Doppler effect, that is an up-shift in energies of neutrons emitted in the direction of the magnetic field and a decrease for neutrons emerging from fusion reactions in the opposite direction of the ion movement. This is seen prominently for both resonant peaks. Another neutron peak emerges for the parallel spectral components at $\approx$ 1 MeV, which is a combined effect of a non-resonant rise in σ_{pBe} at $E_{\mathrm{p,rf}} \approx 3.0$ MeV and an energy-localized flattening of the anisotropic $f_{\mathrm{p,rf}}(E)$. The shape of spectra emitted at 90^{o} compared to

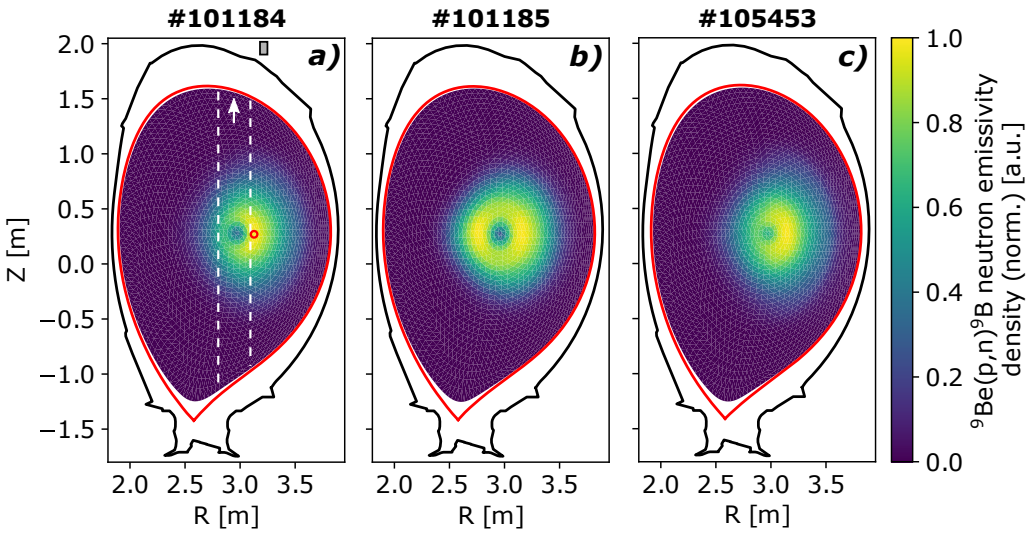

Figure 18: DRESS calculated normalized (maximum) ^{9}Be(p,n)^{9}B neutron emissivity densities for discharges #101184 in panel *(a)*, #101185 in panel *(b)*, and #105453 in panel *(c)*. Enclosing the profiles are the plasma boundary (red) and JET limiter (black). The core location at $\rho_{\mathrm{tor}} = 0.18$ for which the distributions in figures 19 and 20 are plotted is denoted with a red circle. TOFOR's line of sight is denoted with dashed white lines and arrow, and the position of the activation system with a gray rectangle.

the magnetic field is governed by the fact that spectral components at individual energies are all double-humped, i.e. split into a down- or up-shifted peak due to fast protons moving either towards or away from the perpendicular observer while gyro-orbiting around the magnetic field lines. Because primary proton-beryllium neutrons can only be produced in reactions with ≥ 2 MeV of kinetic energy, at large reactant orbit radii, a relatively large spectral split is induced at all energies of the perpendicular component. At neutron energies just above 0 MeV the split is approximately 0.1 MeV, and reaching $\pm$ 1.2 MeV for neutrons nominally emitted at 2 MeV. This effect alters the three distinct local peaks seen in the parallel spectrum components: only the up-shifted part of the first neutron peak at $E_{\mathrm{n}} \approx 0.5$ MeV can be seen, while the down-shifted component can not be distinguished from the non-resonant emission at lower E_{n}. The middle peak is surrounded by emission at comparable probability with similar energy splits and therefore gets averaged out. The third peak has a distinct down-shifted spectral component, visible due to its high resonant cross section compared to the plateau neutron emission at energies of around 1.5 MeV, while the up-shifted component at $\approx$ 2.7 MeV is less prominent and almost completely merged with the high-energy spectrum tail.

In figure 20 we display the modelled core deuteron and alpha fusion products of primary ^{9}Be(p,d)2α and ^{9}Be(p,$\alpha\gamma$)^{6}Li fusion for discharge #101184. Note that alpha contributions from the two reactions are summed up. In panel *(a)* the birth rate (DRESS, solid) and slowed-down density profiles (LOCUST, dashed) are compared. Similarly to ^{9}Be(p,n)^{9}B neutrons, the charged product birth profiles are hollow, however much broader and poloidally symmetric because the cross sections do not have a threshold and are non-negligible for protons with energies as low as several 10 keV. Core concentrations of fusion products with respect to n_{e} are approximately $3{\cdot}10^{-4}$ %. In panel *(b)* birth energy spectra (DRESS, solid) and slowed-down energy distributions $f_{\mathrm{fp,f}}$ (LOCUST, dashed) are shown. Low-energy peaks in deuteron and alpha birth spectra correspond to the three-body ^{9}Be(p,d)2α reaction, with mean energies of 0.57 MeV and 0.45 MeV, respectively. LOCUST shows that of the total number of particles simulated, approximately 9 % of deuterons and 2 % of alphas were lost. The higher energy alpha peak at mean energy of 1.8 MeV, is driven

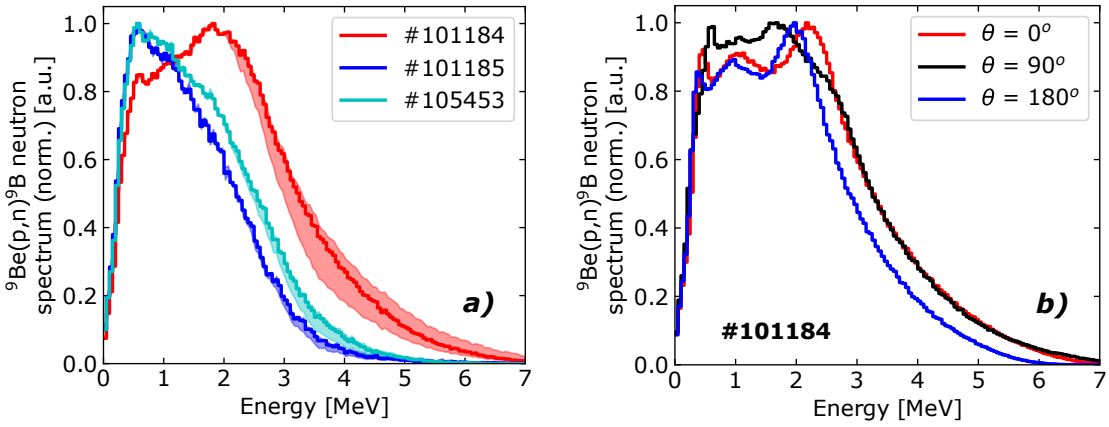

Figure 19: DRESS calculations of neutron energy spectra for reaction ^{9}Be(p,n)^{9}B. Panel *(a)*: comparison of pitch-integrated normalized (maximum) spectra for discharges #101184, #101185, and #105453 at $\rho_{tor} = 0.18$. 1σ uncertainty due to unavailability of the cross section beyond $E_p > 5.42$ MeV is shown. Panel *(b)*: comparison of volume-averaged normalized (maximum) spectra at three toroidal emission angles θ in discharge #101184.

by ^{9}Be(p,α)^{6}Li, with a 14 % loss rate computed by LOCUST. Thermalised deuteron $f_{fp,f}$ shows a larger negative energy gradient compared to the summed-up ^{4}He population, with the distribution decaying after $\approx$ 4.5 MeV, while the alphas extend up to energies of 6 MeV. Because of the low sensitivity of the two reactions' cross section to high energy protons, and thermalisation blending the differences in the fusion product distribution functions, $f_{fp,f}$ are similar for discharges #101185 and #105453.

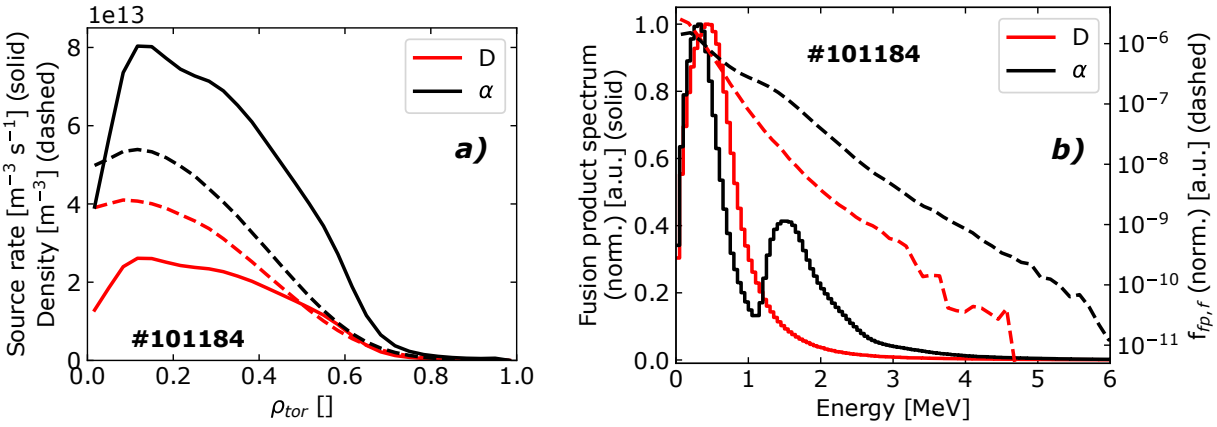

Figure 20: DRESS-LOCUST modelling of deuteron (red) and alpha (black) fusion products for reactions ^{9}Be(p,d)2α and ^{9}Be(p,α)^{6}Li for discharge #101184. Alphas from both reactions have been summed up. Panel *(a)*: birth profiles (solid) and slowed-down density profiles (dashed). Panel *(b)*: Normalized (maximum) birth energy spectra (solid) and normalized (integral) fusion product energy distribution functions (dashed). All quantities are plotted for an outboard core point at $\rho_{tor} = 0.18$

Calculated total (volume-integrated) fusion rates and fusion power for three primary proton-beryllium reactions are detailed in table 1. The highest neutron rate was calculated for He discharge #101184, while R_n is approximately a factor of 2 lower in the other two discharges. In #101185 a less evolved energetic proton tail results in a lower ^{9}Be(p,n)^{9}B reactivity, however this was partly recovered by a broader core emissivity profile and an increase in Be concentration by more than a factor of 2 due to limiter melting. Similarly R_n in #105453 is lower due to less favourable conditions for acceleration of an H RF minority in

D plasmas, and lower RF power. Both non-neutron emitting fusion reactions are seen to have total rates approximately and order of magnitude higher than ^{9}Be(p,n)^{9}B for all three discharges, due to their higher cross sections at lower proton energies.

Table 1: Computed volume-integrated reaction rates of primary fusion between fast RF protons and Be impurities, and total fusion power for discharges #101184, #101185, and #105453.

Discharge → Reaction ↓	#101184	#101185	#105453
^{9}Be(p,n)^{9}B [s^{-1}] (R_{n})	$6.6{\cdot}10^{13}$	$4.1{\cdot}10^{13}$	$3.2{\cdot}10^{13}$
^{9}Be(p,d)2α [s^{-1}]	$5.8{\cdot}10^{14}$	$9.0{\cdot}10^{14}$	$4.3{\cdot}10^{14}$
^{9}Be(p,α)^{6}Li [s^{-1}]	$5.9{\cdot}10^{14}$	$8.8{\cdot}10^{14}$	$4.4{\cdot}10^{14}$
P_{fus} [kW]	0.28	0.40	0.24

3.2.2. Secondary proton-beryllium products and residual fuel

The slowed-down deuteron and alpha distributions were used to calculated neutron emission via secondary fusion on beryllium impurities. The resulting emissivity profiles and neutron spectra are shown in figure 21. The $\mathrm{d}^{*}_{\mathrm{pbe}}$–Be neutron spectrum is strongly peaked with a mean energy of 4.7 MeV, while the $\alpha^{*}_{\mathrm{pbe}}$–Be spectrum is seen to be wide, due to a broad summed alpha energy distribution, extending over approximately 3 MeV, with a mean energy of 6.8 MeV. As detailed in table 2, all neutron rates for secondary fusion on beryllium are found to be orders of magnitude smaller than the primary emission, insignificantly contributing to the total neutron yield. Parasitic reactions on thermal deuterium and tritium fuel are found to be important only for D bulk discharge #105453, contributing approximately 13 % to the total neutron rates.

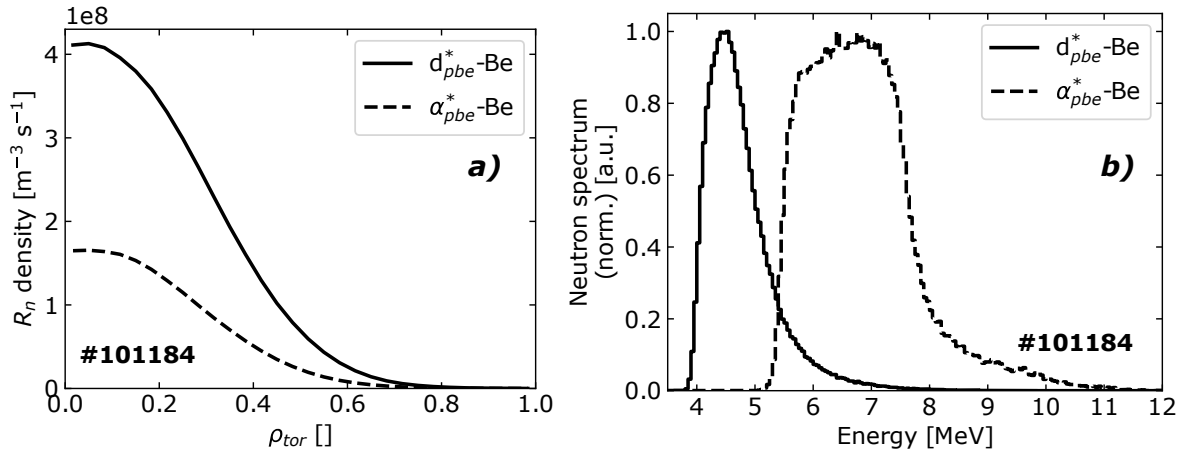

Figure 21: DRESS calculations of neutron rate density profiles in panel *(a)* and normalized (maximum) neutron energy spectra in panel *(b)* for reactions ^{9}Be($\mathrm{d}^{*}_{\mathrm{pbe}}$,n$\gamma$)^{10}B (solid) and ^{9}Be($\alpha^{*}_{\mathrm{pbe}}$,n$\gamma$)^{12}C (dashed) in discharge #101184. Neutron spectra are plotted at the position of the magnetic axis.

3.2.3. Deuteron knock-on tail in #105453

The non-negligible signature of fast deuterons detected in D discharge #105453 by NPA, as shown in figure 4, indicates that proton-beryllium fusion does not fully account for the total fusion yield observed

Table 2: Computed volume-integrated reaction rates of secondary fusion between fusion products, Be impurities, and residual thermal D and T for discharges #101184, #101185, and #105453. Fusion product deuterons are denoted d^*_{pbe}, fusion product alphas α^*_{pbe}, residual deuterons d_{th}, and residual tritons t_{th}.

Discharge → Reaction ↓	#101184	#101185	#105453
$^9Be(d^*_{pbe},n)^{10}B$ [s^{-1}]	$4.9{\cdot}10^9$	$6.9{\cdot}10^9$	$2.7{\cdot}10^9$
$^9Be(\alpha^*_{pbe},n)^{12}C$ [s^{-1}]	$1.8{\cdot}10^9$	$3.0{\cdot}10^9$	$9.6{\cdot}10^8$
$d^*_{pbe} \rightarrow d_{th}$ [s^{-1}]	$1.1{\cdot}10^9$	$2.0{\cdot}10^9$	$1.1{\cdot}10^{11}$
$d^*_{pbe} \rightarrow t_{th}$ [s^{-1}]	$7.6{\cdot}10^8$	$1.6{\cdot}10^9$	$6.7{\cdot}10^{10}$
$d^*_{pbe} \rightarrow d^*_{pbe}$ [s^{-1}]	$5.3{\cdot}10^5$	$1.2{\cdot}10^6$	$2.2{\cdot}10^5$
$d_{th} \rightarrow d_{th}$ [s^{-1}]	$3.5{\cdot}10^8$	$6.0{\cdot}10^8$	$1.5{\cdot}10^{12}$
$d_{th} \rightarrow t_{th}$ [s^{-1}]	$1.5{\cdot}10^9$	$2.6{\cdot}10^9$	$4.7{\cdot}10^{12}$
$t_{th} \rightarrow t_{th}$ [s^{-1}]	$1.0{\cdot}10^5$	$1.8{\cdot}10^5$	$2.6{\cdot}10^8$
$\sum R_n$ [s^{-1}]	$1.0{\cdot}10^{10}$	$1.7{\cdot}10^{10}$	$6.3{\cdot}10^{12}$

in this pulse. Therefore, the contribution of neutron emission triggered by the fast D tail via its interaction with bulk deuterons and residual tritium is assessed. The mechanism for generating the observed fast tail is inferred as follows – second harmonic RF D heating alone could not have produced the observed energetic deuterons due to the scheme's inefficiency at thermal ion energies, albeit the resonance location at $v_{\|}$=0 coincided with the magnetic axis. We postulate that elastic scattering of MeV-range protons on thermal deuterons d(p,p)d, i.e. knock-on effect [85], triggered the initial deviation of bulk deuterons from a Maxwellian distribution, which were further accelerated by 2nd harmonic RF heating, to energy ranges between several hundred keV to MeV. The capability to model the combined effect of knock-on and RF heating of a Maxwellian ion population at JET is not readily available and is outside the scope of this paper to develop, therefore a semi-empirical approach to estimating the distribution function of the fast deuteron tail in #105453 is adopted.

The initial estimate of the deuteron energy distribution shape and amplitude is based on NPA measurements. As shown in figure 22 the D neutral tail measurement is fitted with a sum of two Maxwellian functions with effective temperatures T_{eff} of 30 keV and 120 keV. The fit is done up to particle energies of 1 MeV, where the extrapolated amplitude of $f_{d,f}$ is more than eight orders of magnitude lower than the bulk Maxwellian, beyond which deuterons are not expected to meaningfully contribute to the total fusion yield. The integral density of the fast deuteron component can be evaluated through the ratio of D and H NPA signal strengths in the interval of ion energies [126.0, 370.0] keV, with the hydrogen density constrained by the residual gas analysis in JET's sub-divertor plenum. A combined total distribution function for plasma deuterons is constructed, composed of the thermal and fast components, with its integral value corresponding to the computed deuterium density, described in Section 3.1.1.

Because NPA measurements are representative of line-integrated energy spectra of emitted neutrals, synthetic diagnostics methods are generally required for inferring properties of the original ion distribution. Demonstrations of NPA spectrum unfolding have been performed for JET [86], however the technique requires forward modelling capabilities of the combined knock-on and RF acceleration. We have therefore developed an alternative, simplified NPA-based model for resolving $f_{d,f}$, constrained by the following assumptions:

(i) Due to the low density of the plasma, fast ions neutralised in the core are expected to have a rel-

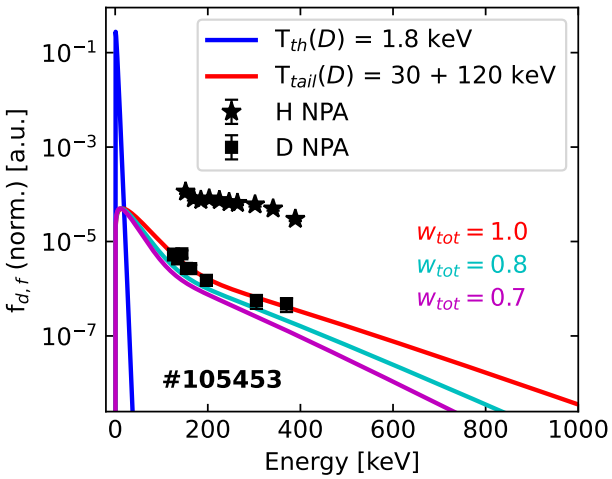

Figure 22: Normalized ($\int f_{\mathrm{d,f}} = 1$) deuteron energy distribution function comprising bulk (blue) and fast tail components (red) for discharge #105453. The energetic ion distribution shape is fitted against NPA D measurements (squares) with a composite Maxwellian function, while the ratio between thermal and fast components is determined by comparing H (stars) and D NPA signal strengths. $f_{\mathrm{d,f}}$ is shown for three values of the combined knock-on and 2nd harmonic RF acceleration probability w_{tot}, corresponding to core points denoted in panel *(c)* of figure 23.

atively large plasma mean free path and thus a high probability of reaching the NPA. Additionally contributing to the NPA signal are core-born fast ions neutralised at the plasma edge due to their wide trapped particle trajectories. The NPA data fit is therefore assumed to represent a constant-in-pitch energy distribution function $f_{\mathrm{d,f}}$ of fast deuterons largely originating from the plasma core. In order to resolve $f_{\mathrm{d,f}}$ spatially in (R, Z), the probabilities of generating fast deuterons via proton elastic scattering (w_{ko}) and 2$^{\mathrm{nd}}$ harmonic RF heating (w_{rf}) in steady-state conditions are assessed individually for each process. These 2D probability functions are multiplied and combined into w_{tot}, shown in panel *(c)* of figure 23. Normalized values of w_{tot} are used to scale the Maxwellian temperatures T_{eff} of the NPA-fitted fast tail, converging toward a thermal Maxwellian distribution of the bulk deuterons as probability for combined acceleration approaches zero. In figure 22 $f_{\mathrm{d,f}}$ energy distributions are shown for three values of w_{tot}, namely the non-scaled original fit at $w_{\mathrm{tot}} = 1.0$ representing the core location with the highest probability of deuteron acceleration, and two scaled distributions with $w_{\mathrm{tot}} = 0.8$ and 0.7, both at $\rho_{\mathrm{tor}} = 0.18$ as per the markers in panel *(c)* of figure 23, exhibiting the poloidal dependency of the acceleration effect.

(ii) The first weight function w_{ko} is based on proton-deuteron elastic scattering reaction rates:

$$w_{\mathrm{ko}}(\mathbf{v}_{\mathrm{p}}, \mathbf{v}_{\mathrm{d}}, R) = n_{\mathrm{p}}\, n_{\mathrm{d}} \int_{\mathbf{v}_{\mathrm{p}}} \int_{\mathbf{v}_{\mathrm{d}}} f_{\mathrm{p,f}}\; f_{\mathrm{d,th}}\; \mathbf{v}_{\mathrm{rel}}\; \sigma_{ko}(\mathbf{v}_{\mathrm{rel}})\; d\mathbf{v}_{\mathrm{p}} d\mathbf{v}_{\mathrm{d}}\;, \tag{1}$$

in which the knock-on reactivity is computed using the TRANSP-LOCUST modelled fast proton distribution function $f_{\mathrm{p,f}}$, an originally Maxwellian D distribution $f_{\mathrm{d,th}}$, and evaluated D(p,p)D elastic scattering cross section σ_{ko} [87]. The knock-on reaction rate profile is shown in panel *(a)* of figure 23.

(iii) The second weight function w_{rf} reflects the interaction of the N=2 RF wave field with the fast deuteron tail. The RF interaction is modelled by constructing a radial wave absorption function, which is a

superposition of Gaussian functions in the major radius R space, summed over $f_{\mathrm{d,f}}$ deuteron energy range. Note that particle energy dependency is expressed through the parallel $v_{\parallel}$ and perpendicular $v_{\perp}$ velocity terms in the wave interaction formulation. The peak position of the Gaussians is determined by the Doppler shift $\Delta_{\mathrm{d,f}}$ of fast ions, and the full width at half maximum corresponds to the energetic particles' Larmor radii ρ_{L}:

$$w_{\mathrm{rf}}(E_{\mathrm{d}}, R) = n_{\mathrm{d,f}}^{\mathrm{norm}}\, D_{\mathrm{rf}}^{\mathrm{norm}} \sum_{E_{\mathrm{d}}} \exp\left(-\frac{1}{2}\frac{(R-\Delta_{\mathrm{d,f}})^2}{\left(\rho_{\mathrm{L}}/\sqrt{2\ln 2}\right)^2}\right), \text{ where} \tag{2}$$

$$\Delta_{\mathrm{d,f}} = \mathrm{N}\frac{|q|}{m}\frac{R_0\, B_0}{(\omega_{\mathrm{rf}} - k_{\parallel} v_{\parallel})}, \text{ and} \tag{3}$$

$$D_{\mathrm{rf}} = \left(J_1\left(\frac{k_{\perp} v_{\perp}}{\omega_{\mathrm{rf}}}\right) + \frac{E_-}{E_+} J_3\left(\frac{k_{\perp} v_{\perp}}{\omega_{\mathrm{rf}}}\right)\right)^2 . \tag{4}$$

The Gaussian amplitudes in Equation (2) are determined by $n_{\mathrm{d,f}}^{\mathrm{norm}}$, which is the normalized (maximum) $f_{\mathrm{d,f}}$ density of deuterons at a given energy, and $D_{\mathrm{rf}}^{\mathrm{norm}}$, representing the normalized (maximum) RF diffusion coefficient for a harmonic N=2 interaction, proportional to the energy-dependent intensity of the wave-particle coupling. Terms in Equations (2 – 4) are R_0 and B_0, the major radius and magnetic field at the magnetic axis, respectively, the injected RF frequency ω_{rf}, the parallel and perpendicular wave number with respect to the magnetic field $k_{\parallel}$ and $k_{\perp}$, the co- and counter-rotating polarized electric field with respect to the ions' gyro-motion E_+ and E_-, and first kind Bessel functions J_{n}. The computed Gaussian composite is constant along the tokamak vertical axis. The computed w_{rf} is shown in panel *(b)* of figure 23, where one can see that there are two radial maxima of RF interaction, displaced symmetrically by $\approx$ 20 cm with respect to the magnetic axis, owing to the RF antenna's dipole phasing.

The modelled $f_{\mathrm{d,f}}$ distribution functions were input into DRESS to compute the fusion reactions rates and neutron emissivity profiles of reactions triggered by deuterons accelerated by a combined knock-on and 2$^{\mathrm{nd}}$ harmonic RF effect. The calculated neutron rates emitted by individual fusion reaction driven by knock-on deuterons $\mathrm{d_{ko}}$ are detailed in Table 3. The combined fast deuterons' contribution to the neutron yield is $1.0{\cdot}10^{13}$ s^{-1}, which is comparable to the total proton-beryllium neutron emission at $\approx 3{\cdot}10^{13}$ s^{-1}. The knock-on contribution to total R_{n} is a significant 20 %, with neutrons emitted in the interaction between knock-on deuterons and thermal tritium being the second largest contribution to the total yield.

Table 3: Computed volume-integrated neutron rates via fusion reactions driven by fast knock-on deuterons in D discharge #105453. Knock-on deuterons are denoted $\mathrm{d_{ko}}$, fusion product deuterons $\mathrm{d^*_{pbe}}$, residual deuterons $\mathrm{d_{th}}$, and residual tritons $\mathrm{t_{th}}$.

Discharge → Reaction ↓	#105453
^{9}Be($\mathrm{d_{ko}}$,n)^{10}B [s^{-1}]	$1.0{\cdot}10^{10}$
$\mathrm{d_{ko}} \rightarrow \mathrm{d^*_{pbe}}$ [s^{-1}]	$9.7{\cdot}10^{7}$
$\mathrm{d_{ko}} \rightarrow \mathrm{d_{th}}$ [s^{-1}]	$2.9{\cdot}10^{12}$
$\mathrm{d_{ko}} \rightarrow \mathrm{t_{th}}$ [s^{-1}]	$7.5{\cdot}10^{12}$
$\mathrm{d_{ko}} \rightarrow \mathrm{d_{ko}}$ [s^{-1}]	$4.2{\cdot}10^{9}$
$\sum R_{\mathrm{n}}$ [s^{-1}]	$1.0{\cdot}10^{13}$

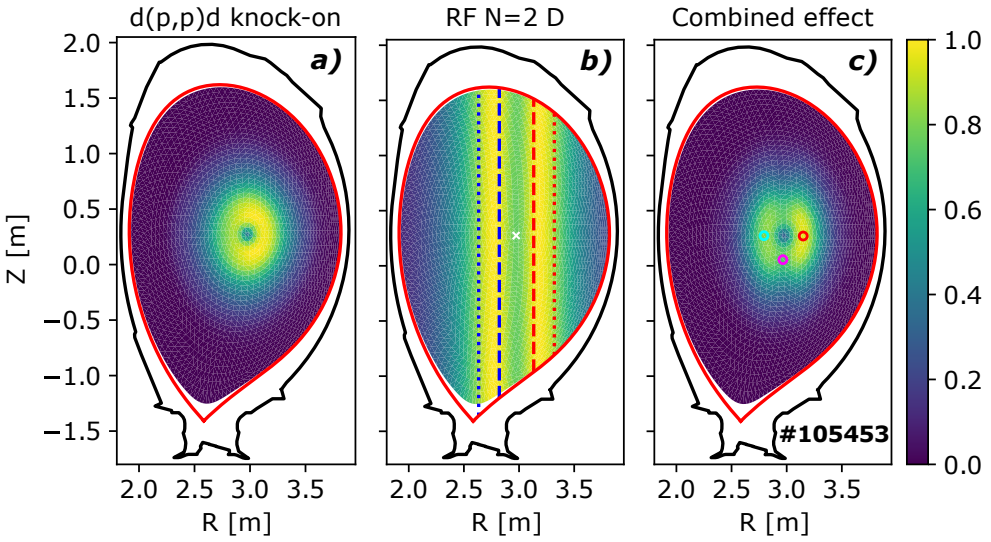

Figure 23: Computed normalized (maximum) probability functions used for linear scaling of the NPA-fitted deuteron fast ion tail $f_{\mathrm{d,f}}$ for discharge #105453. Panel *(a)*: proton-deuteron elastic scattering reaction rate weight function w_{ko} – equation (1). Panel *(b)*: weight function w_{rf} characterizing second harmonic D RF interaction with the fast ion tail $f_{\mathrm{d,f}}$ – equation (2). Radial planes of N=2 RF absorption for deuterons at energies of 30 keV (dashed) and 120 keV (dotted) for a positive (red) and negative (blue) Doppler shift are shown. Magnetic axis is denoted with a white ×. Panel *(c)*: combined interaction probability function $w_{\mathrm{tot}} = w_{\mathrm{ko}} \cdot w_{\mathrm{rf}}$, with denoted three positions at same $\rho_{\mathrm{tor}} = 0.18$ but varying $f_{\mathrm{d,f}}$ scaling, corresponding to energy distribution plots in figure 22.

A combined knock-on and 2$^{\mathrm{nd}}$ harmonic RF effect is expected to generate a fast alpha tail in the equivalent He low-density discharge #101184 as well. However, because alphas produce neutrons by fusing with impurities via $^{9}\mathrm{Be}(\alpha,\mathrm{n}\gamma)^{12}\mathrm{C}$, rather than the bulk plasma ions, the resulting reaction rates are expected to be orders of magnitude lower than dominant proton-beryllium fusion, comparable to neutron emission triggered by alpha fusion products.

3.3. Experimental validation

Having assessed the individual neutron yield components for the three discharges, the total yield is compared against the measurements of JET's absolutely calibrated fission chambers. A pivotal part of this is the evaluation of the computational uncertainty of the modelled proton-beryllium, D-T, and D-D neutron rates. Individual uncertainty contributors are discussed below, and summarized in table 4 – assuming the level of correlation between contributions is low, the total relative calculational uncertainty is assessed as the square root of the sum of squares of individual values, adding up to ≈ ±35 % for proton-beryllium, and ±22 for D-T and D-D fusion.

(a) *^{9}Be(p,n)^{9}B cross section*: an uncertainty estimate of the dominant proton-beryllium reaction cross section was provided as part of the re-evaluation effort [29]. Over an energy range of approximately 3 MeV the cross section 1σ uncertainty varies between 1 – 5 %. This was propagated through the calculation of the reaction's reactivity $\langle\sigma v\rangle$ for the whole plasma volume, to obtain an estimate of the relative computational uncertainty in R_{n} of ±3 %. Additionally, the cross section is evaluated only up to $E_{\mathrm{p,rf}} = 5.42$ MeV where it has a relatively high value of 0.42 barn, after which measurements are not available. In the presented DRESS calculations it was assumed that σ_{pBe} decreases linearly beyond its last available measurement, reaching 0 barn at 10 MeV. To assess the impact of the cross section availability cut-off, DRESS calculations were run with two different assumptions – namely

that the cross section is zero barn beyond 5.4 MeV, and that it remains constant at the last measured value. This variation is assumed to be a 3σ uncertainty assessment. The uncertainty in the calculated spectra shown in figure 19, and that of the integral ^{9}Be(p,n)^{9}B neutron rates represents the derived 1σ value. #101184 is most sensitive to this change due to the highest density of protons at energies beyond 5 MeV, which contributes ± 7 % to R_n uncertainty, while in #101184 and #105453 the effect is small at ± 2 %.

(b) Plasma composition: the uncertainty of R_n is dependent on the uncertainty of fast proton and thermal Be densities. The former is estimated via a residual gas analysis measurement ξ, which introduces an additional dependency on electron density and impurity dilution, whereas Be density profiles were measured directly via charge exchange recombination spectroscopy. This yields the following non-linear neutron rate proportionality to the uncertainty sources:

$$R_\mathrm{n} \propto n_\mathrm{p,f}\, n_\mathrm{Be} = \xi n_\mathrm{Be} \left(n_\mathrm{e} - n_\mathrm{Be} Z_\mathrm{eff} - \sum_\mathrm{imp} n_\mathrm{i} Z_\mathrm{i} \right) \ .$$

The uncertainty was assessed probabilistically by sampling from Gaussian distributions of n_e, n_Be, and ξ with prescribed 1σ standard deviations of 10 %, 18 %, and 2 %, respectively, based on experimental uncertainties. The relative computational uncertainty in R_n is evaluated to be ±31 %. The contribution of high-Z impurities to the total uncertainty is small and is neglected. In D discharge #105453 the uncertainty of tritium density affects the prominent D-T neutron rate component. The standard deviation of the tritium concentration measurement is ≈ 20 %, and is linearly proportional to the relative computational uncertainty of R_n.

(c) Safety factor: the q-profile in the core has an effect on fast proton orbits, their confinement, and consequently the neutron rate calculation via $f_\mathrm{p,f}$. The safety factor was reconstructed with EFIT++ using an inversion radius constraint derived from electron cyclotron emission T_e measurements – the reconstructed q-profiles consistently reached values of 1 closer to the magnetic axis than indicated by the ECE marker, most likely due to counter-balancing of additional magnetics and pressure equilibrium constraints. An outward shift of the q=1 position by ρ_tor = +0.1 was performed to assess the effect of a change in proton fast ion distribution function on proton-beryllium neutron rates. The relative computational uncertainty in R_n due to uncertainty in reconstructed q-profiles is evaluated to be +19 %.

(d) Deuteron knock-on $f_\mathrm{d,f}$: the uncertainty of knock-on energy distribution obtained via an NPA fit for discharge #105453 on the computed D-T and D-D neutron rates was estimated by varying the T_eff of the high-energy tail fit. A variation of ±25 keV resulted in a computational uncertainty of ≈ ±9 %.

In figure 24 the total measured and calculated neutron rates are plotted, together with an experimental uncertainty of ≈ 10 %, and computational uncertainty as per table 4. For both He discharges the primary neutron emitting proton-beryllium fusion is dominating, with secondary fusion on beryllium and residual D and T interactions contributing negligibly to the total neutron rates. In D discharge #105453 the primary proton-beryllium contribution is approximately three times higher than that of fusion between fast knock-on deuterons and a mix of bulk D and trace T. Measured and calculated neutron yields are seen to match within the combined experimental and computational uncertainty. Their relative discrepancies, detailed in table 5, are well within the combined experimental and computational uncertainty evaluations, and the systematic discrepancies observed for fusion performance modelling on large datasets of D-D and D-T plasmas which are predominantly driven by the fusion between fast and thermal bulk ions, which average at ≈ 40 % [15, 88].

Table 4: Summary of plasma parameter sensitivity study for discharges #101184, #101185, and #105453 to determine the total uncorrelated uncertainty of the computed neutron rate R_n for proton-beryllium, D-T, and D-D fusion. The individual reactions' contributions to the total uncertainty for #105453 were weighted by their relative R_n share.

Parameter variation	R_n variation [%] (reaction, discharge)
^{9}Be(p,n)^{9}B cross section ±1–5 %	±3 (p–^{9}Be, All)
^{9}Be(p,n)^{9}B cross section > 5.42 MeV	±7 (p–^{9}Be, #101184) ±2 (p–^{9}Be, #101185 & #105453)
Plasma composition n_e ±10 %, n_{Be} ±18 %, ξ ±2 %	±31 (p–^{9}Be, All)
Plasma composition n_T ±20 %	±20 (D-T, #105453)
q=1 shifted by ρ_{tor} +0.1	+19 (p–^{9}Be, All)
T_{eff} ($f_{d,f}$) ±25 keV	±9 (D-T + D-D, #105453)
Uncorrelated total uncertainty	**+37 / –32** (#101184) **+36 / –31** (#101185) **+33 / –29** (#105453)

Table 5: Comparison of measured and calculated total neutron rates R_n with the relative discrepancy of the calculation for discharges #101184, #101185, and #105453.

Discharge → R_n ↓	#101184	#101185	#105453
Measured [s^{-1}]	5.8·10^{13}	5.5·10^{13}	6.1·10^{13}
Calculated [s^{-1}]	6.6·10^{13}	4.1·10^{13}	4.9·10^{13}
Calc./Meas.–1 [%]	+14 %	–25 %	–20 %

In figure 25 volume-integrated neutron spectra components from individual fusion reactions are summed up to obtain total neutron energy spectra for the three modelled discharges. The spectral contributions are coloured based on the source reaction, while the line style denotes the source of particles interaction – namely a solid line indicates primary proton-beryllium or residual hydrogenic fuel fusion, a dashed line indicates reactions driven by proton-beryllium deuteron and alpha fusion products, and a dash-dotted line denotes fusion triggered by fast deuterons accelerated by the knock-on effect (only relevant for #105453). In panel *(a)* we see that the neutron spectrum in He discharges is dominated by a broad primary ^{9}Be(p,n)^{9}B component, up to energies of ≈ 8 MeV, after which the tail of ^{9}Be(α^*_{pbe},nγ)^{12}C neutrons is the most prominent. At around 12 MeV the D-T component becomes dominant, exhibiting a large high-energy tail extending to energies beyond 20 MeV. Neutrons emitted via ^{9}Be(d$^*_{pbe}$,nγ)^{10}B, D-D, and T-T reactions are indistinguishable from the high-energy tail of the p–Be neutrons. Panel *(b)* shows that due to #105453 being a D bulk plasma pulse, with a higher concentration of T and a population of fast knock-on deuterons,

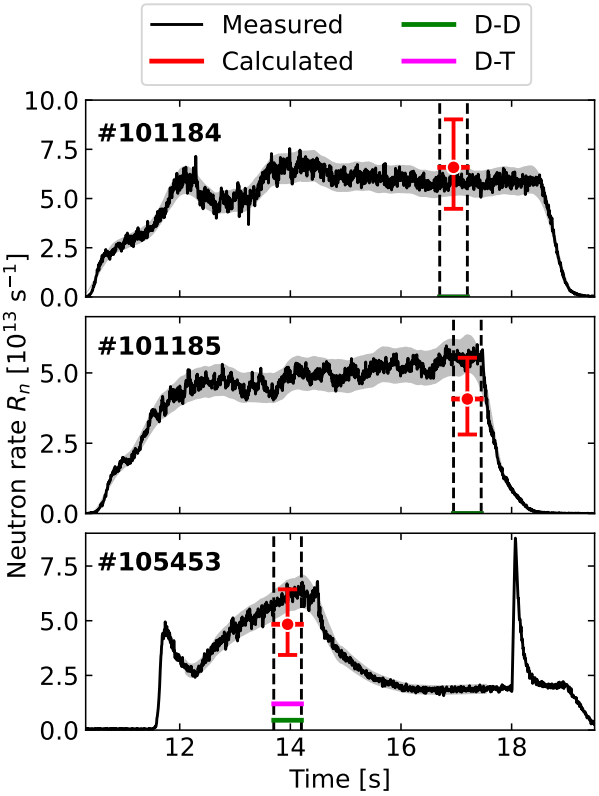

Figure 24: Comparison of measured and calculated total neutron rates R_n for discharges #101184, #101185, and #105453. The contribution of D-D and D-T fusion is added. The experimental uncertainty is denoted with the grey shaded area, and the computational uncertainty with the red error bars.

the neutron spectrum changes compared to He. The negative energy gradient of the proton-beryllium component is larger due to the lower fast proton energy density. The D-D component is large enough for its thermal peak and the broader d_{ko}–d_{th} spectral component to be dominant around $E_n \approx 2.45$ MeV. The D-T component is significant in #105453, with the fusion between knock-on deuterons and thermal tritons being the dominant component, inducing a broad spectral shape.

Due to relatively low neutron rates achieved in the modelled discharges, count rates recorded by the neutron radial profiles camera and the TOFOR neutron spectrometer were too low to yield statistically relevant results. Hence, the computed total neutron emissivity profiles and total neutron energy spectra can not be directly experimentally validated. We calculate synthetic TOFOR spectra using DRESS neutron emissivity results by integrating the neutron source spatially, over TOFOR's field of view (shown in panel *(a)* of figure 18), and with respect to the emission angle, only tallying neutrons emitted in the direction of the detector, perpendicularly to the magnetic field. The incident energy spectrum is further multiplied by TOFOR's response matrix, which contains information on how the time-of-flight spectrum depends on impinging neutron energy. Synthetic TOFOR responses are shown in figure 26. Neutrons emitted through primary proton-beryllium fusion are present in the spectral region above ≈ 37 ns, with the intensity dropping beyond 65 ns due to a decrease in TOFOR's sensitivity to low-energy neutrons. ^{9}Be(p,n)^{9}B emission differences driven by varying prominence of fast proton tails in the discharges are seen to be preserved. For pulse #105453 the D-D and D-T peaks are prominently featured in addition to the p–Be tail. Note that the modelled TOFOR spectra do not include the contribution of scattered neutrons – this is not expected to

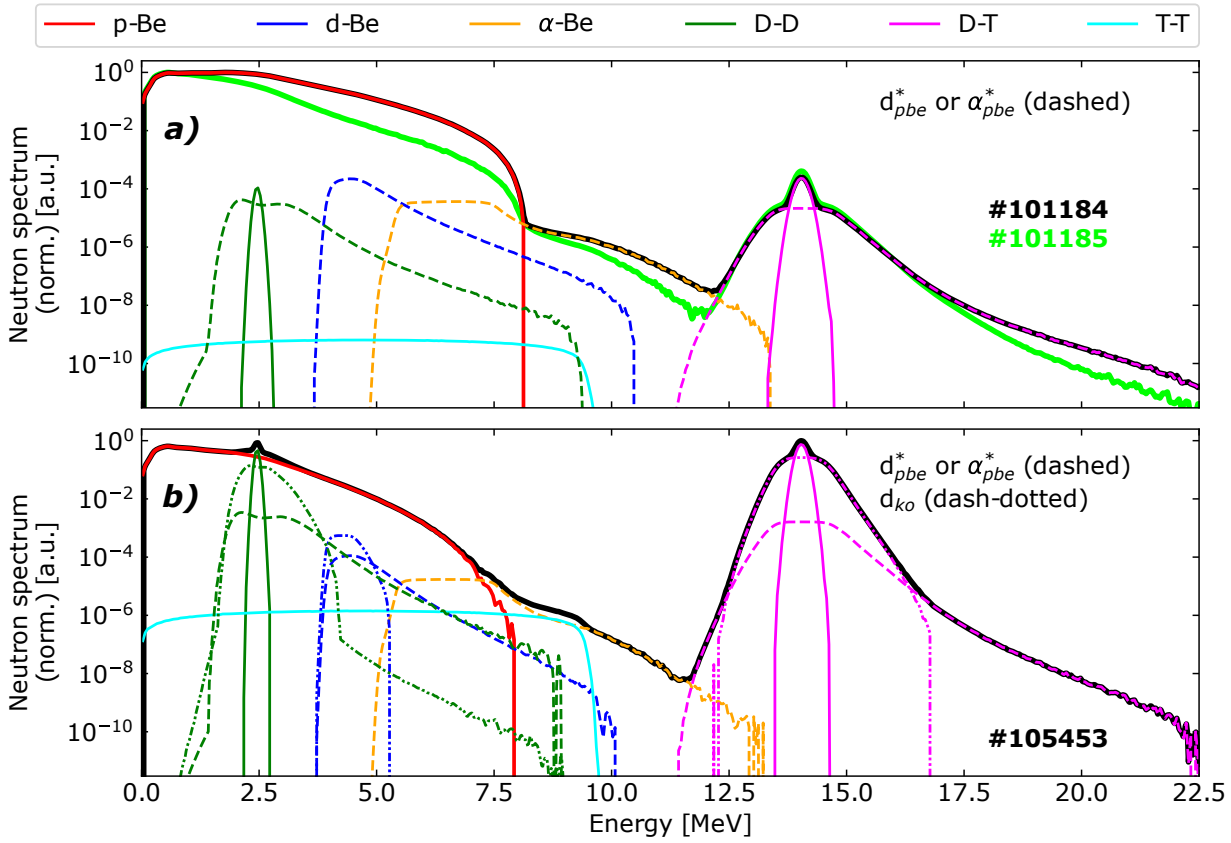

Figure 25: DRESS calculated normalized (maximum) total neutron energy spectra (solid black) with individual contributions – primary and secondary neutrons of the proton-beryllium chain, and D-D, D-T, and T-T neutrons due to residual fuel, for discharges #101184, and #101185 (only total spectrum shown in light green) in panel *(a)*, and #105453 in panel *(b)*. Neutron spectra driven by secondary deuterons d^*_{pbe} or alphas α^*_{pbe} are denoted with dashed lines, while knock-on deuteron d_{ko} induced spectra are denoted with dash-dotted lines.

significantly alter the shape of the calculated response.

4. Neutron source model

A neutron source model description was generated for the three discharges, summing up all individual emission components. The source provides the basis for random-sampling of plasma neutrons at birth, and contains information on neutrons' spatial, angular, and energy emission probability. To demonstrate the applicability of the model, neutron sources were coupled to MCNP via the standard source definition function (SDEF card) and neutron transport calculations were launched with nuclear data from the FENDL-3.2b library [30] using a detailed reference JET MCNP model [89], tracking 10^{10} particle histories. In addition to analog simulations, variance reduction using ADVANTG was was applied to improve tally statistics and demonstrate the sources' compatibility with the technique [90]. We analyse the response of fission chambers (FC) and the neutron activation system (AS). The former are cylindrical detectors, positioned next to the transformer limbs, the response of which was obtained by convolving the computed neutron flux with a measured ^{235}U fission chamber response function [1, 12]. The activation system, located in JET's octant 3 upper port (shown in panel *(a)* of figure 18), was modelled by computing the energy dependent

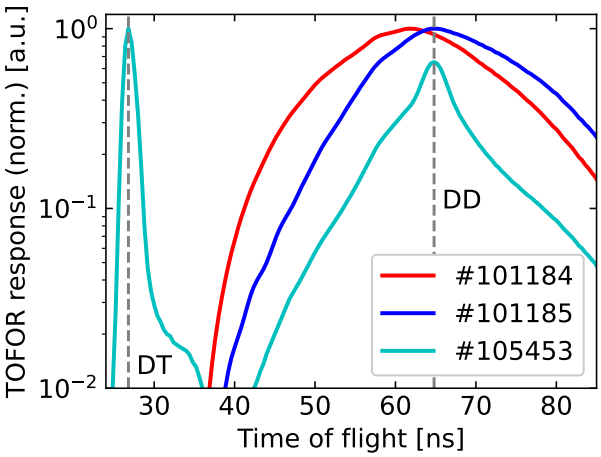

Figure 26: Normalized (maximum) synthetic TOFOR response calculated with realistic neutron spectra for discharges #101184, #101185, and #105453. Grey dashed lines denote D-D and D-T neutron emission peaks, corresponding to neutron time-of-flight values of ≈ 65 ns and 27 ns, respectively.

neutron flux within the volume of activation foil mock-ups located in the diagnostic's irradiation chamber. In order to assess the sensitivity of foil activation to varying realistic neutron sources, the computed flux was additionally multiplied by the activation cross section of reactions ^{115}In(n,n')^{115m}In, ^{27}Al(n,p)^{27}Mg, and ^{56}Fe(n,p)^{56}Mn from the IRDFF-II nuclear data library [91]. The reactions' cross sections render them sensitive to differences in neutron energy spectra in the range of ≈ 0.2 MeV to 8 MeV, relevant for proton-beryllium and D-D fusion, due to their increasing energy thresholds as seen in figure 27 [13]. All three activation reactions have a relatively flat response for neutrons emitted in the D-T energy range. The response of miniature fission chambers (mFC) to the various sources was studied as well. Due to their small size and response flexibility, these detectors can be positioned closer to the plasma source, and at numerous toroidal and poloidal locations, compared to the standard FC design. This can render the overall fusion yield measurement less sensitive to complex tokamak geometry effects and variations in plasma emissivity distributions, making mFCs highly relevant for deployment in fusion reactors. ^{235}U and ^{238}U mFCs were modelled at the location of the activation system, using detector composition data extensively validated for fission power measurements [92]. For comparison, all the detector responses were additionally calculated with generic MCNP D-D and D-T neutron sources, i.e. source terms that have been used as reference for most JET neutronics analyses and assume a thermal spectrum peak shape [6, 7, 12].

In figure 27 the successful coupling of realistic proton-beryllium neutron sources is demonstrated by plotting the MCNP computed neutron energy spectra at the position of JET's activation systems for the three discharges. One can observe a largely broadened neutron spectrum extending up to energies of around 8 MeV due to the dominant ^{9}Be(p,n)^{9}B fusion, with preserved spectral energy gradients which carry information on $\partial f_{\mathrm{p,rf}}(E)/\partial E$ of the underlying fast proton ion distribution function. Due to a non-negligible amount of neutron thermalisation occurring, albeit the irradiation end is located in the immediate vicinity of the separatrix, the broad p–Be source spectral peaking between 0.5 MeV to 2 MeV (figure 19) is not distinguishable from the slowing-down neutron background. The birth probability of the secondary $\mathrm{d}^{*}_{\mathrm{pbe}}$–Be and $\alpha^{*}_{\mathrm{pbe}}$–Be neutrons is too low for them to be tallied in MCNP with statistical meaningfulness, meaning it is highly unlikely their spectral contributions could have been detected by JET's neutron diagnostics suite. On the other hand, signatures of neutrons emitted in fusion of residual D and T are preserved – most notably, discharge #105453 has a visible D-D peak and a prominent D-T component with distinct peak

shaping as a result of competing thermal and deuteron knock-on neutron emission. Furthermore, due to the effects of D-T neutron slowing down, the D pulse's p–Be spectral tail at energies above 6 MeV is piled over. In He discharges the D-T component was on the limit of computational detectability. Comparing the AS spectrum computed for #101184 against generic D-D and D-T sources in figure 28, we observe the main difference in the relative intensity of the spectra in the range 0.1 MeV $\leq E_n \leq$ 5 MeV. This is because the proton-beryllium spectral peak is located at lower energies than D-D or D-T, and is significantly broader, increasing the relative abundance of neutrons in this energy interval. This also means that the thermal part of the neutron spectrum in p–Be discharges is systematically higher than in the generic sources by up to several 10 %. However, below energies of approximately 100 keV the spectral shapes become comparable due to prevalent thermalisation and nuclear interaction effects. #101184 spectrum computed at the location of one of JET's ex-vessel fission chambers shows that the spectral shape is generally preserved with the transport of neutrons to the outside of the tokamak vessel, with the exception of a general depletion of the MeV-range neutron population in favour of a higher probability of thermalised neutrons.

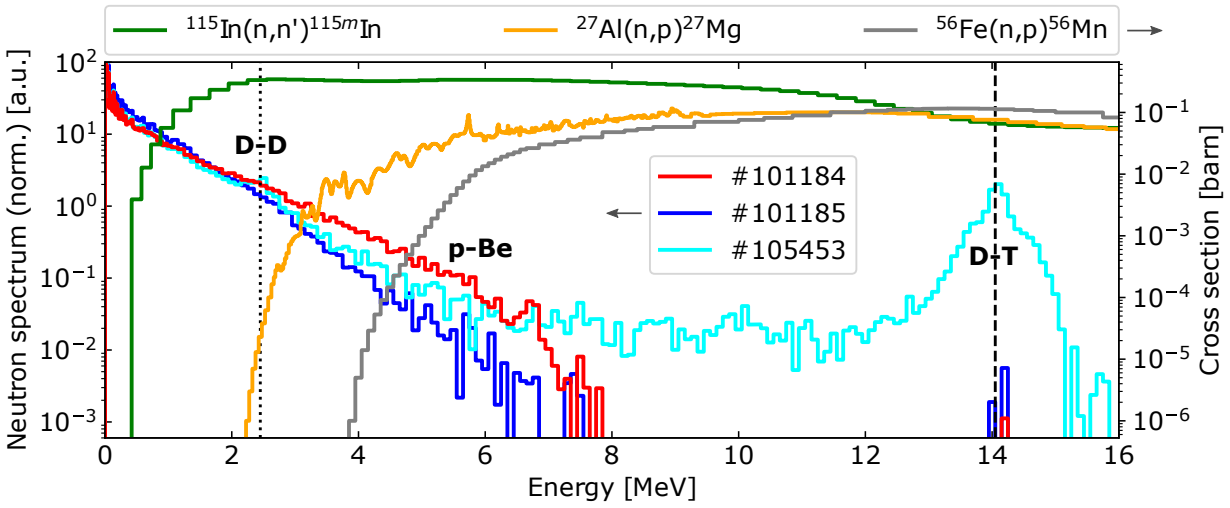

Figure 27: MCNP-calculated normalized (integral value) total neutron energy spectra at the position of JET's neutron activation system for realistic proton-beryllium sources in pulses #101184, #101185, and #105453. Denoted are the contributions from the dominant primary proton-beryllium fusion, as well as parasitic D-D and D-T reactions (emission peaks denoted with dotted and dashed lines, respectively). Cross sections for activation reactions on ^{115}In, ^{27}Al, and ^{56}Fe are shown [91].

In table 6 the MCNP-computed integral detector responses are presented for the proton-beryllium and generic sources. We show the relative discrepancy in the ^{235}U FC calculated response, normalised to the generic D-D source, averaged for three fission chambers located in JET octants 2, 6, and 8 [12]. We observe that response discrepancies are non-negligible for He plasma sources and show a generally lower value compared to the D-D source. This occurs because the FC response function decreases in the energy interval between the D-D peak and $\approx$ 6 MeV by more than 20 %, where the p–Be spectrum tail is prominent. Albeit neutron emissivity profiles for p–Be sources are different from the generic DD source, the main feature being their core hollowness, this is not expected to contribute more than ± 2 % to the observed FC response decrease due to the detectors' low sensitivity to plasma geometry changes [12]. Interestingly, the calculated response for #105453 does not differ from the generic source. This occurs because the ^{235}U FC response function increases for neutron energies above 10 MeV, corroborated by the relative increase in FC response for a generic D-T source, meaning that the FC's response to the prominent D-T spectral component in #105453 counteracts the integral response drop due to the p–Be tail. Large variations in

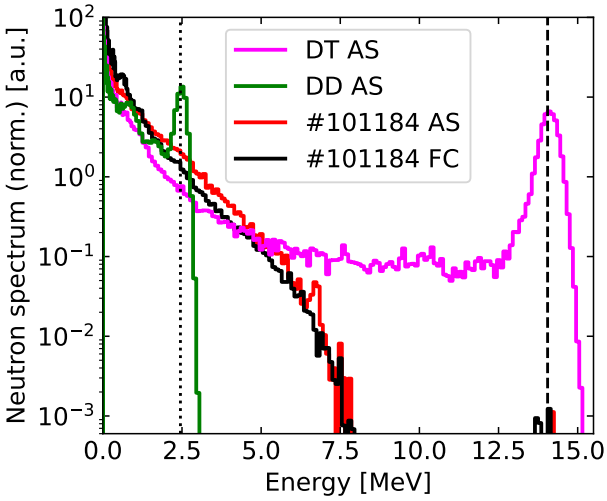

Figure 28: MCNP-calculated normalized (integral value) total neutron energy spectra at the position of JET's neutron activation system for generic D-D and D-T sources (emission peaks denoted with dotted and dashed lines, respectively), compared to He discharge #101184 spectra for the activation system and ex-vessel fission chambers.

fission chambers' relative response between the p–Be shots indicate that the FC absolute calibration factors for P_{fus} measurements in dominant p–Be plasmas are dependent on the source spectrum details and would need to be refined on an individual discharge basis, if applied to detector cross-calibration. We note that the calculated response difference is still comparable to the experimental uncertainty of JET's D-D absolute calibration of ± 10 %, applied to neutron yield measurements in these discharges.

The integral activation system response was calculated as the ratio of ^{27}Al(n,p) and ^{56}Fe(n,p) reactions over inelastic scattering on ^{115}In to eliminate the dependency on absolute neutron yield – this means we are able to infer information about the neutron spectrum shape and bypass uncertainties due to absolute normalisation [13]. The activation material coefficient $(m_{\mathrm{x}}M_{\mathrm{In}})/(m_{\mathrm{In}}M_{\mathrm{x}})$ is set to unity. Results in table 6 show that the Al and Fe activation coefficients for individual He discharges are a factor of 10 different, capturing the decay of the proton-beryllium neutron spectrum tail due to the reactions' varying cross section threshold, as shown in figure 27. In addition, the coefficients for individual foils are a factor of approximately 3.5 different for pulses #101184 and #101185, meaning that the activation set is capable of resolving the variation of p–Be spectrum energy gradients in the two pulses, driven by differences in fast proton distribution functions. Furthermore, there is negligible contribution of the D-T components to foil activation in the two He discharges, an effect that can be dominant and render the (n,p) reaction on Al and Fe insensitive to changes in neutron spectra above 2 MeV, as for example observed in pure D discharges due to T-burnup driven D-T neutron emission [13]. This is observed for D discharge #105453 in which the prominent D-T spectral component induces relatively high activation coefficient values, with the Al and Fe coefficients ratio being approximately 0.76 – challenging to measure and model precisely. Similar values are computed for the generic pure D-T source. In comparison, the activation of the two threshold reactions is negligible for a generic D-D source without the presence of energetic deuterons that could drive spectral anisotropies [13, 12].

Miniature fission chambers are seen to be relatively sensitive to the changes in plasma neutron source spectra. Specifically, the ^{235}U mFC is sensitive to the relative abundance of low-energy thermalised neutrons in the spectrum. Due to that the p–Be discharges trigger a relatively higher response compared to D-D and D-T. In addition, the response is proportional to the absolute value of the spectra energy gradients, resulting

in a 60 % higher response for pulse #101185 than #101184. In contrast, ^{238}U mFCs are sensitive to fast neutrons due to a sharp increase in the fission cross section beyond $E_n \approx 1$ MeV, meaning that the p–Be discharges trigger a generally lower response compared to both D-D and D-T generic sources, which have prominent peaks in the energy region of high fission probability. We note that the insensitivity to lower-energy neutrons renders the ^{238}U mFC less sensitive to changes or uncertainties in the surrounding geometry, compared to ^{238}U.

Table 6: Comparison of MCNP neutron transport calculations of JET's fission chambers (FC), neutron activation system (AS), and miniature fission chamber (mFC) response for proton-beryllium discharges #101184, #101185, and #1015453, as well as generic D-D and D-T neutron sources. FC and mFC responses are normalised to the generic D-D source. Reactions rates for Al and Fe activation are normalised to In foil activation. MCNP 1σ statistical uncertainties are specified.

Discharge → Tally ↓	#101184	#101185	#105453	D-D	D-T
$\left(\frac{\mathrm{FC}}{\mathrm{FC_{D-D}}} - 1\right)_{\langle \mathrm{Oct} \rangle}$ [%]	-5.2 ± 0.4	-10.2 ± 0.4	-0.4 ± 0.4	/	19.5 ± 0.4
AS $\propto \left(\frac{RR_{\mathrm{Al}}}{RR_{\mathrm{In}}}\right) \cdot 10^{-3}$ []	7.1 ± 0.2	2.1 ± 0.1	68 ± 2	0.08 ± 0.002	310 ± 10
AS $\propto \left(\frac{RR_{\mathrm{Fe}}}{RR_{\mathrm{In}}}\right) \cdot 10^{-3}$ []	0.75 ± 0.06	0.21 ± 0.06	90 ± 2	0.0	425 ± 7
$\left(\frac{m\mathrm{FC}}{m\mathrm{FC_{D-D}}} - 1\right)$ ^{235}U [%]	17 ± 3	27 ± 3	19 ± 3	/	9 ± 3
$\left(\frac{m\mathrm{FC}}{m\mathrm{FC_{D-D}}} - 1\right)$ ^{238}U [%]	-39 ± 2	-60 ± 2	-24 ± 2	/	61 ± 1

5. Discussion

Beryllium has been treated as a pivotal component of ITER's first wall solution for over a decade, with significant effort invested into upgrading JET to a metal beryllium/tungsten ITER-like-wall [93], and ITER scenario development with Be plasma facing components with integrated modelling tools [94, 42, 95]. JET's ILW enhancement has been extensively exploited to address key issues relevant for the operation of ITER and future fusion devices, such as wall retention properties, development of operational scenarios, and core confinement with a metal wall – most importantly with D-T plasmas [4]. However, a decision has been made to replace Be wall components with tungsten, and thus operate ITER with a full W wall [96]. The new ITER project baseline envisions boronization as a replacement for beryllium's important role of oxygen getter. In light of this decision, the integrated modelling framework we present can be applied to study the interaction between fast ions and newly introduced boron impurities in ITER. Of potential interest is the fusion between energetic protons and boron, ^{11}B(p,α)2α, which results in the production of three alphas with DT-like mean energy of ≈ 3.26 MeV [31, 97], recently been studied in magnetic confinement devices [98]. ^{11}B(p,α)2α could be explored in the currently planned *Start of Research Operations* phase, in which low density L- and H-mode H and D plasmas will be developed [96]. In these discharges B will be inherently present post-boronization, while protons could be accelerated through fundamental H RF minority heating, or synergetic H-NBI and second harmonic H RF heating. The latter would grant access to MeV-range protons in H-mode plasmas, probing the high-energy resonances of the proton-boron fusion cross section, enabling studies of alpha particle confinement and the effects of alpha-driven modes on global confinement well ahead of the *First Deuterium-Tritium* phase. Furthermore, the generated alphas themselves interact with boron via ^{10}B(α,nγ)^{13}N and ^{10}B(α,pγ)^{13}C fusion, emitting neutrons and gammas which can be used for alpha particle characterization and diagnostics commissioning.

To showcase the applicability of the presented framework to the study of arbitrary fusion between fast particles and plasma impurities we model reactions within the proton-boron fusion chain, i.e. alphas in

^{11}B(p,α)2α [31], neutrons in ^{10}B(α,nγ)^{13}N [99], and gammas in ^{10}B(α,pγ)^{13}C [20], using parameters of the best performing proton-beryllium JET discharge #101184. In the calculation the proton $f_{\mathrm{p,rf}}$ was preserved, while Be impurity profiles were replaced with B (isotopes ^{10}B at $\approx$ 20 % and ^{11}B at $\approx$ 80 % abundance) and adjusted to retain quasi-neutrality. The calculated ^{11}B(p,α)2α emissivity density profiles are shown in panel *(a)* of figure 29. The alpha birth spectra were obtained via fitting spectral measurements [97] with a double-Gaussian, shown in panel *(b)* of figure 29. Alpha source distributions were sampled and coupled to LOCUST to calculate the thermalised alpha density and distribution functions, with which the secondary ^{10}B(α,nγ)^{13}N and ^{10}B(α,pγ)^{13}C rates were estimated.

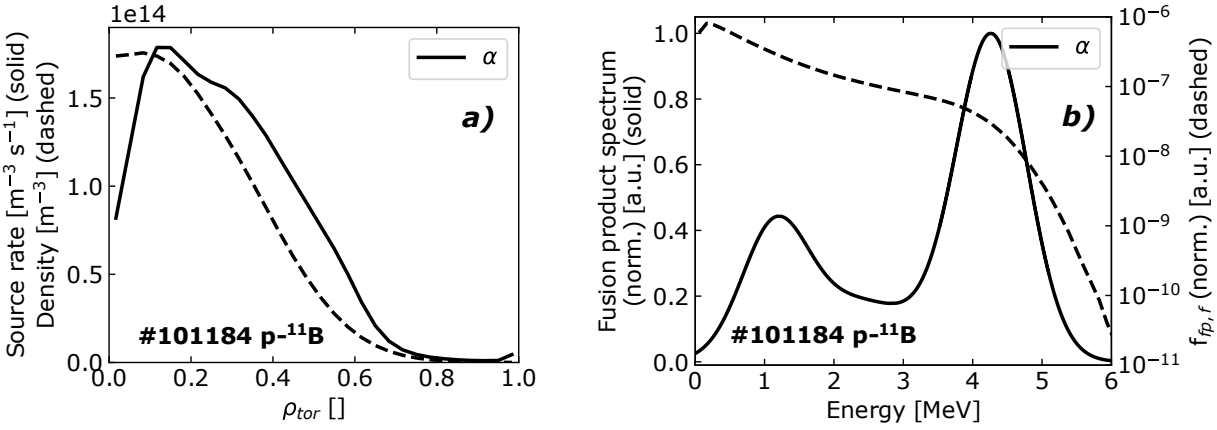

Figure 29: Modelled alpha fusion products for reaction ^{11}B(p,α)2α, using parameters from discharge #101184. Panel *(a)*: birth profiles (solid) and slowed-down density profiles (dashed). Panel *(b)*: Normalized (maximum) birth energy spectra (solid) and normalized (integral) fusion product energy distribution function (dashed). All quantities are plotted for an outboard core point at $\rho_{\mathrm{tor}} = 0.18$.

Results, summarized in table 7, show that the ^{11}B(p,α)2α alpha rate produced in JET discharge #101184, if beryllium were replaced with boron, would be higher than the total alpha rate of proton-beryllium fusion (table 1), however of the same order of magnitude. We observe that the computed alpha rates are comparable to those achieved in dedicated D-^{3}He experiments, if the same level of B and He-3 concentrations are assumed [32, 13]. This means that ^{11}B(p,α)2α could be a viable source of DT-like alphas in ITER's pre-DT operation, accessible via dedicated scenario development targeting low collisionality conditions and synergetic heating of protons. Similarly to Be secondary fusion, we assess that rates of neutron and gamma emission, triggered by the interaction between alpha fusion products and B impurities, would be several orders of magnitude lower than those of primary 3α fusion. Note that the ^{10}B(α,pγ)^{13}C fusion rate was estimated using the sum of cross sections for the first three excitation states at 3.089 MeV, 3.684 MeV, and 3.854 MeV. In JET experiments secondary Be fusion products emitted at low rates were on the limit of detectability, however the ^{9}Be(α,nγ)^{12}C gamma peak was detected and is visible in the spectrum measurement shown in figure 7. Based on the calculated rates in #101184-like conditions with boron present, we assess that gammas emitted via ^{10}B(α,pγ)^{13}C could have been observed at JET.

6. Conclusion

In the paper we present JET experiments targeting sustained conditions in which fusion performance is driven by the interaction between fast ions and plasma impurities due to a metal wall. For the first time a steady-state L-mode plasma with dominant proton-beryllium fusion and neutron yields of up to

Table 7: Computed volume-integrated particle rates for the proton-boron fusion chain using parameters from discharge #101184. Fusion product alphas are denoted α^*_{pb}.

Discharge → Reaction ↓	#101184
^{11}B(p,α)2α [α s^{-1}]	$3.6{\cdot}10^{15}$
^{10}B(α^*_{pb},nγ)^{13}N [neut. s^{-1}]	$7.4{\cdot}10^{7}$
^{10}B(α^*_{pb},pγ)^{13}C [γ s^{-1}]	$1.7{\cdot}10^{9}$

$\approx 6{\cdot}10^{13}$ s^{-1} is demonstrated, sustained over several fast ion slowing-down times, both in "aneutronic" He, and bulk D. The plasma scenarios, in which H was accelerated through fundamental frequency RF heating, were developed via maximizing the RF power density on the minority and decreasing collisionality, facilitating the evolution of a fast proton tail. The fusion drive is unambiguously confirmed by multiple independent plasma diagnostics. The presence of an MeV-range RF-accelerated proton minority is recorded by the neutral particle analyser and fast ion loss detector, and imprinted in the characteristics of observed MHD activity. Furthermore, the signature of proton-beryllium fusion products was detected by a gamma spectrometer, with a unique measurement of a broad ^{9}Be(p,$\alpha\gamma$)^{6}Li gamma peak at 3.56 MeV, and neutron fission chambers. The highest neutron yield in JET's *C43* He campaign was achieved by triggering proton-beryllium fusion, exceeding the campaign average by more than three orders of magnitude. This confirms the findings of modelling done for ITER's Pre-Fusion Power Operation phase, in which proton-beryllium fusion was computed to contribute non-negligibly to neutron emission in He plasmas and was identified as a crucial radiation safety issue [19]. We also show that sources of charged and neutral fusion products with significant strength can be generated and tailored through scenario development of pulses envisioned to be used in commissioning phases of future fusion devices, taking advantage of the inherently present metal wall impurities, and can be exploited for early nuclear diagnostics commissioning and studies of energetic particle confinement.

The bulk of the paper is dedicated to the demonstration of an integrated modelling framework, developed to model the two-stage proton beryllium-fusion chain, and produce high-fidelity fusion product source terms for use in synthetic diagnostics, fast particle, and neutron transport codes. The methodology couples JET plasma state data to TRANSP and JETTO for interpretive and predictive plasma core modelling, LOCUST for full orbit product tracking and collisional slowing-down, DRESS to resolve two- and three-body fusion kinematics, and ultimately MCNP for neutron transport calculations. We highlight the following modelling results, obtained by applying this tool to He and D proton-beryllium discharges:

- Plasma composition is accurately modelled by matching measurements of Z_{eff} (extraordinarily high for JET plasmas) and P_{rad} within the combined experimental and modelling uncertainty. This is achieved by inferring the impurity composition through a combination of diagnostics constraints and predictive full-radius impurity transport modelling.

- TRANSP-FPP computed H RF minority distribution function is coupled to LOCUST and corrected for prompt losses and finite Larmor radius effects. The computed pitch-energy distribution of proton losses is qualitatively matched against FILD measurements, capturing the prompt proton losses peak energy shift between the two He discharges due to changes in their proton distribution functions.

- Primary ^{9}Be(p,n)^{9}B reaction, with a threshold energy of 2.05 MeV, is found to be the dominant neutron emitter at naturally present concentrations of beryllium. The yield contribution of secondary

reactions between fusion products and beryllium, ^{9}Be(d,n)^{10}B and ^{9}Be(α,n)^{12}C, is found to be negligible, approximately four orders of magnitude lower than the primary reaction, agreeing with predictions for ITER [19].

- An estimate of the proton-deuteron knock-on effect on the total neutron yield in D discharge #105453 is performed, using a semi-empirical model based on NPA measurements of the fast D energy distribution function. It is found that the interactions between knock-on deuterons and residual D and T contribute around 25 % to the total calculated neutron rates.

- Calculated neutron rates match the fission chamber measurements within the combined experimental and computational uncertainty for He and D discharges. The average discrepancy from the experiment is $\approx \pm$ 20 %, which is well within the values observed for D-D and D-T discharges in which fusion performance is driven by fusion between fast and thermal ions [15, 88]. This is an important step towards an experimental validation of the modelling framework, and the newly evaluated beryllium fusion cross sections [29].

- Realistic proton-beryllium neutron sources are propagated through JET's MCNP neutron transport model, to calculate the response of fission chambers and the neutron activation system. We find that due to a variation in ^{235}U fission chambers' response function, which occurs between D-D and D-T neutron peaks where the proton-beryllium spectrum is most prominent, its response to p–Be neutrons is up to $\approx$ 10 % lower than to a generic D-D neutron source. Additionally, it is shown that differences in p–Be spectral tail energy gradients due to fast proton distribution variations in the discharges could be detected by employing the multi-foil neutron activation technique, using ^{115}In(n,n')^{115m}In, ^{27}Al(n,p)^{27}Mg, and ^{56}Fe(n,p)^{56}Mn reactions.

Most importantly, this is a demonstration of our capability to accurately model non-standard fusion reactions in tailored plasma discharges, growing our ability to predict and exploit these reactions in future fusion devices. We stress that, unfortunately, neutron yields were not high enough for meaningful count statistics on time-of-flight neutron spectrometer and neutron camera measurements, meaning that the modelled neutron spectra and emissivity profiles could not be independently validated against experimental data, as previously demonstrated for bulk D, T, and D-T plasmas [13, 33, 100, 101]. Through further scenario optimisation, such as increasing the plasma current, RF heating power, plasma density, pulse duration, and beryllium concentration, the neutron yield could have been improved further to enable TOFOR and neutron camera measurements, completing the validation effort. In addition, two independent experimental methods for probing the relationship between the fast proton distribution function and p–Be neutron spectra are proposed and computationally demonstrated in the paper: *(i)* the use of In, Al, and Fe activation foils and assessing the neutron spectra energy gradients by measuring and calculating their activation ratios, *(ii)* deploying miniature fission chambers to explore the effects of changes in p–Be emissivity profiles and spectra on their response, and test the detectors' suitability for fusion power measurements.

Due to ITER's decision to replace Be wall components with W and omit He discharge from the operational plan, we additionally demonstrate the application of this methodology to the study of newly relevant interactions between fast ions and boron impurities in ITER. It is shown that a p–B alpha source achieves reactions rates that are approximately two times larger than those of p–Be in same plasma conditions. Furthermore, the three-α source rate, normalized to B concentration, is comparable to that produced by D-^{3}He fusion, normalized to ^{3}He concentration, extensively studied in JET's three-ion RF experiments [21, 32, 13]. Because of this ^{11}B(p,α)2α could be exploited in future fusion devices to produce a steady-state source of alphas with DT-like energies for early studies of α confinement, well ahead of neutron-producing D and D-T

experiments. Due to a relatively low neutron and gamma emission rate produced in secondary reactions of the proton-boron chain the radiation safety challenge of exploiting this reactions is significantly smaller than that of Be fusion, meaning it is compatible with applications in aneutronic commissioning discharges aimed at nuclear diagnostics calibrations and fusion product studies. The p–B modelling methodology could be validated via relevant experiments on devices with a W wall and boron impurities [102], and experiments aiming at exploring the p–^{11}B path to commercial fusion [103, 98].

Acknowledgements

This work has been carried out within the framework of the EUROfusion Consortium, funded by the European Union via the Euratom Research and Training Programme (Grant Agreement No 101052200 — EUROfusion) and from the EPSRC [grant number EP/W006839/1]. Views and opinions expressed are however those of the author(s) only and do not necessarily reflect those of the European Union or the European Commission. Neither the European Union nor the European Commission can be held responsible for them.

References

[1] O. N. Jarvis, "Neutron measurement techniques for tokamak plasmas," *Plasma Physics and Controlled Fusion*, vol. 36, pp. 209–244, 2 1994. [Online]. Available: http://stacks.iop.org/0741-3335/36/i=2/a=002?key=crossref.2e5dddfbfca1e88fa9fb83fca4f1943d

[2] B. Wolle, "Tokamak plasma diagnostics based on measured neutron signals," *Physics Reports*, vol. 312, pp. 1–86, 5 1999. [Online]. Available: http://linkinghub.elsevier.com/retrieve/pii/S0370157398000842

[3] V. Kiptily, R. Dumont, M. Fitzgerald *et al.*, "Evidence of electron heating by alpha particles in JET deuterium-tritium plasmas," *Physical Review Letters*, vol. 131, p. 075101, 8 2023.

[4] C. Maggi, D. Abate, N. Abid *et al.*, "Overview of T and D-T results in JET with ITER-like wall," *Nuclear Fusion*, vol. 64, p. 112012, 11 2024.

[5] P. Batistoni, S. Popovichev, A. Cufar *et al.*, "14 mev calibration of JET neutron detectors - phase 1: calibration and characterization of the neutron source," *Nuclear Fusion*, vol. 58, p. 026012, 2 2018. [Online]. Available: http://stacks.iop.org/0029-5515/58/i=2/a=026012?key=crossref.62be43414208ce42d84e880519f8b59f

[6] P. Batistoni, S. Popovichev, Z. Ghani *et al.*, "14 mev calibration of JET neutron detectors - phase 2: in-vessel calibration," *Nuclear Fusion*, vol. 58, p. 106016, 10 2018. [Online]. Available: http://stacks.iop.org/0029-5515/58/i=10/a=106016?key=crossref.0f1845ba46b22a61ac624e0f7f63f80b

[7] A. Čufar, P. Batistoni, S. Conroy *et al.*, "Calculations to support in situ neutron yield calibrations at the joint european torus," *Fusion Science and Technology*, pp. 1–17, 8 2018. [Online]. Available: https://www.tandfonline.com/doi/full/10.1080/15361055.2018.1475163

[8] P. Raj, J. L. Ball, J. Carmichael *et al.*, "Overview of the neutron diagnostic systems for the SPARC tokamak," *Review of Scientific Instruments*, vol. 95, 10 2024.

[9] T. Nishitani, M. Ishikawa, M.-S. Cheon *et al.*, "Neutronic simulations of in-vessel neutron calibrations for ITER neutron diagnostics by using simplified ITER model," *Fusion Engineering and Design*, vol. 191, p. 113548, 6 2023.

[10] M. Cecconello, S. Conroy, G. Ericsson *et al.*, "Pre-conceptual study of the European DEMO neutron diagnostics," *Journal of Instrumentation*, vol. 14, pp. C09 001–C09 001, 9 2019.

[11] Ž. Štancar, M. Gorelenkova, S. Conroy *et al.*, "Generation of a plasma neutron source for Monte Carlo neutron transport calculations in the tokamak JET," *Fusion Engineering and Design*, vol. 136, pp. 1047–1051, 11 2018. [Online]. Available: https://linkinghub.elsevier.com/retrieve/pii/S0920379618303533

[12] Z. Štancar, M. Gorelenkova, S. Conroy *et al.*, "Multiphysics approach to plasma neutron source modelling at the JET tokamak," *Nuclear Fusion*, vol. 59, p. 096020, 9 2019.

[13] Ž. Štancar, Z. Ghani, J. Eriksson *et al.*, "Experimental validation of an integrated modelling approach to neutron emission studies at JET," *Nuclear Fusion*, vol. 61, p. 126030, 12 2021.

[14] A. Žohar, M. Nocente, B. Kos *et al.*, "Validation of realistic Monte Carlo plasma gamma-ray source on JET discharges," *Nuclear Fusion*, vol. 62, p. 066004, 6 2022.

[15] Ž. Štancar, K. Kirov, F. Auriemma *et al.*, "Overview of interpretive modelling of fusion performance in JET DTE2 discharges with TRANSP," *Nuclear Fusion*, vol. 63, p. 126058, 12 2023.

[16] H.-T. Kim, F. Auriemma, J. Ferreira *et al.*, "Validation of D-T fusion power prediction capability against 2021 JET D-T experiments," *Nuclear Fusion*, vol. 63, p. 112004, 11 2023.

[17] M. G. Johnson, C. Hellesen, E. A. Sundén *et al.*, "Neutron emission from beryllium reactions in JET deuterium plasmas with 3 he minority," *Nuclear Fusion*, vol. 50, p. 045005, 4 2010. [Online]. Available: http://stacks.iop.org/0029-5515/50/i=4/a=045005?key=crossref.03cc94ce87ebf8b0799a3326d2206971

[18] A. Krasilnikov, V. Kiptily, E. Lerche *et al.*, "Evidence of ^{9}Be + p nuclear reactions during $2\omega_{CH}$ and hydrogen minority ICRH in JET-ILW hydrogen and deuterium plasmas," *Nuclear Fusion*, vol. 58, p. 026033, 2 2018. [Online]. Available: https://iopscience.iop.org/article/10.1088/1741-4326/aa90c3

[19] A. R. Polevoi, A. Loarte, R. Bilato *et al.*, "Impact of suprathermal ions on neutron yield at pre-DT phase of iter operation," *Nuclear Fusion*, 4 2021. [Online]. Available: https://iopscience.iop.org/article/10.1088/1741-4326/abfa33

[20] V. Kiptily, "Gamma-ray measurements of ^{10}B(α,pγ)^{13}C reaction for alpha-particle diagnostics in fusion plasmas," *Fusion Engineering and Design*, vol. 215, p. 114959, 6 2025.

[21] Y. O. Kazakov, J. Ongena, J. C. Wright *et al.*, "Physics and applications of three-ion ICRF scenarios for fusion research," *Physics of Plasmas*, vol. 28, p. 020501, 2 2021. [Online]. Available: https://aip.scitation.org/doi/10.1063/5.0021818

[22] A. Pankin, J. Breslau, M. Gorelenkova *et al.*, "TRANSP integrated modeling code for interpretive and predictive analysis of tokamak plasmas," *Computer Physics Communications*, vol. 312, p. 109611, 7 2025.

[23] M. Romanelli, G. Corrigan, V. Parail *et al.*, "JINTRAC: A system of codes for integrated simulation of tokamak scenarios," *Plasma and Fusion Research*, vol. 9, pp. 3 403 023–3 403 023, 2014. [Online]. Available: https://www.jstage.jst.go.jp/article/pfr/9/0/9_3403023/_article

[24] R. J. Akers, E. Verwichte, T. J. Martin *et al.*, "GPGPU Monte Carlo calculation of gyro-phase resolved fast ion and n-state resolved neutral deuterium distributions," in *Proceedings of the 39th EPS Conference and 16th Int. Congress on Plasma Physics*, 2-6 July 2012, p. P5.088.
[25] J. Eriksson, S. Conroy, E. A. Sundén *et al.*, "Calculating fusion neutron energy spectra from arbitrary reactant distributions," *Computer Physics Communications*, vol. 199, pp. 40–46, 2 2016.
[26] M. E. Rising, J. C. Armstrong, S. R. Bolding *et al.*, "MCNP® Code Version 6.3.0 Release Notes," Los Alamos National Laboratory, Los Alamos, NM, USA, Tech. Rep. LA-UR-22-33103, Rev. 1, January 2023. [Online]. Available: https://www.osti.gov/biblio/1909545
[27] G. Rapisarda, L. Lamia, A. Caciolli *et al.*, "Experimental nuclear astrophysics with the light elements Li, Be and B: A review," *Frontiers in Astronomy and Space Sciences*, vol. 7, 2 2021.
[28] N. Hu, R. Kakino, A. Sasaki *et al.*, "Clinical evaluation of performance, stability, and longevity of an accelerator system designed for boron neutron capture therapy utilising a beryllium target," *Nuclear Instruments and Methods in Physics Research Section A: Accelerators, Spectrometers, Detectors and Associated Equipment*, vol. 1072, p. 170126, 3 2025.
[29] A. Žohar, A. Trkov, A. Hjalmarsson *et al.*, "Evaluation of cross sections for fast ion reactions with beryllium in helium and hydrogen fusion plasmas," *Nuclear Fusion*, vol. 64, p. 076040, 7 2024.
[30] G. Schnabel, D. Aldama, T. Bohm *et al.*, "FENDL: A library for fusion research and applications," *Nuclear Data Sheets*, vol. 193, pp. 1–78, 2 2024.
[31] A. Tentori and F. Belloni, "Revisiting p-^{11}B fusion cross section and reactivity, and their analytic approximations," *Nuclear Fusion*, vol. 63, p. 086001, 8 2023.
[32] M. Nocente, Y. Kazakov, J. Garcia *et al.*, "Generation and observation of fast deuterium ions and fusion-born alpha particles in JET d-^{3}he plasmas with the 3-ion radio-frequency heating scenario," *Nuclear Fusion*, vol. 60, p. 124006, 12 2020. [Online]. Available: https://iopscience.iop.org/article/10.1088/1741-4326/abb95d
[33] K. Kirov, E. Belonohy, C. Challis *et al.*, "Analysis of the fusion performance, beam–target neutrons and synergistic effects of JET's high-performance pulses," *Nuclear Fusion*, vol. 61, p. 046017, 4 2021. [Online]. Available: https://iopscience.iop.org/article/10.1088/1741-4326/abdfde
[34] V. Kiptily, M. Fitzgerald, Y. Kazakov *et al.*, "Evidence for Alfvén eigenmodes driven by alpha particles in D-^{3}he fusion experiments on JET," *Nuclear Fusion*, vol. 61, p. 114006, 11 2021.
[35] M. Dreval, S. Sharapov, Y. Kazakov *et al.*, "Alfvén cascade eigenmodes above the TAE-frequency and localization of Alfvén modes in D-^{3}he plasmas on JET," *Nuclear Fusion*, vol. 62, p. 056001, 5 2022.
[36] H. Oliver, S. Sharapov, Ž. Štancar *et al.*, "Toroidal Alfvén eigenmodes observed in low power JET deuterium–tritium plasmas," *Nuclear Fusion*, vol. 63, p. 112008, 11 2023.
[37] S. Mazzi, J. Garcia, D. Zarzoso *et al.*, "Enhanced performance in fusion plasmas through turbulence suppression by mega-electronvolt ions," *Nature Physics*, vol. 18, pp. 776–782, 7 2022.
[38] J. Garcia, Y. Kazakov, R. Coelho *et al.*, "Stable Deuterium-Tritium plasmas with improved confinement in the presence of energetic-ion instabilities," *Nature Communications*, vol. 15, p. 7846, 9 2024.
[39] J. Eriksson, C. Hellesen, F. Binda *et al.*, "Measuring fast ions in fusion plasmas with neutron diagnostics at JET," *Plasma Physics and Controlled Fusion*, vol. 61, p. 014027, 1 2019. [Online]. Available: http://stacks.iop.org/0741-3335/61/i=1/a=014027?key=crossref.a7dfe8661a997a23bdf2ad67579ca921
[40] M. Nocente, V. Kiptily, M. Tardocchi *et al.*, "Fusion product measurements by nuclear diagnostics in the Joint European Torus deuterium–tritium 2 campaign," *Review of Scientific Instruments*, vol. 93, 9 2022.
[41] H. Järleblad, B. Reman, Y. Dong *et al.*, "Reconstruction of the fast-ion deuterium distribution in a tritium-rich plasma in the JET DTE2 campaign," *Nuclear Fusion*, vol. 65, p. 016060, 1 2025.
[42] E. Tholerus, L. Garzotti, V. Parail *et al.*, "Access and sustainment of ELMy H-mode operation for ITER pre-fusion power operation plasmas using JINTRAC," *Nuclear Fusion*, vol. 65, p. 036006, 3 2025.
[43] D. Matveev, D. Douai, T. Wauters *et al.*, "Tritium removal from JET-ILW after T and D-T experimental campaigns," *Nuclear Fusion*, vol. 63, p. 112014, 11 2023.
[44] V. I. Afanasyev, A. Gondhalekar, P. Y. Babenko *et al.*, "Neutral particle analyzer/isotope separator for measurement of hydrogen isotope composition of JET plasmas," *Review of Scientific Instruments*, vol. 74, pp. 2338–2352, 4 2003.
[45] S. Baeumel, A. Werner, R. Semler *et al.*, "Scintillator probe for lost alpha measurements in JET," *Review of Scientific Instruments*, vol. 75, pp. 3563–3565, 10 2004.
[46] P. Bonofiglo, V. Kiptily, J. Rivero-Rodriguez *et al.*, "Alpha particle loss measurements and analysis in JET DT plasmas," *Nuclear Fusion*, vol. 64, p. 096038, 9 2024.
[47] C. Cheng, L. Chen, and M. Chance, "High-n ideal and resistive shear Alfvén waves in tokamaks," *Annals of Physics*, vol. 161, pp. 21–47, 4 1985.
[48] S. Hacquin, S. E. Sharapov, B. Alper *et al.*, "Localized x-mode reflectometry measurements of alfvén eigenmodes on the jet tokamak," *Plasma Physics and Controlled Fusion*, vol. 49, pp. 1371–1390, 9 2007.

[49] R. Betti and J. P. Freidberg, "Stability of Alfvén gap modes in burning plasmas," *Physics of Fluids B: Plasma Physics*, vol. 4, pp. 1465–1474, 6 1992.
[50] H. J. C. Oliver, S. E. Sharapov, B. N. Breizman *et al.*, "Axisymmetric global Alfvén eigenmodes within the ellipticity-induced frequency gap in the Joint European Torus," *Physics of Plasmas*, vol. 24, 12 2017.
[51] M. Fitzgerald, J. Buchanan, S. Sharapov *et al.*, "Full-orbit and drift calculations of fusion product losses due to explosive fishbones on JET," *Nuclear Fusion*, vol. 59, p. 016004, 1 2019.
[52] V. Kiptily, M. Fitzgerald, V. Goloborodko *et al.*, "Fusion product losses due to fishbone instabilities in deuterium JET plasmas," *Nuclear Fusion*, vol. 58, p. 014003, 1 2018.
[53] Y. Kazakov, M. Nocente, M. Mantsinen *et al.*, "Plasma heating and generation of energetic D ions with the 3-ion ICRF + NBI scenario in mixed H-D plasmas at JET-ILW," *Nuclear Fusion*, vol. 60, p. 112013, 11 2020. [Online]. Available: https://iopscience.iop.org/article/10.1088/1741-4326/ab9256
[54] L. Generalov, S. Abramovich, A. Zvenigorodskij *et al.*, "Measurement of differential cross sections of gamma quanta production with Eg=3.563 MeV from the reaction 9Be(p,alpha)6Li* (3.563 MeV) at 0 degree," *Bulletin of the Russian Academy of Sciences: Physics*, vol. 67, p. 1616, 2003.
[55] L. Generalov and S. Abramovich, "Total cross section of the Be-9(p,a)Li-6* (3.5618 MeV) reaction at Ep<2.4 MeV," *Bulletin of the Russian Academy of Sciences: Physics*, vol. 69, p. 1819, 2005.
[56] D. Zahnow, C. Angulo, M. Junker *et al.*, "Thermonuclear reaction rates of 9Be(p, γ)10B," *Nuclear Physics A*, vol. 589, pp. 95–105, 6 1995.
[57] G. M. Griffiths, E. A. Larson, and L. P. Robertson, "The capture of protons by deuterons," *Canadian Journal of Physics*, vol. 40, pp. 402–411, 4 1962.
[58] D. Kocher and T. Clegg, "Cross sections for proton-deutron scattering from 1.0 to 10.0 MeV," *Nuclear Physics A*, vol. 132, pp. 455–467, 7 1969.
[59] M. Swinhoe and O. Jarvis, "Calculation and measurement of 235U and 238U fission counter assembly detection efficiency," *Nuclear Instruments and Methods in Physics Research*, vol. 221, pp. 460–465, 4 1984. [Online]. Available: http://linkinghub.elsevier.com/retrieve/pii/0167508784900206
[60] M. G. Johnson, L. Giacomelli, A. Hjalmarsson *et al.*, "The 2.5-MeV neutron time-of-flight spectrometer TOFOR for experiments at JET," *Nuclear Instruments and Methods in Physics Research Section A: Accelerators, Spectrometers, Detectors and Associated Equipment*, vol. 591, pp. 417–430, 6 2008. [Online]. Available: http://linkinghub.elsevier.com/retrieve/pii/S0168900208003574
[61] L. Giacomelli, S. Conroy, G. Gorini *et al.*, "Tomographic analysis of neutron and gamma pulse shape distributions from liquid scintillation detectors at joint european torus," *Review of Scientific Instruments*, vol. 85, p. 023505, 2 2014. [Online]. Available: http://aip.scitation.org/doi/10.1063/1.4864122
[62] J. Breslau, M. Gorelenkova, F. Poli *et al.*, "Transp," 2018.
[63] M. Brambilla, "Numerical simulation of ion cyclotron waves in tokamak plasmas," *Plasma Physics and Controlled Fusion*, vol. 41, pp. 1–34, 1 1999. [Online]. Available: http://stacks.iop.org/0741-3335/41/i=1/a=002?key=crossref.6be5bf4454aa8509b29f6c6f604db3f5
[64] G. Hammett, "Fast ion studies of ion cyclotron heating in the PLT tokamak," *University Microfilms International No. GAX86-12694*, 1986.
[65] L. Lauro-Taroni, B. Alper, R. Giannella *et al.*, "Impurity transport of high performance discharges in JET," in *Proceedings of the 21st EPS Conference on Controlled Fusion and Plasma Physics, 18B*, 27 June - 1 July 1994, p. 102. [Online]. Available: http://libero.ipp.mpg.de/libero/PDF/EPS_21_Vol1_1994.pdf
[66] L. Frassinetti, M. N. A. Beurskens, R. Scannell *et al.*, "Spatial resolution of the JET thomson scattering system," *Review of Scientific Instruments*, vol. 83, p. 013506, 1 2012. [Online]. Available: http://aip.scitation.org/doi/10.1063/1.3673467
[67] S. Schmuck, J. Fessey, T. Gerbaud *et al.*, "Electron cyclotron emission measurements on JET: Michelson interferometer, new absolute calibration, and determination of electron temperature," *Review of Scientific Instruments*, vol. 83, p. 125101, 12 2012. [Online]. Available: http://aip.scitation.org/doi/10.1063/1.4768246
[68] N. C. Hawkes, E. Delabie, S. Menmuir *et al.*, "Instrumentation for the upgrade to the JET core charge-exchange spectrometers," *Review of Scientific Instruments*, vol. 89, p. 10D113, 10 2018.
[69] A. Thorman, E. Litherland-Smith, S. Menmuir *et al.*, "Visible spectroscopy of highly charged tungsten ions with the JET charge exchange diagnostic," *Physica Scripta*, vol. 96, p. 125631, 12 2021.
[70] E. Delabie, N. Hawkes, T. M. Biewer *et al.*, "In situ wavelength calibration of the edge CXS spectrometers on JET," *Review of Scientific Instruments*, vol. 87, p. 11E525, 11 2016.
[71] A. M. Patel, N. C. Hawkes, K.-D. Zastrow *et al.*, "X-ray crystal spectrometer throughput, data treatment, and configuration over the JET DTE2 and DTE3 campaigns," *Review of Scientific Instruments*, vol. 96, 9 2025.
[72] G. Szepesi, L. Appel, E. D. la Luna *et al.*, "Advanced equilibrium reconstruction for JET with EFIT++," in *Proceedings of the 47th EPS Plasma Physics conference*, 21-25 June 2021.

[73] A. A. Teplukhina, M. Podesta, F. M. Poli *et al.*, "Fast ion transport by sawtooth instability in the presence of icrf-nbi synergy in JET plasmas," *Nuclear Fusion*, 9 2021. [Online]. Available: https://iopscience.iop.org/article/10.1088/1741-4326/ac2524
[74] W. A. Houlberg, K. C. Shaing, S. P. Hirshman *et al.*, "Bootstrap current and neoclassical transport in tokamaks of arbitrary collisionality and aspect ratio," *Physics of Plasmas*, vol. 4, pp. 3230–3242, 9 1997.
[75] M. Erba, T. Aniel, V. Basiuk *et al.*, "Validation of a new mixed Bohm/gyro-Bohm model for electron and ion heat transport against the ITER, Tore Supra and START database discharges," *Nuclear Fusion*, vol. 38, pp. 1013–1028, 7 1998.
[76] G. Staebler, E. A. Belli, J. Candy *et al.*, "Verification of a quasi-linear model for gyrokinetic turbulent transport," *Nuclear Fusion*, vol. 61, p. 116007, 11 2021.
[77] H. P. Summers, "Atomic Data and Analysis Structure User Manual 2.7," 2004. [Online]. Available: https://www.adas.ac.uk/manual.php
[78] A. Czarnecka, K.-D. Zastrow, J. Rzadkiewicz *et al.*, "Determination of metal impurity density, ΔZ_{eff} and dilution on JET by VUV emission spectroscopy," *Plasma Physics and Controlled Fusion*, vol. 53, p. 035009, 3 2011.
[79] S. S. Henderson, M. Bluteau, A. Foster *et al.*, "Optimisation and assessment of theoretical impurity line power coefficients relevant to ITER and DEMO," *Plasma Physics and Controlled Fusion*, vol. 59, p. 055010, 5 2017.
[80] T. Pütterich, R. Neu, R. Dux *et al.*, "Modelling of measured tungsten spectra from ASDEX Upgrade and predictions for ITER," *Plasma Physics and Controlled Fusion*, vol. 50, p. 085016, 8 2008.
[81] H. P. Summers, W. J. Dickson, M. G. O'Mullane *et al.*, "Ionization state, excited populations and emission of impurities in dynamic finite density plasmas: I. the generalized collisional–radiative model for light elements," *Plasma Physics and Controlled Fusion*, vol. 48, pp. 263–293, 2 2006.
[82] S. Vartanian, E. Delabie, C. Klepper *et al.*, "Simultaneous h/d/t and 3he/4he absolute concentration measurements with an optical penning gauge on JET," *Fusion Engineering and Design*, vol. 170, p. 112511, 9 2021.
[83] M. Maslov, E. Lerche, F. Auriemma *et al.*, "JET D-T scenario with optimized non-thermal fusion," *Nuclear Fusion*, vol. 63, p. 112002, 11 2023.
[84] D. V. Eester and E. Lerche, "Simple 1D Fokker-Planck modelling of ion cyclotron resonance frequency heating at arbitrary cyclotron harmonics accounting for Coulomb relaxation on non-Maxwellian populations," *Plasma Physics and Controlled Fusion*, vol. 53, p. 092001, 9 2011.
[85] L. Ballabio, G. Gorini, and J. Källne, "α-particle knock-on signature in the neutron emission of DT plasmas," *Physical Review E*, vol. 55, pp. 3358–3368, 3 1997.
[86] J. Varje, P. Sirén, H. Weisen *et al.*, "Synthetic NPA diagnostic for energetic particles in JET plasmas," *Journal of Instrumentation*, vol. 12, pp. C11 025–C11 025, 11 2017.
[87] D. Brown, M. Chadwick, R. Capote *et al.*, "ENDF/B-VIII.0: The 8^{th} major release of the nuclear reaction data library with CIELO-project cross sections, new standards and thermal scattering data," *Nuclear Data Sheets*, vol. 148, pp. 1–142, 2 2018.
[88] H. Weisen, H.-T. Kim, J. Strachan *et al.*, "The 'neutron deficit' in the JET tokamak," *Nuclear Fusion*, vol. 57, p. 076029, 7 2017.
[89] I. Lengar, T. Vasilopoulou, M. Kłosowski *et al.*, "Characterisation of the neutron field for streaming analyses in TT operations at JET," *Fusion Engineering and Design*, vol. 202, p. 114351, 5 2024.
[90] A. Čufar, B. Kos, I. A. Kodeli *et al.*, "The analysis of the external neutron monitor responses in a simplified JET-like tokamak using advantg," *Fusion Science and Technology*, vol. 71, 2 2017.
[91] A. Trkov, P. Griffin, S. Simakov *et al.*, "IRDFF-II: A New Neutron Metrology Library," *Nuclear Data Sheets*, vol. 163, pp. 1–108, 1 2020. [Online]. Available: https://linkinghub.elsevier.com/retrieve/pii/S0090375219300687
[92] Ž. Štancar, L. Barbot, C. Destouches *et al.*, "Computational validation of the fission rate distribution experimental benchmark at the JSI TRIGA Mark II research reactor using the Monte Carlo method," *Annals of Nuclear Energy*, vol. 112, pp. 94–108, 2 2018.
[93] F. Romanelli, "Overview of the JET results with the ITER-like wall," *Nuclear Fusion*, vol. 53, p. 104002, 10 2013. [Online]. Available: http://stacks.iop.org/0029-5515/53/i=10/a=104002?key=crossref.911ea29ee69f0c4d016990aaf7fc592a
[94] M. Schneider, E. Lerche, D. V. Eester *et al.*, "Simulation of heating and current drive sources for scenarios of the ITER research plan," *Nuclear Fusion*, vol. 61, p. 126058, 12 2021.
[95] F. Eriksson, E. Tholerus, G. Corrigan *et al.*, "Simulations of the stationary Q=10 and the exit phase from the flat-top of an ITER 15MA baseline scenario: predictive JINTRAC simulation with a consistent treatment of D and T in the whole plasma," *Nuclear Fusion*, vol. 64, p. 126033, 12 2024.
[96] P. Barabaschi, A. Fossen, A. Loarte *et al.*, "ITER progresses into new baseline," *Fusion Engineering and Design*, vol. 215, p. 114990, 6 2025.
[97] M. H. Sikora and H. R. Weller, "A new evaluation of the ^{11}B(p, α)$\alpha\alpha$ Reaction Rates," *Journal of Fusion Energy*, vol. 35, pp. 538–543, 6 2016.
[98] R. M. Magee, K. Ogawa, T. Tajima *et al.*, "First measurements of p^{11}B fusion in a magnetically confined plasma," *Nature*

Communications, vol. 14, p. 955, 2 2023.

[99] Q. Liu, M. Febbraro, R. J. deBoer *et al.*, "Measurement of the $^{10}B(\alpha,n_0)^{13}N$ cross section for $2.2 < E_\alpha < 4.9$ MeV and its application as a diagnostic at the National Ignition Facility," *Physical Review C*, vol. 100, p. 034601, 9 2019.

[100] B. Eriksson, S. Conroy, G. Ericsson *et al.*, "Determining the fuel ion ratio for D(T) and T(D) plasmas at JET using neutron time-of-flight spectrometry," *Plasma Physics and Controlled Fusion*, vol. 64, p. 055008, 5 2022.

[101] L. Hägg, J. Eriksson, S. Conroy *et al.*, "Plasma rotation and thermonuclear neutron emission estimates in JET deuterium tritium plasmas from neutron spectroscopy," *Plasma Physics and Controlled Fusion*, vol. 67, p. 035024, 3 2025.

[102] D. Fajardo, C. Angioni, R. Dux *et al.*, "Full-radius integrated modelling of ASDEX Upgrade L-modes including impurity transport and radiation," *Nuclear Fusion*, vol. 64, p. 046021, 4 2024.

[103] Y. Shi, Y. Wang, B. Liu *et al.*, "Overview of EXL-50 research progress," *Nuclear Fusion*, vol. 65, p. 092004, 9 2025.